**Improving the homogeneity of superparamagnetic nanoparticles and a study of their physicochemical properties and applications**

by

Barry Jay Yeh

A dissertation submitted to the Graduate Faculty of
Auburn University
in partial fulfillment of the
requirements for the Degree of
Doctor of Philosophy

Auburn, Alabama
May 5, 2018

Keywords: Iron Oxide Nanoparticles, Size-Selective Fractionation, Magnetic Resonance Imaging



Approved by

Allan E. David, Chair, Assistant Professor of Chemical Engineering
Mario R. Eden, Professor of Chemical Engineering
Thomas Hanley, Professor of Chemical Engineering
Bart Prorok, Professor of Materials Engineering
Christopher J. Easley, Associate Professor of Chemistry and Biochemistry

## Abstract

Superparamagnetic iron oxide nanoparticles (SPIONs) have enormous potential in biomedical applications, including drug delivery, magnetic hyperthermia treatment (MHT), and contrast enhancement for magnetic resonance imaging (MRI). SPIONs larger than 20 nm are generally synthesized with a multi-core structure held together by an external matrix. This typically yields particles with a very broad size distribution, having a polydispersity index (PdI) of about 0.23. This broad size distribution hinders clinical translation of these particles because of safety and performance variability [1–3]. While several size fractionation techniques have been employed, including magnetic fractionation, centrifugation, gel chromatography, and vacuum filtration to improve nanoparticle size homogeneity, the particle size distribution remains much higher than gold, silica, and other nanoparticles [4–10]. Therefore, a novel separation method, diffusive magnetic fractionation (DMF), is introduced to narrow the broad size distribution of SPIONs. The DMF is proven to be scalable, controllable and efficient. Its fractionated SPIONs were used to enhance mass transport through biological barriers by a rotational magnetic field. The mass transport of SPIONs showed a strong size dependency. Furthermore, mathematic models were developed and showed a strong correlation between theoretical and experimental data. Therefore, the models are used to predict the result of the fractionation and to optimize the process efficiency.

Acknowledgement

I would like to express my sincere gratitude to my advisor Dr. Allan David for the continuous support of my Ph.D. study and related research, for his patience, motivation, and immense knowledge. His guidance helped me in all the time. I could not have imagined having a better advisor and mentor for my Ph.D. study.

Besides my advisor, I would like to thank the rest of my committee: Dr. Mario Eden, Dr. Thomas Hanley, Dr. Bart Prorok, and Dr. Christopher Easley, for their insightful comments and encouragement.

I thank all members in Dr. David's research group in for the support, for all the long meetings we had before deadlines. Last but not the least, I would like to thank my family: my parents and sister for supporting me spiritually throughout my life.

Table of Contents

List of Figures

List of Abbreviations

| | |
|---|---|
| DLS | Transmission Electron Microscopy |
| DMF | Diffusive Magnetic Fractionation |
| DMF-SPIONs | Diffusive Magnetic Fractionated Superparamagnetic Iron Oxide Nanoparticles |
| EPR | Enhanced Permeability and Retention |
| MF | Magnetic Fractionation |
| MF-SPIONs | Magnetic Fractionated Superparamagnetic Iron Oxide Nanoparticles |
| MHT | Magnetic Hyperthermia Treatment |
| MRI | Magnetic Resonance Imaging |
| MSPIONs | Multicore Superparamagnetic Iron Oxide Nanoparticles |
| PEG | Polyethylene Glycol |
| PI | Polydispersity Index |
| PMF | Pulsed Magnetic Field |
| SEC | Size Exclusion Gel Chromatography |
| SEM | Scanning Electron Microscopy |
| SPION | Superparamagnetic Iron Oxide Nanoparticles |
| SQUID | Superconducting Quantum Interference Devices |
| TEM | Transmission Electron Microscopy |
| USPIONs | Ultra-small Superparamagnetic Iron Oxide Nanoparticles |

## Chapter 1 : Introduction

Nanotechnology has become a major research topic since the 1990s because of the discovery of Enhanced Permeability and Retention (EPR) effects. SPIONs became the ultimate nanomaterial for biomedical applications because of their unique combination of biocompatibility and superparamagnetic property. Unfortunately, SPIONs have a very broad particle size distribution, which result in performance variability and safety concerns especially for biomedical applications [1–3]. Nanoparticle's biodistribution, cellular uptake, pharmacokinetics and MRI imaging contrast enhancement are all negatively affected by the broad size distribution [11,12]. This problem remains due to the limitation of current chemical synthesis and particle size selection methods. Thus, a novel separation method, diffusive magnetic fractionation (DMF), is introduced to homogenize the broad size distribution of SPIONs.

The DMF separates different sized SPIONs by their magnet and diffusive mobility. DMF separated SPIONs (DMF-SPIONs) have an average size distribution at least three times narrower than conventional methods. Nevertheless, the current DMF is laborious to establish because of the method is based on a trial and error approach. Therefore, a systematic and reproducible method to setup the DMF is necessary. We developed a mathematical approach. The approach built on the SPION's physical property of diffusion and attraction under the influences of a magnetic field. The model aided us to setup the DMF for SPIONs with different distribution and avoid the time-consuming trial and error approach.

The goal of this project is to make the DMF applicable for different scientific researches and to demonstrate the importance of SPION's size distribution. The first part of the project is to optimize the DMF for SPIONs with different formulations and avoid the current arduous process. The second parts of the project is to demonstrate the influence of SPION's size distribution. The

particle size and particle size distribution has a strong impact on the mass transport and bio-distribution of SPIONs, which affects the biomedical performance and safety [1–3]. We are using DMF-SPIONs to enhance the mass transportation of SPIONs and showing that the SPION's size distribution is a crucial problem for biomedical applications and the DMF is a solution for it.

1.1: Background

SPIONs are commonly used for biomedical applications because of their unique combination of strong superparamagnetic character and bio-compatibility. Superparamagnetic character happens when thermal fluctuations overcomes magnetic interactions between particles, which is usually only achievable for nanomaterials or thin film materials [13]. The character prevents magnetic nanoparticles to aggregate due to magnetic attractions between particles. Generally, SPION's particle sizes need to be smaller than 29-36 ± 5 nm to be superparamagnetic, which a critical size of 20 nm is generally used in most synthesis studies to ensure superparamagnetic characteristics [14–18]. These SPIONs are also known as ultra-small SPIONs (USPIONs). However, most biomedical applications take place within the size range of 10-150 nm because of the EPR. Therefore, multiple single-core SPIONs were packaged together to form a larger multi-core SPIONs (MSPIONs) for biomedical applications between 20-150 nm, including all three major SPION applications, drug delivery, MHT and MRI contrast enhancement.

Most synthesis process can produce both USPIONs and MSPIONs with different reaction conditions. USPIONs have better synthesis controls in physical properties, such as particle sizes, size distributions, compositions and particle shapes [19–23]. USPIONs also have a higher cell uptake, longer blood circulation and higher penetration of capillary wall than multi-core particles [7]. USPIONs nanoparticles usually have a particle size distribution of $\sigma \leq 5\%$ [24,25]. Unfortunately, USPION can only be used for biomedical applications within 10-20 nm particle size range. On the other hand, MSPIONs are poorly controlled in size, size distribution, and composition, but commonly used for the majority of biomedical applications [25–28]. These biomedical applications utilized particle size range between 20-150 nm because of large surface area, higher energy transformations, biodistribution and higher MRI contrast [27]. In fact, most of the current clinically approved SPIONs are MSPIONs [29–31]. The size distribution of MSPIONs is usually very broad

with $\sigma \geq 20\%$ [26–28]. The broad size distribution of MSPIONs hinders translation of MSPION performance to clinical use due to safety concerns and performance variabilities. The particle size distribution negatively affects biodistribution and pharmacokinetics of MSPIONs and creates performance variabilities on all major MSPION applications, including drug delivery, contrast enhanced MRI, and MHT [11,32]. For decades, the problem remains unsolved because of the limitations of chemical synthesis and failures of conventional size selection techniques in providing competitive monodispersed MSPIONs in comparison with other nanomaterials such as gold, silica, and other nanoparticles [33,34].

1.2: Particle size and size distribution effects on target delivery

In 1986, nanoparticles were observed to have EPR effect in tumor [35]. The US government has encouraged the development of nanoparticle based drug carriers since 2000 [36]. In the majority of applications, the biodistribution and the pharmacokinetics greatly determined the performance of nanoparticle carriers [37–39]. However, both the biodistribution and the pharmacokinetics were negatively influenced by particles sizes and size distributions. Different sized nanoparticles tended to accumulate in different areas of a biological system [11,32]. As a result, the particle size distribution will affect the amount of particle accumulation at a certain biological entity. Similarly, the pharmacokinetics of a nanoparticle have direct impact on the performance of the biomedical applications [38,40]. For most nanoparticle formulation, the size of the particles directly affects the pharmacokinetics [6,41,42]. In order to reach a targeted entity, nanoparticles have to overcome multiple biological barriers and avoid clearance from blood circulation, which makes the size of the particle important [6,43]. Recently, more studies focus on how the physical and chemical properties of nanoparticles affect their blood half-lives and biodistribution. However, the effect of particle size distributions in a biological system remains unclear.

Researchers have been using different purification techniques to refine particle size distributions and to improve biodistribution and performances of SPIONs. For example, SPION AMI25, Ferumoxide, has a broad distribution with an average size of about 150 nm, as shown in Figure 1.1. AMI25 was filtered to generate particles of 20 nm. Fractionated AMI25 was reported with a blood half-life of 15.9 h in rabbits in comparison to the original Ferumoxide of 0.46 h [5]. The difference in performances between different sized particles confirms the need for controlled size distribution for effective delivery in biomedical researches [6,7,44–46].

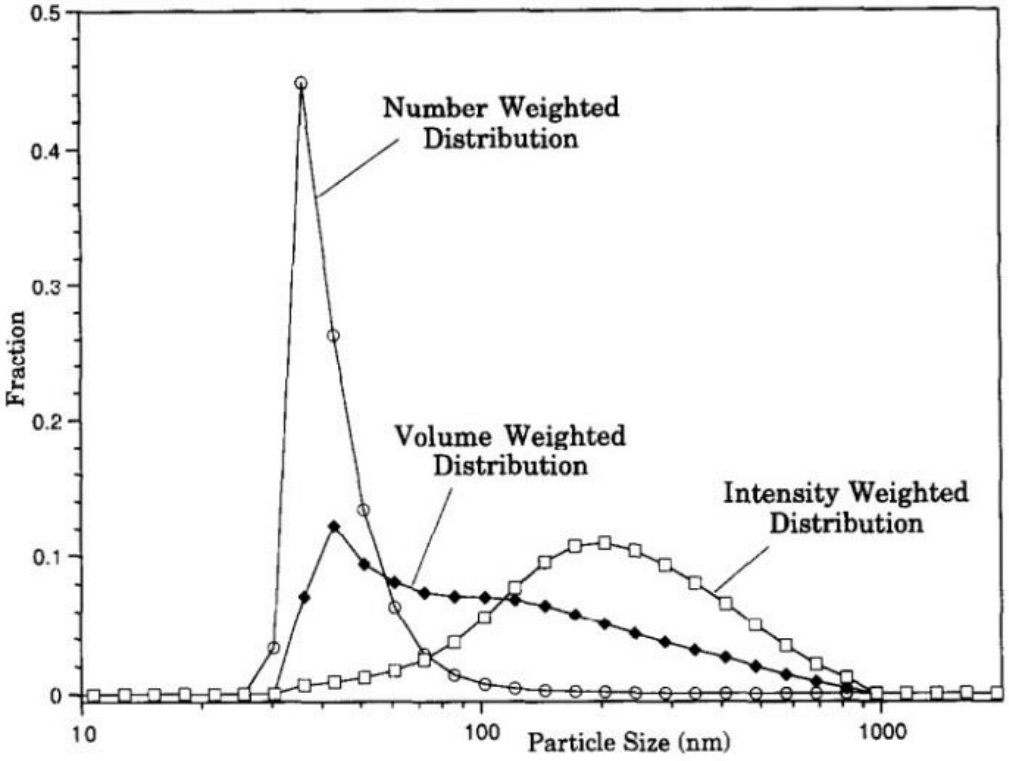


Figure 1.1. Ferumoxides lognormal particle size distribution by DLS (dynamic light scattering) [47]. The average sizes about 42 nm by number, 137 nm by volume and 250 nm by intensity. The particle size distributions are very broad, which were estimated to be $\sigma \sim 22\%$ by number, $\sigma \sim 89\%$ by volume and $\sigma \sim 62\%$ by intensity. ($\sigma$ = standard deviation/mean). This figure is reprinted with permission.

1.3: Particle size and size distribution effects on MRI application

MRI is obtained by applying perpendicular radiofrequency pulses to a constant magnetic field to induce magnetization and relaxation of protons within tissues. The T2 relaxation time is measured when protons emit the absorbed radiofrequency energy. The presence of SPIONs shortens the T2 ation time, which enhances the contrast of MRI. This phenomenon results from the magnetic field distortion near magnetic particles. The concept of MRI is based on the absorption and emission of radiofrequency energy from protons. The presence of SPIONs creates a magnetic field distortion interaction where the strong superparamagnetic character rapidly reacts to the oscillating radio frequency and accelerates the rate of energy release from the nearby protons. The field distortion significantly shortens the T2 relaxation time of protons and separates it from background noises, which makes SPIONs perfect candidates for MRI contrast agents.

Ferumoxides (Feridex®, Endorem®) and Ferucarbotran (Resovist ®, Cliavist®) are two types of SPIONs clinically approved as MRI contrast agents specifically for liver in the mid-1990s. Ferumoxides were developed by AMAG Pharma (former Advanced Magnetics) and were referred as AMI-25. The transverse ($r_2$) and longitudinal ($r_1$) relaxivities are 98.3 and 23.9 $mM^{-1}sec^{-1}$. Ferumoxides are 80-150 nm SPIONs with low molecular weight dextran coating. Ferucarbotran was developed by Schering AG, and was referred as SHU 555A [48]. Resovist is a carboxydextrane-coated SPION with 4.2 nm cores and a hydrodynamic diameter of 45-60nm. Its $r_2$ and $r_1$ relaxivities are 151 and 25.4 $mM^{-1}sec^{-1}$. The production of Ferumoxides was terminated in 2009 due to its inconsistent performances comparing to macromolecular gadolinium based contrast agents. Both SPIONs have very broad size distributions with $\sigma \geq 80\%$, as shown in Figure 1.1 [47]. The broad size distribution results in an inconsistent enhancement on MRI because the relaxation time is strongly dependent on the particle sizes, as shown in Figure 1.2 [47,49–51].

The broad size distribution of SPIONs also results in undesired offsite accumulation and low target accumulation. This results in high background noise signal with undesired side effects, such as back pains and headaches, reported by Bayer HealthCare Pharmaceuticals Inc. These effects are minimal for macromolecular based gadolinium contrast agents. However, Gadolinium based MRI contrast agents have toxicity concern due to leach of gadolinium ion from the complex [52,53]. In fact, researchers start to focus on Gadolinium oxide based nanoparticle as MRI contrast agent recently for a safer alternative, but offsite accumulations will become one of its major concerns [54]. In comparison, the low toxicity SPIONs become extremely attractive as a clinical substitution, particularly for patients with kidney diseases [53]. Both magnetic nanoparticles must rely on a controlled particle size distribution to avoid the particle size variability. Monodispersed SPIONs will increase the accumulation of SPIONs in the targeted area, which further improves the MRI contrast. Therefore, monodispersed particles are the foundation for applicable, safer and higher contrast MRI agents for both iron oxide and Gadolinium based agents. This means the broad size distribution of current particles must be resolved.

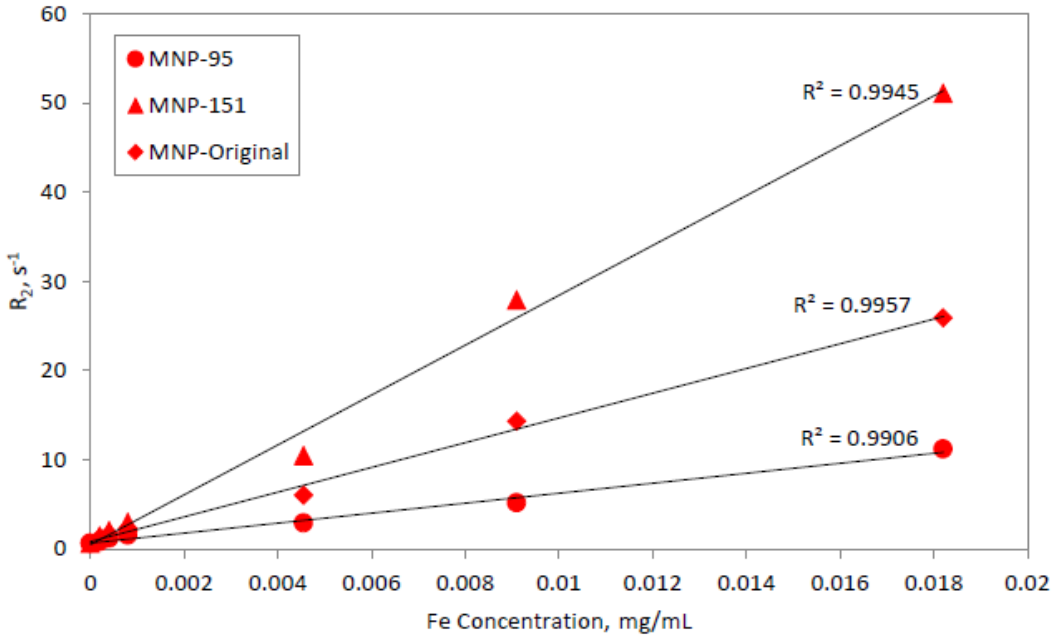


Figure 1.2. T2 relaxation rate of different sized particles with different concentrations, which particle size average are 95, 151, and 100 respectively for MNP-95, MNP-151 and MNP-Original SPIONs [49]. This figure is reprinted with permission.

## 1.4: Particle size effects on magnetic hyperthermia treatment

Magnetic hyperthermia treatment (MHT) is one type of medical therapy to weaken and destroy cancer cells by using a high temperature environment. The process involves magnetic nanoparticles to induce thermal energy. Magnetic nanoparticles response to an external alternating magnetic field and thus generating a localized heating effect. However, heat localization is the a major challenge for MHTs because it determines treatment localization and therefore efficiency [55–57].

Most MHT studies use MSPIONs by the reason of their significantly higher heat transformation in comparison with single-core SPIONs [27]. Yet, MSPIONs have a broad size distribution of $\sigma \geq 20$ %, where $\sigma$ is the standard deviation of particle size distribution divided by the average particle size to represent particle size distributions independently from their particle average sizes [26–28]. The broad size distribution of SPIONs strongly affects their biodistribution and therefore reduces their treatment efficiency and localization [58,59]. Therefore, the MHT treatment is usually initiated with a direct injection of SPIONs into the tumor. Recently MHT showed successful results with Magforce (Nanotherm®) in the first clinical trials on prostate cancer, and approved by the European Medicine Agency [60,61].

The MHT with Magforce® involved direct injection of 4-12 ml of 112 mg Fe/ml of 100 nm aminosilane SPIONs with 15 nm cores into the tumor area [62]. Usually, MHT requires various additional treatments to improve the treatment performance, such as laser, microwave, radiation or other anticancer treatments, but most of them lead to harmful or fatal side effects [63–65]. Therefore, the treatment requires real time temperature control to ensure efficient treatment and avoid undesired effects [60,66]. After the clinical trial, it was stated that homogenous distribution of nanoparticles was the key for future MHT improvements [60,66].

The heating efficiency must be improved for a safer and more material efficient MHT by reducing the need of high dosage injection to the target tumor. SPIONs with narrower size distribution provides a more efficient heat generation than SPIONs with a broader size distribution [67–71]. However, the production of monodisperse SPIONs is unachievable by the current technology. On the other hand, **Error! Reference source not found.** showed inhomogeneous SPION d istribution with very few particles traveled into the tumor region and resulted in a poor heat transformation. The SPIONs penetration through a physical barrier can be improved by low frequency alternation magnetic fields [72,73]. The effect can be further improved by monodisperse SPIONs as shown in Figure 1.3. In additional, chances of SPIONs internalization are also increased once SPIONs are near the cancer cell surface, which will result in significant decrease of the cancer cell survival rate by 40%, as shown in Figure 1.4 and Figure 1.5 [70]. Therefore, highly size controlled multi-core SPIONs is the foundation for future MHT improvements.

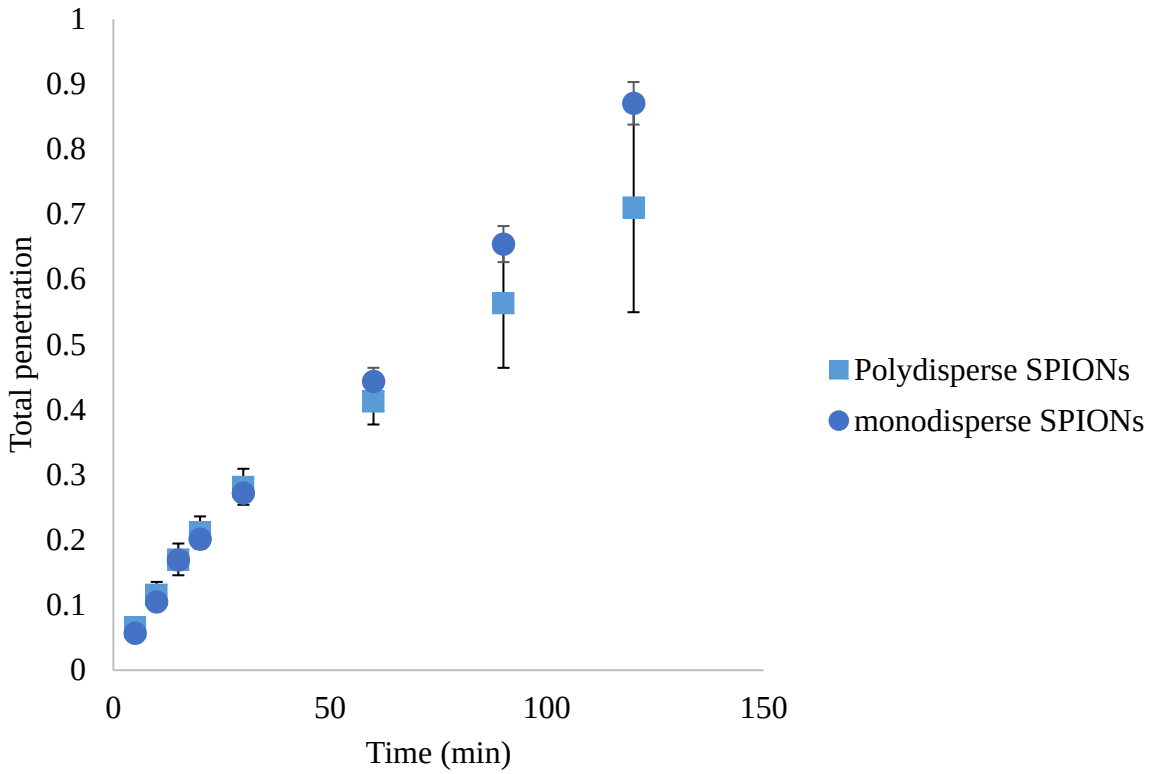


Figure 1.3. SPIONs with different size distributions penetrated through a 1μm membrane with a 7 Hz alternating magnetic field.

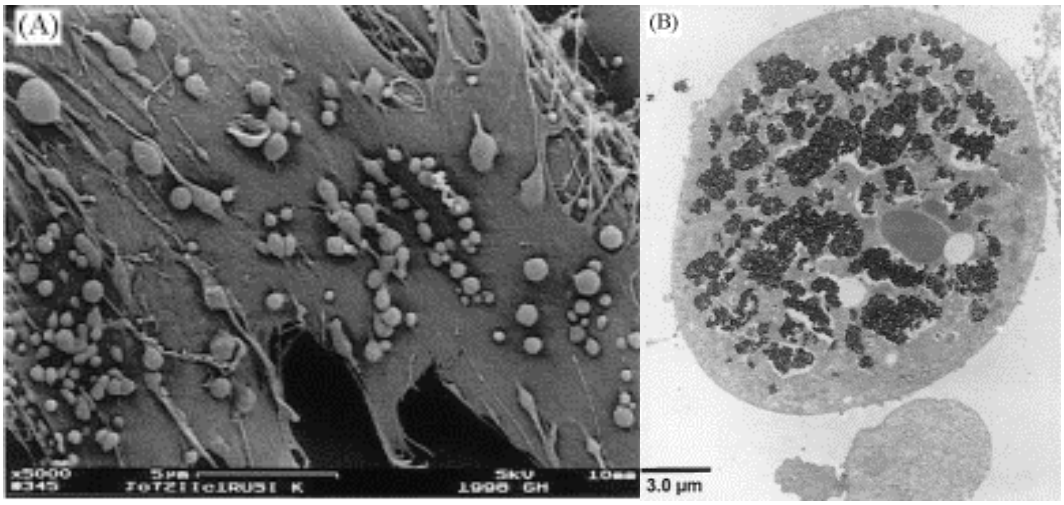


Figure 1.4, (A) Scanning electron microscopic (SEM) of SPIONNs on cell surface. (B) Transmission electron microscopic (TEM) of SPIONs aggregation on cell surface [70]. This figure is reprinted with permission.

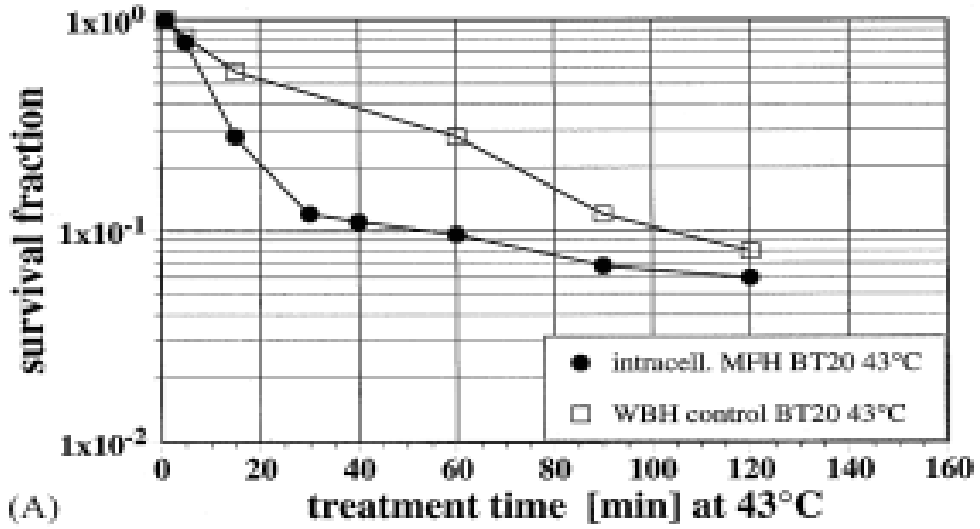


Figure 1.5, intracellular hyperthermia cell survival rate (black dots) and extracellular heating survival rate (white dots) [70].

1.5: Review of magnetic nanoparticle size selection methods

As mentioned in the previous sections, SPIONs with diameters greater than about 20 nm are generally synthesized with multi-core structures held together by an external matrix. This typically yields particles with a very broad size distribution with DLS PdI of above 0.3 [8]. This broad size distribution hinders clinical translation of these particles due to safety concerns and performance variabilities. In fact, there were multiple attempts to narrow SPION size distribution in the past two decades, but none of them were controllable and scalable, including vacuum filtration, gel chromatography, centrifugation separation, and magnetic fraction technique (MF).

Quantifying size distribution is not an obvious job by comparing data between different measurement methods. Currently, there are no optimal means to measure the size distribution of nanoparticles for different applications. In general, monodisperse nanoparticles are particles that have a $\sigma \leq 5\%$ standard deviation by its mean size, or a PdI value lower than 0.1 [75–78]. None of the currently used SPIONs have reported a monodisperse size distribution within the range even in a small quantity for research purpose.

Gel chromatography and vacuum filtration techniques have their limitations in scaling-up and generating multiple fractionations from a polydisperse distribution [5,6]. Both processes utilize particle mobility differences to separate different sized particles through material matrixes by a filter or gel. Particles were hard to be recovered from the matrix to produce multiple fractionations. Moreover, the separations were limited by the homogeneity of the pore size and the structure of matrix material, which maybe the reason for the large size distribution, as shown in Table 1.1.

Centrifugation was able to generate multiple particle separations by applying different rotational speeds [4]. The process utilizes centrifugal forces to separate different sized particles into two layers which consist of suspended particles and aggregated particles. It is difficult to have a

complete removal with only the suspended particles without the aggregated particles, which may also cause large size distribution as shown in Table 1.1.

The MF technique has its potential for large quantity of production, but it has the worst size distribution controllability among all three methods, shown as in Table 1.1. The concepts and methods will be discussed in the following sections.

| Separation method | Average size (nm) | | Core | Size measurement method | Size distribution | | Coating molecule | Application/notes | Ref. |
|---|---|---|---|---|---|---|---|---|---|
| | Ori. | Sep. | (nm) | | Ori. | Sep. | | | |
| Gel Chromatography | 72 (DLS) | 11.4 | 4-7 | TEM | NA | ± 6.3 nm | Dextran | MRI contrast agent | [7] |
| MF | 34.4 | 7.7<br>14.4<br>28.8<br>37.7<br>44.4<br>47.7<br>68.8 | 3 | DLS (z) | PdI ~ 0.35 | PdI ~ 0.27 | Carboxydextran | Size separation | [8,9] |
| Vacuum Filtration | 121 (Feridex) | 15.1 | NA | DLS (z) | broad | PdI = 0.2 | Dextran | MRI contrast agent | [5] |
| Centrifugation | NA | 65.5<br>38.9<br>23.1<br>18.5 | NA | DLS (v) | broad | ± 14<br>9.1 6<br>4.4<br>nm | SiO2 | MRI relexivity comparison | [4,10] |
| | ~6 (n),<br>~19 (v) | 14.9<br>13.2<br>12.1<br>7.3 | | XRD | | NA | | | |
| | ~13 (n),<br>~20 (v) | 24.2<br>20.0<br>15.8<br>10.5 | | TEM | | ±<br>2.4-<br>3.6<br>nm | | | |

Ori.: original samples before any size separations

Sep.: size separated samples

(n): number weighted measurement

(v): volume weighted measurement

(z): z-average size

NA: not available

broad: $\sigma \geq 80\%$

Table 1.1. Comparisons between current separation methods for SPIONs.

The magnetic fractionation, MF, technique was suggested by Thomas Theinländer et al in 2000 [8]. The method was designed as an approach to study particle size effect on different size SPIONs, including blood half-lives, and MRI relaxivities [7,79,80]. The separation started with a strong magnetic force and captured all SPIONs. Once all the SPIONs were captured by the magnetic field, a fluid flow was introduced to the SPIONs. Smaller size SPIONs were released from the field due to weaker magnetic attraction. The magnetic field strength then decreased stepwise and generated multiple fractionations with different sized particles.

However, multiple populations were usually observed with MF-SPIONs (magnetic fractionated SPIONs) and resulted in a broad size distribution with high PdI values, as shown in Figure 1.6.The multiple populations remain the same before and after sonication or additional MF processes. The hypothesis was that larger SPIONs were blocked by smaller SPIONs from reaching the magnetic source and therefore had a weak magnetic attraction. Smaller SPIONs that were close to the surface of the magnetic source aggregated on the surface faster than larger SPIONs because of their shorter distance, and blocked the late comer larger SPIONs to reach the surface of the magnetic source even with larger magnetic contents, as shown in Figure 1.7. The larger SPIONs were forced to be immobilized away from the magnetic source because of a weaker magnetic attraction, and therefore they were released with the smaller SPIONs when the magnetic field decreases and vice versa. In fact, SPIONs were clearly separated by their average size in the system, but their PdI only decreased slightly from about 0.35 to about 0.27 [8]. The size distribution was not improved significantly and the fractionated particle was still polydispered in multiple studies [80,81].

The effects of the broad size distribution of MF-SPIONs was observed in different follow up researches. The blood half-lives of MF-SPIONs can be extracted from a study done by Thomas Allkemper et al, 2002 [80]. The study reported a MRI contrast drop over time by different size MF particles in rabbits with MF-SPIONs separated from SHU-555 SPIONs. The changes of MRI

relaxation time were due to the changes in average size of different MF-SPIONs. Unfortunately, even the smallest MF-SPIONs with an average size of 21 nm had blood half-lives in enhancement performance only around 15~25 minutes. This result is a huge difference comparing to studies done by vacuum filtration and gel chromatography methods, which showed strong size dependency of blood half-lives. Karen C. Briley-Saebo al et reported a huge blood half-live increment from 0.46 h to 15.9 h in rabbits after Ferumoxides was fractionated by vacuum filtration into 20 nm [5]. Similar result was observed in rats, blood half-live had an increment from 6 min to 81 min by filtrating through gel chromatography [7,82].

The significant difference in results might come from broad size distribution of MF-SPIONs due to poor separation performance. Both gel chromatography and vacuum filtration methods significantly provide narrower size distribution SPIONs comparing to the original broad size distribution, while MF did not, as show in Table 1.1. MF was used as a supplemental size selection treatment for different synthesis to produce different sized particles, but none of them reported a significant improvement in results [81,83,84]. Particle size distribution is a very important factor for blood half-lives and therefore a new size fractionation method is needed for biomedical applications.

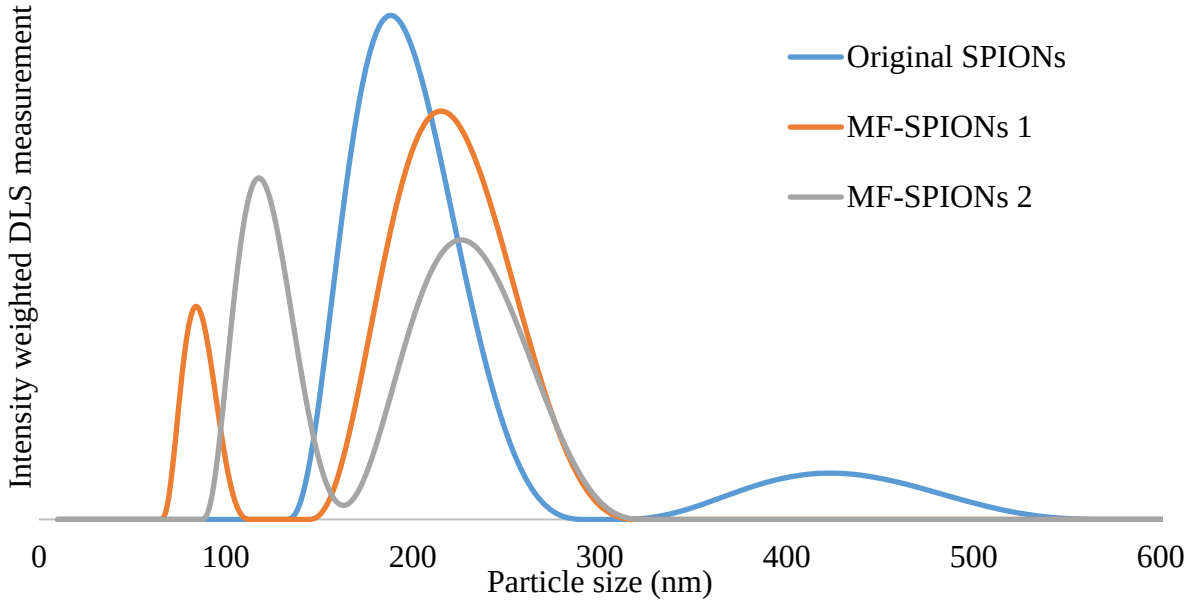


Figure 1.6. Intensity weighted DLS measurement of MF- SPIONs and their original SPIONs.

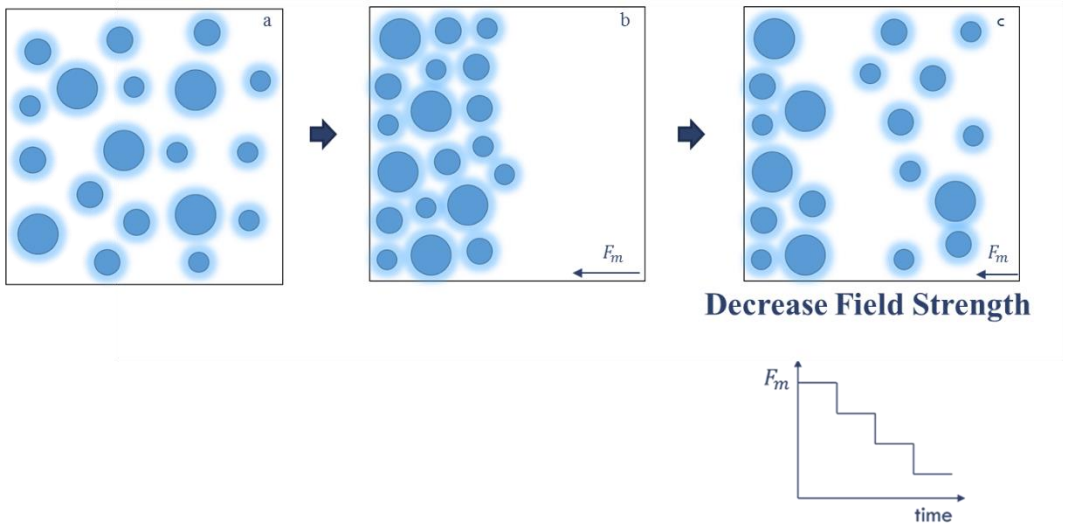


Figure 1.7. Illustration of MF mechanics of magnetic fractionation.

## Chapter 2 : Diffusive magnetic fractionation (DMF)

### 2.1: Abstract

Multi-core superparamagnetic iron oxide nanoparticles (SPIONs) have enormous potentials in biomedical applications, including drug delivery, magnetic hyperthermia treatment, and magnetic resonance imaging. Unfortunately, broad size distribution of SPIONs causes safety concerns resulted from major performance variabilities. Therefore, a new size fractionation method, diffusive magnetic fractionation (DMF), was introduced to improve the size homogeneity of SPIONs. The DMF method utilizes a pulsed magnetic field approach to separate SPIONs by their size differences. The currently available SPIONs have broad particle size distributions with measured polydispersity indices (PIs) about 0.15~0.2. On the other hand, explicitly controlled SPIONs with an average PI of 0.08 were acquired by the DMF. The result is significantly better than the conventional magnetic fractionation method which gave a PI of 0.17. Furthermore, the average size of DMF fractionated SPIONs can be predicted by mathematical models. The experimental results eminently matched our models with a $R^2$ value of 0.98 and therefore fractionated SPIONs with desired sizes can selectively be produced. Besides, the DMF method showed a high particle recovery, scalability, and reproducibility, which are difficult to achieve with conventional methods.

### 2.2: Introduction

Superparamagnetic iron oxide nanoparticles (SPIONs; $Fe_3O_4$, $\gamma$-$Fe_2O_3$) are commonly used for clinical and biomedical applications because of the combination of their magnetic and biocompatible properties [85,86]. A challenge to broader adaptation of SPION-based biomedical technologies, however, is strongly related to particle size distribution. Almost all SPION applications involve processes of delivery which material or energy are transported to a particular

biological entity [27,47,87,88]. The delivery performance is strongly related to its bio-distribution and pharmacokinetics, which are influenced by particle sizes, and therefore particle size distributions [11,37,89]. Unfavorable secondary effects of SPIONs such as shock, chest pain, and back pain were reported to the FDA and performance variability were observed in clinical studies [1–3]. This phenomenon is believed to be due to their broad particle size distribution. Thus, narrowing down the particle size distribution is a major challenge for current SPION based applications. Therefore, we are introducing a new technique, named diffusive magnetic fractionation (DMF) to provide SPIONs with controlled narrow size distribution.

The largest particle size of a single-core SPION is around 26-30 nm because larger particles form multiple magnetic domains and become ferromagnetic [14,90]. The superparamagnetic characteristic is especially important to maintain particle stability for biomedical applications [91]. For most synthesis methods, a critical size of 15-20 nm is used to ensure superparamagnetic characteristics at room temperature [18,92]. Therefore, SPIONs with multi-core structures are commonly used for applications that require particle sizes larger than 20 nm, including most drug delivery, MRI, and tumor targeting applications [6,93]. These SPIONs usually contain 5-15 nm iron oxide cores held together by long chain polymers and this results in random shapes and broad size distributions [5,47,94].

Conventional separation methods for purification, such as density gradient centrifugation, vacuum filtration, size exclusion gel chromatography (SEC) and magnetic field flow fractionation methods (MF), have limited control on average particle sizes and particle size distributions [4–7,9,10,95–99]. The DMF utilizes the differences in diffusivity and magnetic mobility of differently sized particles by a pulsed magnetic field (PMF), which unlike the conventional MF approaches based on a constant magnetic field. During the magnetic pulses, the magnetic field creates strong magnetic attractions to SPIONs and pull them closer to the source of the magnetic field. Between

pulses, it allows SPIONs to freely diffuse away from the source in the absence of a magnetic field. After multiple cycles, variously sized SPIONs are separated by their different attraction and diffusion rates. A layered structure of differently sized SPIONs are eventually formed and maintained with a constant magnetic field. The magnetic field will then be decreased stepwise to release differently sized SPIONs layer by layer.

Nanoparticle size distributions are usually reported by imaging measurements or dynamic light scattering (DLS) measurements. Imaging measurements, such as transmission electron microscopy (TEM), scanning electron microscopy (SEM) or other microscopy approaches, involve image analysis tools to select objects of a specific geometry or size range. Its calculated coefficient of variation is called σ or $C_v$. For randomly shaped particles, like SPIONs, it is very difficult to calculate σ accurately [26]. Also, most microscopy approaches require their sample to be in a dry condition and this introduces major particle aggregations. On the other hand, DLS provides a polydispersity index (PI) to represent the randomness of its measurements. The DLS measurements utilize cumulants analysis to estimate the translational diffusivity and calculate the corresponding hydro diameter with Stokes-Einstein relationship (ISO13321, 2017). A single exponential fit is used in the cumulants analysis, where the first order fitting parameter gives the average of measurements, Z-average size, and the second fitting parameter gives the distribution of measurements, known as PI. PI is selected to compare different particle size distributions in this study because it provides more objective and efficient measurements compared to image analysis. Also, SPIONs are measured in a fluid suspension with DLS approaches, which is the form used by most applications.

The DMF is designed to provide SPIONs with tightly controlled particle size distribution to reduce performance variability and safety concerns. The broad particle size distribution is a result of its multi-core structure, which is very difficult to be improved with currently available

purification methods. The performance of the DMF was measured by a DLS method because it is most applicable for biomedical applications.

2.3: Results and discussion:

**SPION size distribution control through different approaches.**

The DMF is developed as an improvement of conventional MF approaches. The DMF process uses a PMF and a magnetic column. The magnetic column is packed with soft iron beads to increase its surface area and its induced magnetic gradient. The DMF begins with the magnetic column filled with aqueous SPION suspension, while the exit of the magnetic column was blocked to prevent leakage. The magnetic column is placed inside an electric coil which provides an PMF to magnetize the iron beads periodically, as shown in Figure 2.1(a) - (c). When the beads are magnetized, SPIONs are attracted toward the surface of the iron beads. When the iron beads are demagnetized, SPIONs diffuse freely away from the surface. After multiple cycles, differently sized SPIONs are separated due to their mobility difference during magnet attraction and diffusion. Larger SPIONs have a faster magnetic attraction rate and a slower diffusion rate than smaller SPIONs. Moreover, the PMF slowly increased its magnetic field strength every cycle so that larger SPIONs are the first to be captured. Once the PMF reaches the maximum strength, the magnetic field strength is maintained constantly to immobilize all SPIONs to the surface. SPION piles are expected to form layers on the surface, and larger SPIONs are closer to the surface than smaller SPIONs. The magnetic field is then decreased stepwise to release differently sized SPIONs layer by layer. Small SPIONs are released first because of their weak magnetic attraction caused by both their low magnetic content and positioned far away from the surface. A hydraulic pump provides a fluid flow to carry released SPIONs from the magnetic column to a collector column which was magnetized by a strong permanent magnet, as shown in Figure 2.1(d).

The result of DMF was compared with that of conventional MF. MF was performed according to literature with minor alternation for the comparison [8]. The modified MF separation process starts with a strong magnetic attraction and captured all SPIONs from a gravity driven

fluid flow with a magnetic column. Once the fluid flow turns clear and all SPIONs are immobilized by the magnetic column, the flow was then driven by a pump instead of gravity to maintain the flow. Afterwards, the external magnetic field is decreased stepwise and small SPIONs are released from the column due to their weak magnetic attraction, as shown in Figure 2.2. The MF showed very limited improvement on controlling particle size distribution, resulting from its unorganized particle pile formed by the applied constant magnetic field. Some larger SPIONs far away from the surface cannot enter the inner region of the pile because the space is occupied by smaller SPIONs closed to the surface. These larger SPIONs were eventually released with smaller SPIONs due to their weak magnetic attraction caused by their longer distance to the surface, as shown in Figure 2.2.

Other than the use of PMF, another major difference between DMF and the MF is the motion of SPIONs when a magnetic field is applied. SPIONs are captured from a gravity driven fluid flow in MF and they are captured from a motionless fluid body in DMF. Therefore, DMF with no PMF cycles is included to study the effect of capturing mechanisms. For the following study, DMF0 and DMF9 refers to DMF with 0 and 9 PMF cycles.

Commercially available polydisperse $105 \pm 1.7$ nm starch-coated SPIONs with an average PI of 0.24 were separated into 9 fractions by the MF, DMF0, and DMF9 to compare their separation performance on a polydisperse sample. Each of the 9 fractionations of MF, DMF0, and DMF9 was performed at the exact same magnetic field strengths for fair comparisons. Their corresponding fractionated SPIONs were named MF-SPIONs, DMF0-SPIONs, and DMF9-SPIONs. The fractionated SPIONs were measured for their Z-average size and PI by DLS measurements. The samples prepared by all methods exhibited significant changes in average particle size among fractionations. All three methods produced SPIONs in the range of 70-120 nm, as shown in Figure 2.3. The 9 MF-SPION fractions have an average PI of $0.18 \pm 0.013$. The 9

DMF0-SPIONs fractions have an average PI of 0.14 ± 0.012. The 9 DMF9-SPIONs fractions have an average PI of 0.1 ± 0.01, as shown in Figure 2.4. DMF9 showed to be the best fractionation method with narrowest size distribution among three MF techniques. Furthermore, DMF9 produced a fractionation with the smallest average size which indicated that most larger particles are retained by the magnetic column and therefore only the smallest particles were released from the system.

The limitation to control SPIONs size distribution was investigated. Starch-coated SPIONs with PI of 0.24, 0.16, and 0.09 were obtained from merchant, which showed the lack of control of particle size distribution of current purification process. All three types of SPIONs were separated by the MF, DMF0 and DMF9 to observe their performance, as shown in Figure 2.5. The MF showed very little to no improvement on particle size distribution when the original sample have a PI value of 0.16 or lower. On the other hand, the DMF9 showed most significant improvement on all three samples, while the DMF0 also showed an intermediate performance between the MF and DMF.

**More than 95% of the particles were recovered from DMF processes.** The DMF retains the advantages of the MF, such as scalability and high particle recovery in addition to the significant improvement in performance. The particle recovery of the DMF was measured by Ferrozine assay, which the iron content of samples was measured before and after the DMF process. Polydisperse SPIONs with 0.4 mg of iron were separated into 8 fractions of DMF-SPIONs with total 0.38 mg recovered. The DMF-SPIONs results indicated a 95% particle recovery by mass and a mass weighted average size of 90.8 nm. With the assumption of constant density, mass is in proportionality to volume. It was very close to the measured volume weighted average size of 89.7 nm of original SPIONs before the DMF separation, as shown in Figure 2.6.

**Mathematical models showed a strong agreement with DMF9-SPIONs.** Mathematical models are used to predict the average size of DMF-SPIONs and study to separation mechanisms. The DMF is simplified into an interaction between magnetic attractions and hydraulic drags. The magnetic attraction force act on a single SPION can be calculated as following.

$$F_m = \nabla(m \cdot B)$$

$$F_m = \nabla\left(\frac{4}{3}\pi R_{np}^3 \rho\chi\vec{H} \cdot \mu\vec{H}\right)$$

$F_m$ is the magnetic attraction force, $m$ is the magnetic moment of SPIONs, and $B$ is the induced magnetic field generated by a single iron bead. $R_{np}$ is the radius of SPIONs which were measured by DLS. The coating thickness of SPIONs are assumed to be negligible. ρ is the density of SPIONs, $\chi$ is the magnetic susceptibility, and $\mu$ is the magnetic permeability. $\chi$ is estimated by SQUID (superconducting quantum interference devices) measurements. $\vec{H}$ is the magnetic field calculated from the Legendre function with sphere boundaries. The magnetic force field around a single iron bead can then be calculated accordingly.

On the other hand, the hydraulic drag is calculated from stroke's drag. The Reynold number is calculated to be 12.5 and therefore Newtonian flow is assumed.

$$F_d = 6\pi\eta R_{np} v$$

$F_d$ is the stoke's drag force, $\eta$ is the fluid viscosity, and $v$ is the fluid velocity. The two forces are combined to calculate the maximum capacity $C_M$ of a given external magnetic field and particle size. $C_M$ is calculated by integrating the volumes near the bead surface when $F_m > F_d$, which immobilizes SPIONs by the magnetic attraction, as shown in Figure 2.7. $C_M$ is a function of external magnetic field strength and particle size fitted as following.

$$C_M = 0.12 + 0.05 \cdot \ln(12500 * B + 2.4) + 2 \cdot 10^{-9} \cdot \left(R_{np} - 125\right)^3$$

The fitting inputs have units in Tesla and nm. This fitting equation is efficient to predict the

DMF process for starch coated SPIONs with a $R^2$ of 0.91. The equation is used to calculate the change in $C_M$ between different conditions. The magnetic field intervals to fractionate SPION of a certain size can be predicted based on a known particle size distribution and an assumption that particles are perfectly sized into layers. For example, 90 nm starch coated SPION can be separated in the region between 20 and 15 mT. The prediction is extremely accurate with a $R^2$ value of 0.98, as shown in Figure 2.8. The models also confirmed our assumption that particles are sized into layers. The same model can be used for SPIONs with different concentration and physicochemical properties, such as surface modifications, size distribution or shapes, but the fitting parameters are expected to be different.

**Separation of DMF9-SPIONs with different surface modifications was validated**. Polydisperse SPIONs with starch, amine, and 5k MW PEG (polyethylene glycol) coatings were separated by a DMF9 process. All polydisperse samples could be separated and produce DMF9-SPIONs with PI lesser than 0.1. However, SPIONs with different surface modifications require different external magnetic field strength. For example, to fully immobilize 1 mg Fe of starch, amine, and 5k MW PEGylated SPIONs, it required 12, 24, and 34 mT respectively. Stronger magnetic attraction is needed to overcome stronger inter-particle repulsions resulted from different surface modifications. Aminated SPIONs has positive charge on particle surface with Zeta potentials measured to be +45 ± 2 mV. The positive charges create electrostatic repulsion between particles. On the other hand, the bulky PEG polymers create steric repulsion between particles.

PEGylated SPIONs were produced by modifying aminated SPIONs, which came from starch coated SPIONs. The DMF was performed on each selected stage of the three surface modification stages and therefore separated starch coated, aminated, and PEGylated SPIONs were generated. Then, these three SPION samples with DMF treatment at different stage of surface modification process were all modified to PEGylated SPIONs. No significant difference was

observed in all three PEGylated SPIONs. Therefore, the DMF can be performed at any stage of the surface modification process based on research preference.

**Scalability of DMF.** Scalability is an important advantage of the conventional MF process and the DMF inherits the same feature to produce large quantity of monodisperse SPIONs at low cost. The performance of the DMF was evaluated by its average PI values of 4 DMF9 separations. Four different magnetic columns were designed in four different volumes by column lengths of 0.25, 0.5, 0.75 and 1 ml to explore the potential issues from scaling up. Four DMF9-SPIONs were obtain with magnetic field strengths of 24, 16, 8, and 0 mT. The average PIs are 0.08, 0.07, 0.07 and 0.07 respectively, as shown in Figure 2.9. It implies that the DMF can be scaled up without compromising its performance.

## 2.4: Conclusion

We have developed a new particle size selection method, DMF, as an improvement from conventional MF approaches. Unlike filtration approaches, polydisperse SPIONs were fractionated into multiple monodisperse fractions, all of which can be used for applications, such as MRI, drug delivery, and magnetic hyperthermia. DMF demonstrated excellent control of particle size distributing while conventional MF only showed a small improvement. The particle recovery of SPIONs before and after the DMF process was 95%, which means almost all SPIONs were recovered. The DMF can accommodate SPIONs with different surface treatments with the same performance, which is flexible to fit different types of researches. The DMF is scalable and it demonstrated a linear relationship with the volume of the column. Moreover, mathematical models were developed that a desired average particle size and particle size distribution can be produced selectively.

2.5: Figures

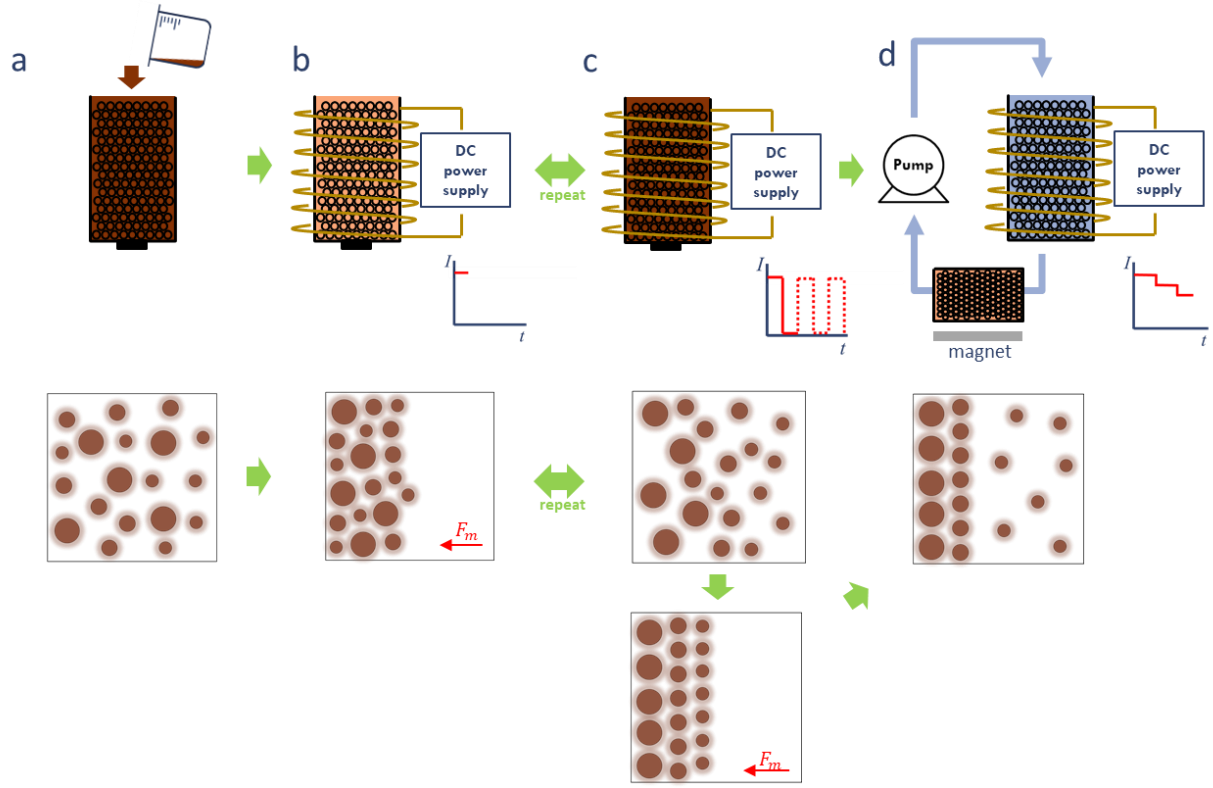


Figure 2.1. Illustration of the procedure for DMF. (a) The exist of a magnetic column is blocked and the column is fill with SPIONs suspension. (b) and (c) the magnetic column is magnetized by a PMF which SPIONs are captured and released repeatedly until and eventually forms layer as shown in the bottom. (d) The system is then connected to a hydraulic pump and a magnetized second column. The current is reduced stepwise to release multiple fractionations. The fractionations will be carried by the moving fluid flow to the second column captured and removed from the system.

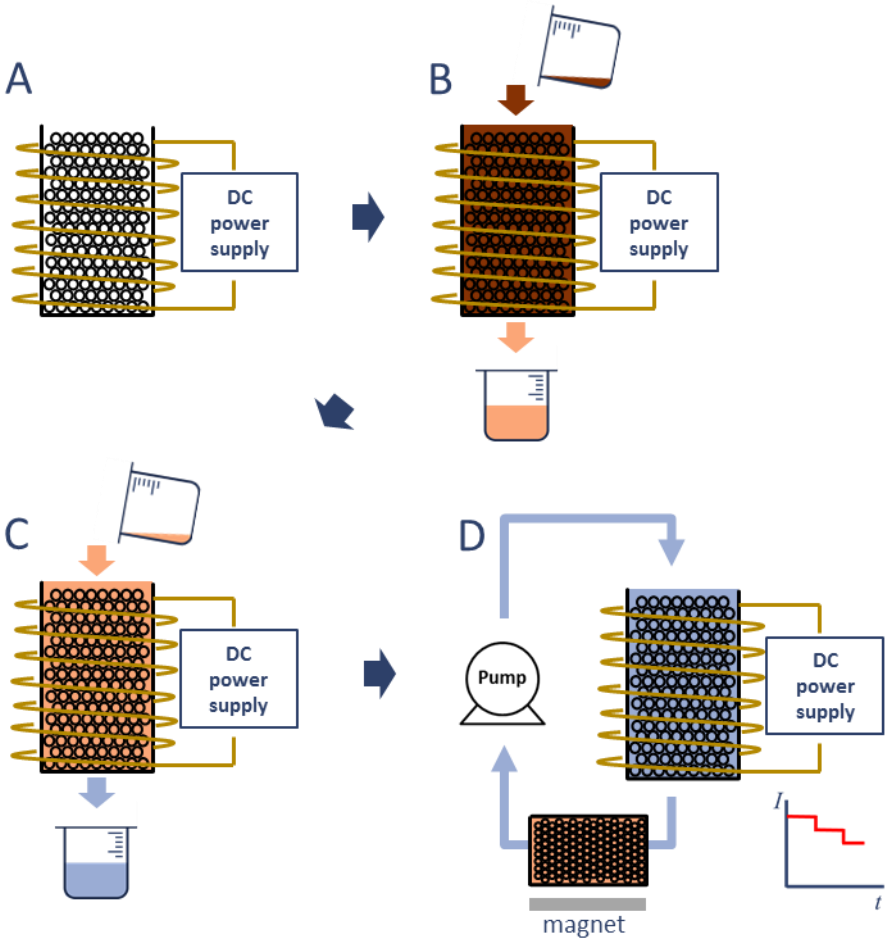


Figure 2.2. Illustration of the procedure for conventional MF with minor modification. (A) The magnetic column is magnetized before introducing SPIONs. (B) SPIONs are introduced with a gravity fluid flow. (C) The exit fluid adds back to the column until it turns clear and all SPIONs are captured by the magnetic column. (D) The column is connected to a hydraulic pump and a second column which is magnetized by a magnet. The current within the electric coil is reduced stepwise to create multiple fractionation.

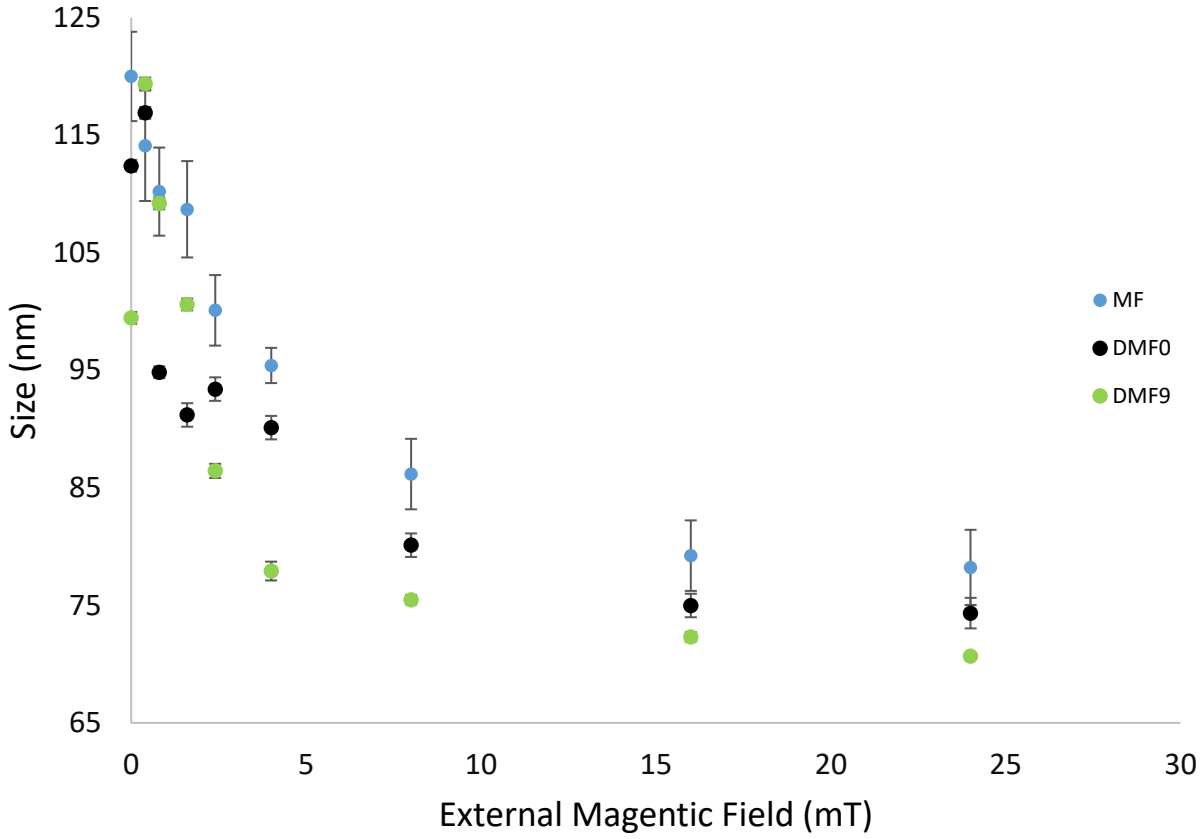


Figure 2.3. The Z-average sizes are reported by DLS measurements to estimate the hydrodiameter of SPIONs. The MF-SPIONs, DMF0-SPIONs, and DMF9-SPIONs all showed changes of average particle size between fractionations. However, DMF9-SPIONs have the most control is particle average size and a slightly wider range of particle average sizes.

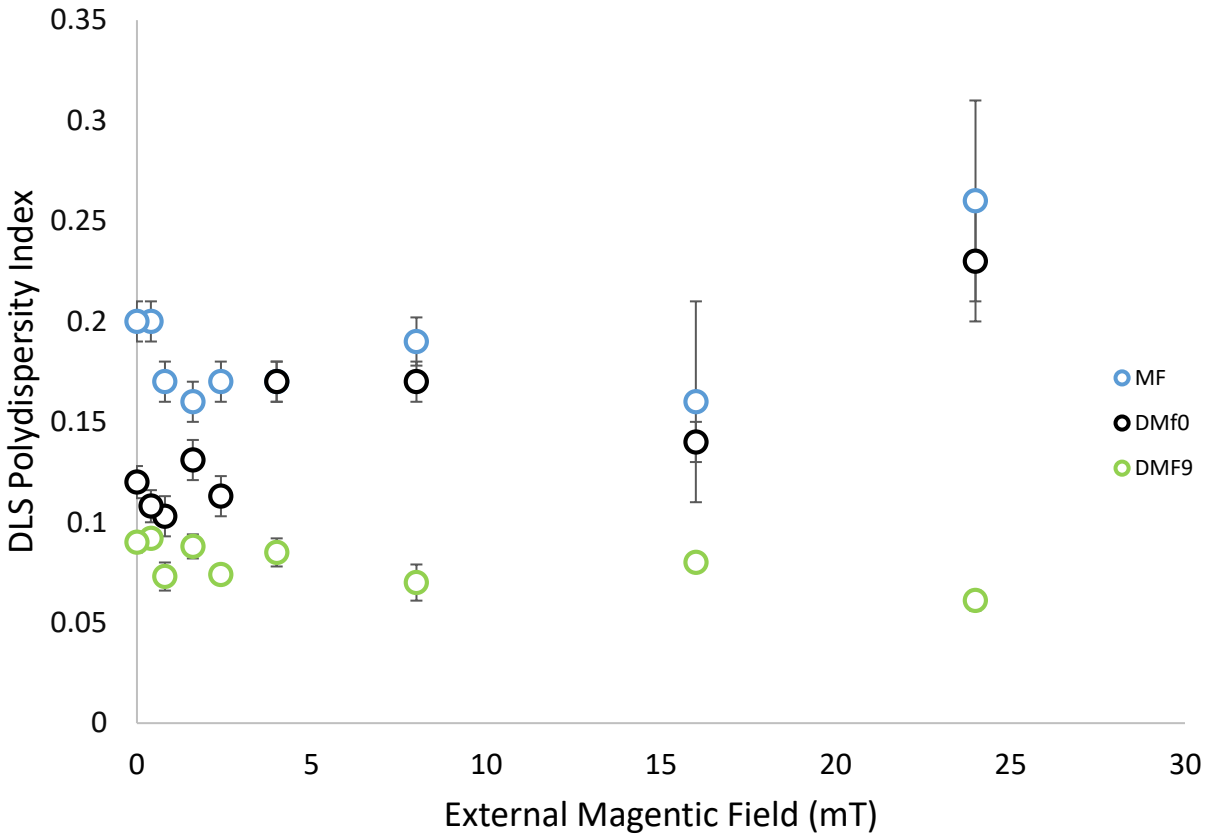


Figure 2.4. Comparison between the MF, SMF and the DMF methods. The PdI is reported by DLS measurements to estimate the particle size distribution. The MF-SPIONs and SMF-SPIONs had PdI values above 0.1 and the DMF-SPIONs fell between 0.05 to 0.1. PdI values below 0.07 are generally observed by monodisperse spherical nanoparticles.

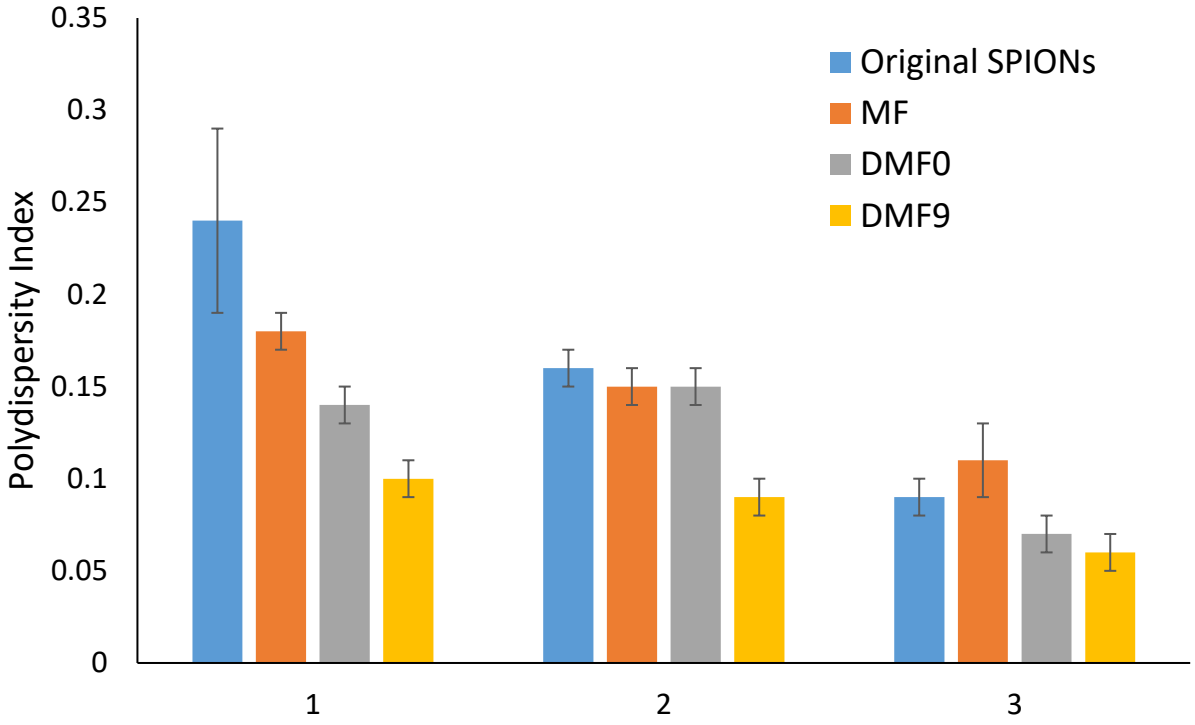


Figure 2.5. Illustration shows a comparison between MF, DMF0, and DMF9 methods. SPIONs with PI of 0.24, 0.16, and 0.09 were separated respectively by group 1, 2, and 3.

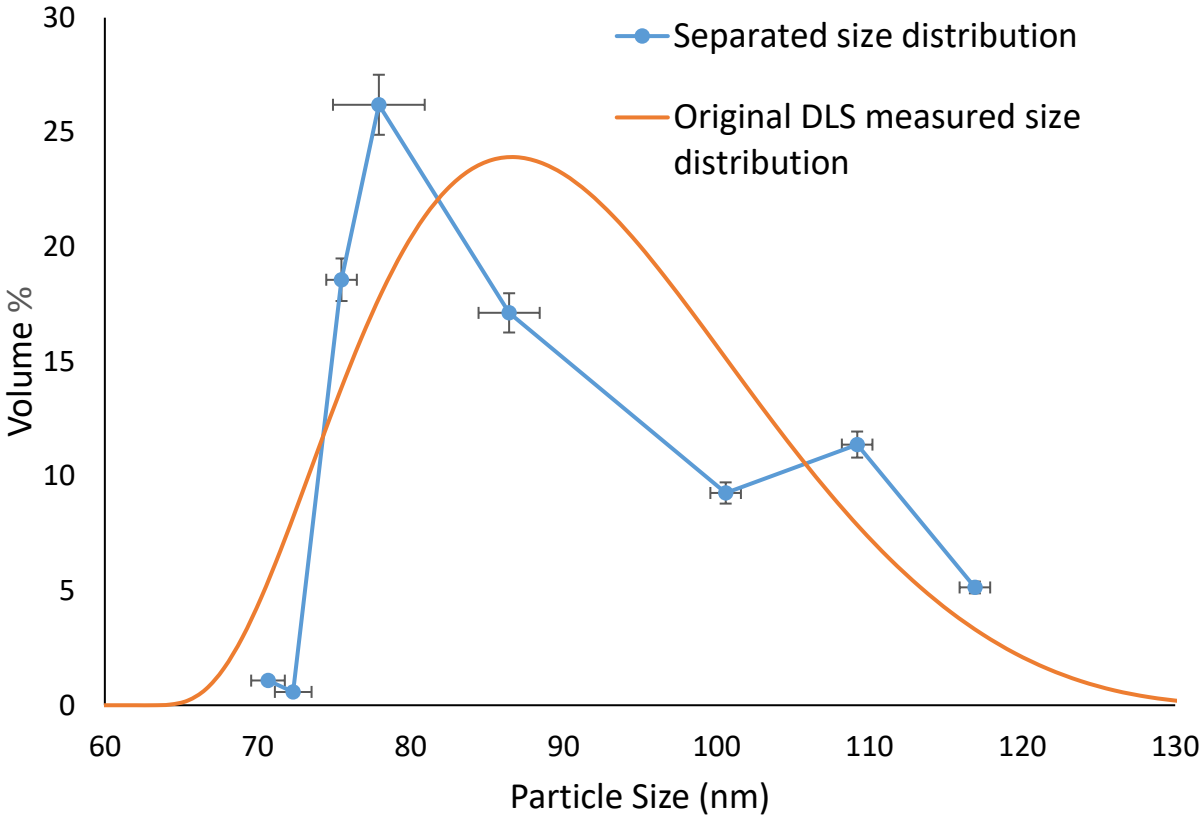


Figure 2.6. Particle size distribution of 100 nm starch coated SPIONs with a volume-weighted DLS measurement and Ferrozine assay from DMF-SPIONs.

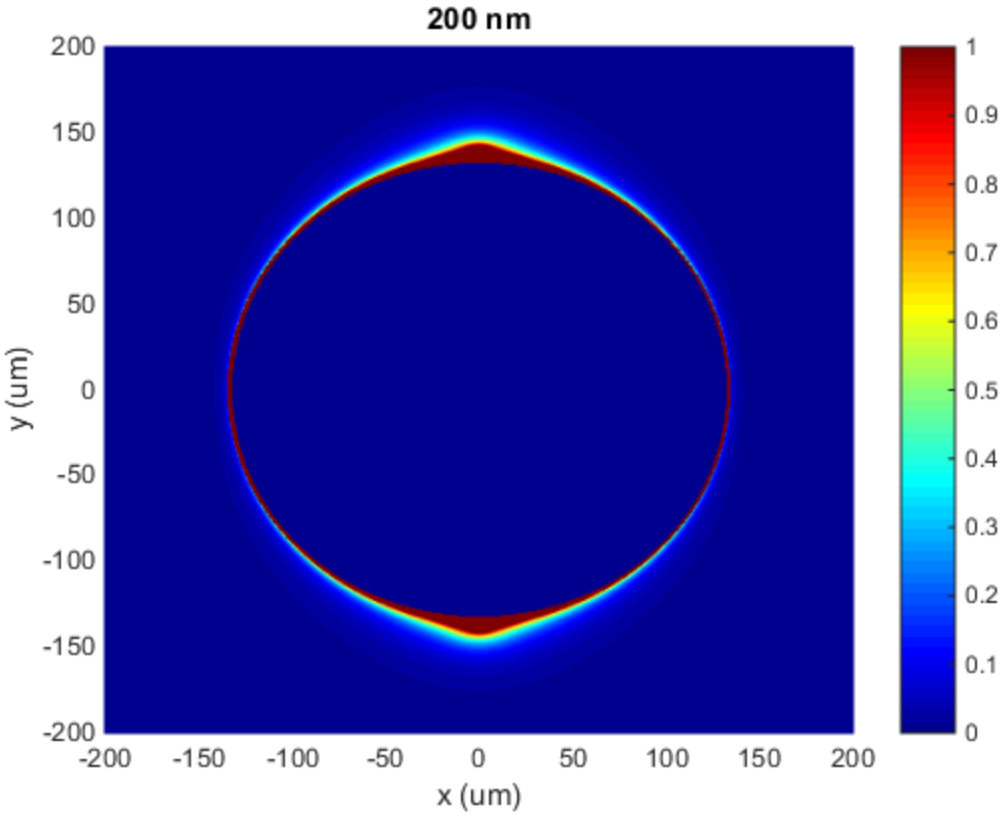


Figure 2.7. Illustration of an image of the combination of magnetic force and fluid drag force around a single iron bead. The intensity is calculated as $Intensity = \frac{Magnetic\ attraction}{fluid\ drag}$. In other words, volume with an intensity > 1 results in 200 nm SPION to be immobilized and intensity ≦1 will results in particle free moving with fluid flow and will be released from the system.

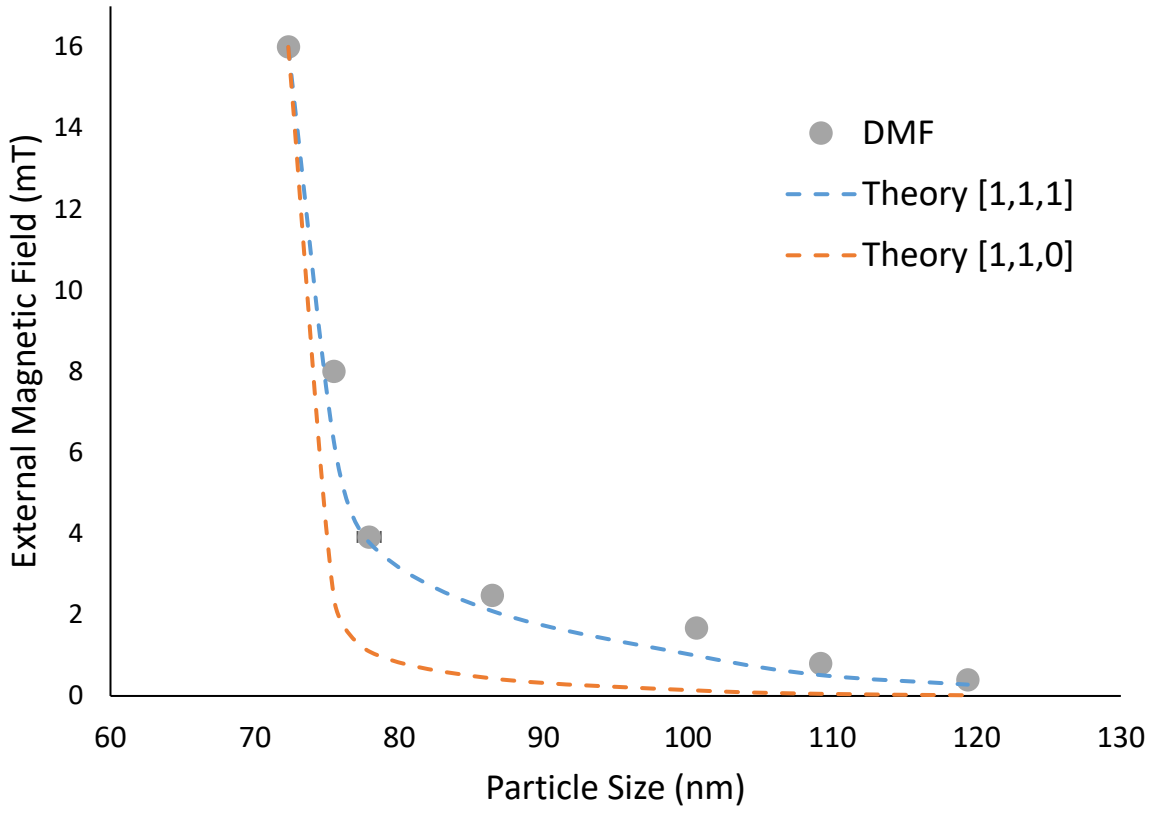


Figure 2.8. Theory and experimental plot of DMF-SPIONs from starch coated 100 nm SPIONs. Theory [1,1,1] and theory [1,1,0] are the Miller indices of iron crystals with two different magnetization directions. The actual crystal orientation is unknown, so both were considered in the mathematical models. The iron crystal with a [1,1,1] magnetization turned out to be the best fit for our system.

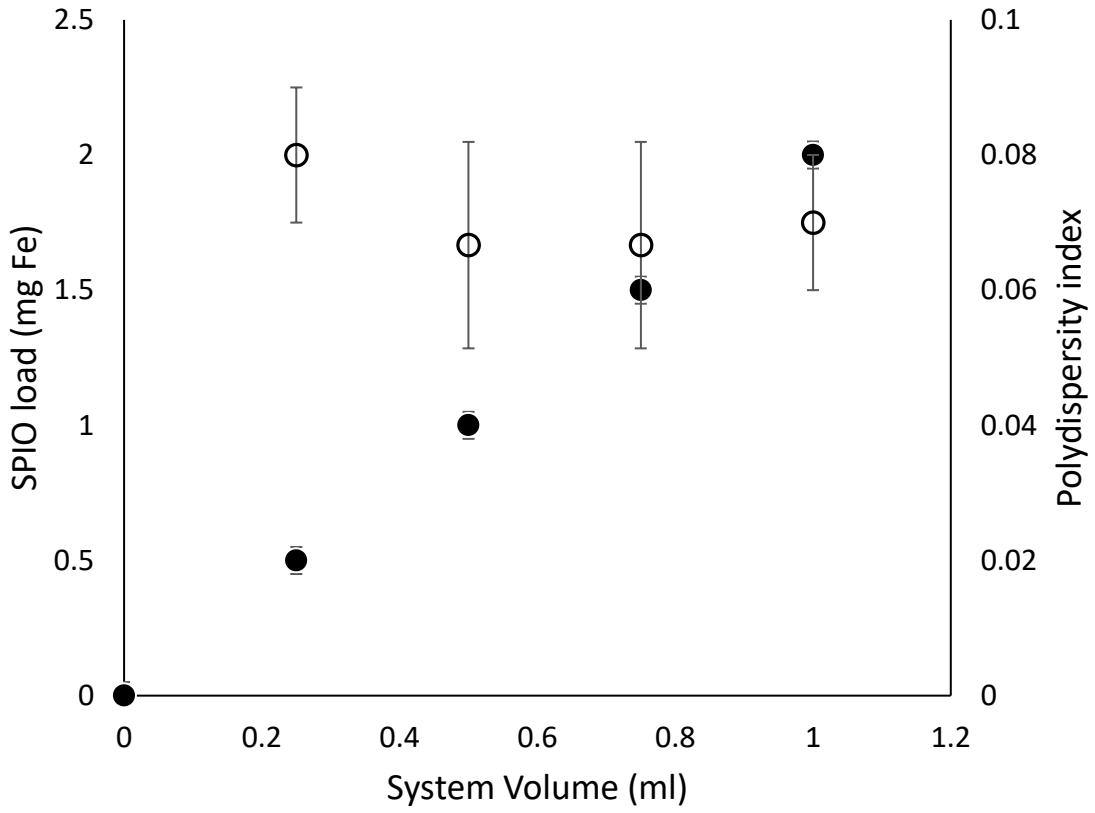


Figure 2.9. Illustration to show the scalability of DMF with 100 nm starch coated SPIONs and its corresponding PI performance with different system volume. The black dots are the SPIONs loading according to different system volumes and the white dots are their average PI values accordingly.

2.6: Material and Experiment

***SPION surface modification process*** was used to study the effects from different surface modifications. Starch coated SPIONs (FluidMAG-D; Chemicell, Germany) were cross-linked, aminated, and PEGylated according to previously published method [100]. The method started with 2 mL of starch coated SPIONs aqueous suspension (25 mg/ml) mixed with 2.6 mL of 6M NaOH (97%) for 15 minutes followed by adding 1.3 mL of epichlorohydrin. The mixture was placed on a shaker for 24 hours. Then the solution was dialyzed (Float-A-Lyzer G2, 8-10 kDa MW; Spectrum Laboratories, CA) for 24 hours. The dialyzed SPION suspension was then mixed with 2 ml of 30 ammonia at room temperature for 24 hours. These Aminated SPIONs could then be modified to produce PEGylated SPIONs. The PEGylation process was based on the use of mPEG-NHS (Nanocs; NY). A mixture of 300 300 µl DMSO, 300 µl water, and 300 µl phosphate buffer were made to dissolve 15 mg of mPEG-NHS. Then, 300 µL of SPION suspension was added into the mixture. The final solution was placed on a shaker for 24 hours at room temperature. The resulting PEGYlated SPIONs were eventually magnetically separated from its solution.

***Magnetic column***, an iron bead packed column LS Column Miltenyi Biotec, was used to increase system capacities. The column went through a 22W electric coil that was connected to a DC power supply (Hewlett Packard 6543A) to provide an external magnetic field.

***MF process with minor modification*** was used for the comparison with DMF. SPION aqueous suspension flowed through the magnetic column by gravity. The column was set at a constant magnetic field of 22 mT. Fluid was collected at the column exit and added back to the top of the column repeatedly until the fluid turned clear. Then a continuous aqueous flow in 1.5 ml/min was introduced into the system by a peristaltic pump and the field strength was decreased in stepwise manner to release a fractionation on each field strength decrement, as shown in Figure 2.2. During each decrement, the particles were collected from the flow output by a second magnetic column

magnetized by a 0.22 T magnet. Each fractionation took 5~8 minutes to collect. Then, the magnetic field was reduced again to give multiple fractionations.

***DMF process*** was used to homogenize SPIONs by their size differences. After polydisperse SPIONs solution fully filled the magnetic column, an input current was turned on and off periodically to provide a PMF in multiple cycles. Different PMF cycles and period parameters were used for differently sized and surface coated SPIONs. In general, a PMF with 2/2 (on/off minutes) was used for starch coated SPIONs. After the PMF process was finished, an aqueous flow ran through the column continuously with a flow rate of 1.5 ml/min, and then the magnetic field was decreased stepwise to release a fractionation at each decrement. The fractionations were collected until the aqueous solution turns clear, which was about 5~8 minutes. During each decrement, the particles were collected either directly from the flow output or indirectly by a second magnetic column with a strong magnetic of 0.22 T, as shown in Figure 2.1. Afterward, the magnetic field was reduced again to give multiple fractionations.

**Characterization of SPIONs**

ZetaSizer Nano ZS90 (Malvern, UK) was used to measure particle hydrodynamic diameters (Z-average size), particle size distribution (PI), and Zeta potentials. All measurements were taken in triplicates by the sizing instrument.

Superconducting Quantum Interference Device (Quantum Design, US) was used to measure the magnetic susceptibility of SPIONs.

SpectraMax i3 (Molecular Device, US) was used to measure the optical absorbance of samples.

## Chapter 3 : A Study of the Size Dependency of Magnetic Mobility and Diffusivity of Superparamagnetic Iron Oxide Nanoparticles and an Improvement for Diffusive Magnetic Fractionation

### 3.1: Abstract

Superparamagnetic iron oxide nanoparticles (SPIONs) are crucial base material for biomedical applications, such as magnetic hyperthermia, magnetic targeting, and contrast enhancement for magnetic resonance imaging (MRI). The safety and performance of these applications are strongly dependent on the bio-distribution of SPIONs which is affected by their particle size distribution. Diffusive magnetic fractionation (DMF) was developed to improve the size homogeneity of SPIONs. The DMF method showed excellent control of particle size distribution. However, it is laborious to optimize the DMF for different SPION formulations through trial-and-error. Therefore, computational models were developed to predict the optimal condition for different particle formulations, which demonstrated strong agreement with experimental results.

## 3.2: Introduction

SPIONs are common nanocarriers for varied biomedical applications. The biomedical performance of SPIONs is connected to its mass transportation, which is influenced by the particle size and particle size distribution [11,37,89]. Many purification techniques attempt to control the particle size distributions in order to control their bio-distribution and the pharmacokinetics. Nevertheless, none of them are very effective, including vacuum filtration, gel chromatography, and magnetic fluid fractionation techniques [4–6,9,10,95–99,101]. Thus, a previously described magnetic fluid fractionation technique, diffusive magnetic fractionation (DMF), was developed and demonstrated significant improvement on controlling particle size distribution.

The DMF utilizes a pulsed magnetic field (PMF) to sized SPIONs into multiple layers based on their magnetic mobility and diffusivity. The process starts with a particle suspension being periodically attracted to a PMF source. Differently sized particles move toward to a magnetic source in various rates during magnetic pulses. This magnetic attraction rate increases with particle size. Between pulses, differently sized SPIONs diffuses freely in the absence of a magnetic field. The diffusion rates are inversely proportional to their particle sizes according to Stokes' Einstein relationship. Therefore, the particles are eventually sized into different layers after multiple pulses, which the larger sized particles are closer to the PMF source than the smaller ones. The particles can then be fractionated layer-by-layer by decreasing the applied magnetic field strength. The method showed significant improvement from conventional methods with high particle recovery and scalability.

However, it requires significant amount of time and materials when working with a new SPION formulations. A trial-and-error approach is generally used to seek for an optimal pulse sequences for particles with new formulations. Multiple pulse sequences are tested until a

reasonable performance is observed. This trial-and-error approach usually takes a long time and a lot of particles to find the optimal pulse sequences. Therefore, it is crucial to develop a systematic way to calculate the optimal pulse sequences for different SPIONs formulations.

Three parameters are affecting the performance of the DMF. The first parameter is the steps of the decreasing magnetic field after the layers are formed. The interval of the steps controls the number of particles being released, which affects the particle distribution. A smaller interval will result fractions with narrower distributions. The second parameter is the number of repeating cycles of the PMF. In general, particles are sized better into layers when the number of repeating cycles are higher. The last parameter is the pulse sequences of the PMF and it is the key to optimizes the DMF performance. The sequences determine how the magnetic particles are sized into different layers, which are later fractionated layer-by-layer to give monodisperse particles. An optimal pulse sequence can significantly improve the DMF performance and reduce the duration of the process. Computational models were developed to predict the optimal DMF settings for different magnetic particle formulations. PEGylated, aminated and starch coated SPIONs were used to represent SPIONs with different formulation and to confirm the prediction from the developed models.

**Theory and modeling for differently sized particles:**

The concept of DMF is based on the mobility differences of magnetic attraction and diffusion between differently sized SPIONs. Larger particles have a faster magnetic attraction rate and a slower diffusion rate than smaller particles. The time difference $|\Delta t_r|$ between varied sized SPIONs to be fully immobilized, indicates how particles are sized into layers. The performance of the DMF is expected to improve when $|\Delta t_r|$ increases. The $|\Delta t_r|$ between two sized particles is determined by the pulse sequence of the applied PMF. The pulse sequence can be simplified into

two parts, which are magnetic attraction and diffusion. The mass transport of SPIONs can be described by the Equation of Continuity.

$$\frac{dc}{dt} + \nabla \cdot \vec{J} = 0 \tag{1}$$

The particle concentration c is depended on time $t$ and position $x$. The total flux $\vec{J}$ contains a diffusion driven part and a force driven part, $\vec{J} = \overrightarrow{J_D} + \overrightarrow{J_F}$, which $\overrightarrow{J_F} \neq 0$ during magnetic attraction and $\overrightarrow{J_F} = 0$ during diffusion. Magnetic attraction happens during a magnetic pulse and diffusion happens between pulses. The Equation of Continuity can be rewritten as the following equation (2) with diffusivity constant D independent of concentration.

$$\frac{dc}{dt} = D\nabla^2 c - \nabla \cdot (\vec{v}c) \tag{2}$$

Except the concentration $c$, all the terms are independent of time. Therefore, the time dependent general solution for concentration $c$ can be assumed as following, which is later confirmed with experimental result.

$$c = c_0\, e^{-\beta t_m} \tag{3}$$

The constant β is proportionate to the magnetic attraction rate and it is a function of particle size $R_p$ and position x. The time variable $t_m$ is the time for magnetic attraction, which is also known as the pulse width of the PMF. To solve for β, it is assumed a position dependent solution $r_{(x)}$, which its steady stead solution is previously solved [102]. The constant β can be expressed in the form of the following.

$$\beta = -Dr''_{(x)} + \vec{v}r'_{(x)} + \overrightarrow{v'}r_{(x)} \tag{4}$$

To solve for the particle size dependency of β, the total force acting on a single SPION can be described as sum of only magnetic attraction force $F_M$ and Stokes' drag force $F_D$. All other forces are assumed to be negligible compare to the two. The force balance is shown as the following.

$$F = F_M - F_D = \nabla\left(\vec{m} \cdot \vec{B}\right) - 6\mu\eta R_p \vec{v} \tag{5}$$

$\vec{B}$ is the applied magnetic field, $\eta$ is the dynamic viscosity, $R_p$ is the radius of the SPION, and $\vec{v}$ is the particle drift velocity. Assuming uniformly magnetized spherical SPIONs, the magnetic moment $\vec{m} = \frac{4}{3}\pi R_p^3 \vec{M}$. The force balance can be rewritten as the following.

$$F = \frac{4}{3}\pi R_p^3 \nabla\left(\vec{M} \cdot \vec{B}\right) - 6\mu\eta R_p \vec{v} \tag{6}$$

The drift velocity $\vec{v}$ is assumed to only depended on position because the time to reach terminal velocity is very short, which is a result from the high surface to mass ratio of nanoparticles. Therefore, the nanoparticle velocity during a magnetic pulsed is can be calculated as followed.

$$\vec{v} = \frac{2{R_p}^2}{9\eta}\ \nabla\left(\vec{M} \cdot \vec{B}\right) \tag{6}$$

The particle drift velocity $\vec{v}$ can be substituted into Equation of Continuity (2) and can be rewritten as the following equation (7)

$$\frac{dc}{dt} = \frac{kT}{6\pi\eta R_p}\nabla^2 c - \nabla \cdot \left(\left(\frac{2{R_p}^2}{9\eta}\ \nabla(M \cdot B)\ \right)c\right) \tag{7}$$

Therefore, the particle size dependency of $\beta$ in equation (4) can be shown as following.

$$\beta = \frac{g_{(x)}}{R_p} + h_{(x)}\frac{R_c^3}{R_p} \tag{8}$$

$$\begin{cases} g_{(x)} = -\dfrac{kT}{6\pi\eta}\nabla^2 c \\ h_{(x)} = \dfrac{2}{9\eta}\left(\nabla(M\cdot B)\cdot\nabla c + c\nabla^2(M\cdot B)\right) \end{cases} \tag{9}$$

The function $g_{(x)}$ is based on diffusion and $h_{(x)}$ is the result of magnetic attraction. The equation was used to model the change in SPION concentration of differently sized particles during magnetic attraction.

Between the pulses of an applied PMF, SPIONs are diffusing freely away from the magnetic source. Based on the Stoke-Einstein relationship, larger SPIONs have a slower diffusion rate than smaller SPIONs. The mass transport of the diffusion can be described as

$$\frac{\partial C}{\partial t} = D\frac{\partial^2 C}{\partial x^2} \tag{10}$$

The time dependent general solution for a fixed position can be described as

$$c = c_0\left(1 - e^{-\frac{\alpha\, t_d}{R_p}}\right) \tag{11}$$

where α is a positive constant which is in proportionality to diffusivity coefficient $D$ and $t_d$ is the time between pulses. Equations (3) and (11) are used to model the change in concentration of differently sized SPIONs with a given pulse sequence. The given pulse sequence consists of $t_m$, $t_d$, the strength of the magnetic pulse, and n which is the number of repeating cycles.

The time to fully captured differently sized SPIONs, $T_c(x, R_p)$, were estimated by calculating the time to reach 95% capture. For a fixed position, the remaining time, $T_r$, to reach 95% capture can be calculated for differently sized particles based on their current concentration.

$$T_r(c, R_P) = T_c\left(R_p\right) - T\left(c, R_p\right) \tag{12}$$

The $|\Delta T_r|$ between differently sized SPIONs equals to the additional time required for the smaller SPIONs to reach 95% capture, which is used to determines the performance of the DMF. A larger $|\Delta T_r|$ indicates a larger time difference between the larger particle and the smaller to reach 95% capture, which improves how SPIONs are sized into layers.

3.3: Result and discussion

The particle mobility during magnetic attraction and diffusion is measured by capturing and releasing SPIONs with a bar magnet, as shown in Figure 3.1. Different sized SPIONs were captured by a bar magnet and their change in concentrations were observed overtime, shown as Figure 3.2 (A). Different sized SPIONs demonstrated significant different magnetic attraction rate. The SPIONs can be fitted perfectly with a single exponential (SE) model except for the original, the largest, and the smallest SPIONs as shown in Figure 3.2 (B). The original SPIONs showed distinguishable difference between its SE fit and multiple exponential (ME) fit. It also showed a significantly larger uncertainty range compared to the fractionated SPIONs. Similarly, the largest and the smallest fractionation, are expected to have broader particle size distributions since particles above or below a certain size will all be collected by these two fractionations. The smallest SPIONs, however, can be fitted perfectly by a model with a SE term with a constant term, which indicates it exist 20% of a certain particle size that is simply too small to be captured by the magnetic field. Similar analysis can be applied to particles with different surface treatments, as shown in Figure 3.3 and Figure 3.4. Therefore, equation (3) can be used model the magnetic attraction profile for differently sized monodisperse SPIONs with vary formulations and the β value can be extracted accordingly. The size dependency of β, equation (8), can be simplified for a fix position and showed as following, where A and B are fitting parameters.

$$\beta = \frac{A}{R_p} - B\ R_p^2 \tag{13}$$

The experimental result showed strong agreement with the model, as shown in Figure 3.5. The model is used to predict the particle attraction rate with differently sized SPIONs, as shown in Figure 3.6.

On the other hand, diffusion of different sized particles can be acquired simply by removing the bar magnetic after the magnetic attraction, as shown in Figure 3.7. Different size particles clearly showed very different diffusion rates. The diffusion behavior can be modeled by equation (11) for different SPIONs formulation, but the measurement is only accurate when the rate is slow. Therefore, for aminated SPIONs and starch coated SPIONs only the largest sized fraction is used to calculated the overall diffusivity by Stokes' Einstein relationship, as shown in Figure 3.8 and Figure 3.9. Combine with the result from magnetic attraction, a complete concentration model during magnetic attraction and diffusion can be modeled.

During magnetic attraction, the concentration decreased due to the capture of SPIONs. On the other hand, SPIONs concentration increased during diffusion due to the absent of a magnetic field. The change of SPION concentration in suspension with an applied PMF sequence can be calculated. Different pulse sequence can be applied, as shown in Figure 3.10. Therefore, $|\Delta T_r|$ can be calculated for any given particle size and pulse sequence. For example, for aminated SPIONs between 70~140 nm the $|\Delta T_r|$ can be calculated, which the optimal setting has the highest value of $|\Delta T_r|$ with a pulse sequence of 88 seconds pulse width and 25 seconds between pulses, as shown in Figure 3.11.

## 3.4: Conclusion

The mathematical models showed strong agreement with the experimental results, which confirmed that our model can be used to predict the optimal pulse sequence for different SPION formulations. The models were based on magnetic attraction and diffusion data, which can be easily acquired with the described experimental setup. The magnetic attraction and diffusion data demonstrated strong agreement with the theoretical fits, which was used to calculated the magnetic attraction and diffusion kinetics of differently sized particles. $|\Delta T_r|$ values are calculated for different pulse sequences, which is used to indicate the performance of the DMF. The DMF performance improves with the calculated value $|\Delta T_r|$ increases. Therefore, the models can be used to calculated the optimal pulse sequences based on simple magnetic attraction and diffusion data.

**Surface modification of SPIONs.** Starch Coated, aminated and PEGylated SPIONs were used in this study. Starch coated SPIONs were purchased from Chemicell, Berlin, Germany. Aminated SPIONs were obtained from the starch coated SPIONs through surface modification [103]. First, 2 mL the starch coated SPION were first crosslinked with epichlorohydrin (Alfa Aesar) after incubated in 6M NaOH (BDH chemicals) for 15 minutes. The product was purified with dialyzed (8-10 kDa MW, Float-A-Lyzer®; Spectrum Laboratories, CA) and incubated with 2mL of 30% ammonia for 24 hrs at room temperature. PEGylated SPIONs were obtained from the aminated SPIONs through surface modification. mPEG-NHS (Nanocs, MA) PEGs were used to surface modify the aminated SPIONs. 15 mg of mPEG-NHS was dissolved in 300 uL DMSO. A mixture of 300 uL of water and phosphate buffer was added into the PEG in DMSO solution. PEGylated SPIONs can be acquired after Aminated SPIONs was added into the mixture and shaken for 24 hours.

**Diffusive magnetic fractionation.** Aqueous SPION suspension was injected into a magnetic column (LS Column; Miltenyi Biotec) with the bottom of the column sealed with parafilm. The column was place inside a 22W electric coil powered by a DC power supply (Hewlett Packard 6543A). The output current of the power supply was controlled to turn on and off periodically. In general, the time duration for the on and off cycle was 30 seconds on and 10 seconds off unless stated otherwise. The current was increased in after each cycle and the settings are 5, 10, 30, 50, 100, 200, 450 mA unless stated otherwise. The magnetic field was maintained constant at 450 mA for 10 minutes once the pulse magnetic field sequence was completed. The parafilm on the column was removed and a second column was connected to the system. A water flow was then introduced by a peristaltic pump (FH100; Thermo Scientific) with a flow rate of 1.5ml/min. The system was left to stabilized for 5 minutes. Then, a bar magnetic with 0.22 T magnetic field is place on the

second magnet and the magnetic field strength was decreased stepwise to release particles with different size. The release SPIONs will be captured by the second column.

**Particle size and size distribution measurement.** The Particle size and size distribution was measured by dynamic light scatter measurement (ZS90; Malvern, UK).

**Magnetic attraction study.** A bar magnetic with 0.25 T magnetic field strength was place inside a 96-well plate with its magnetic pole pointing an adjacent well. SPION aqueous suspension was added into the adjacent well next to the 0.25T bar magnet. Absorbance at 450 nm was measured (SpectraMax i3;Molecular Device, US) at the center of the well with SPION suspension. Measurements were taken every 10 minutes for 6 hours.

**Free diffusion Study**. The study was performed after the magnetic attraction study. The 0.25 T bar magnetic was removed from the 96-well plate. Absorbance measurement was taken at the center of the well every 10 seconds for minutes or at multiple positions inside the well every minute for 20 minutes.

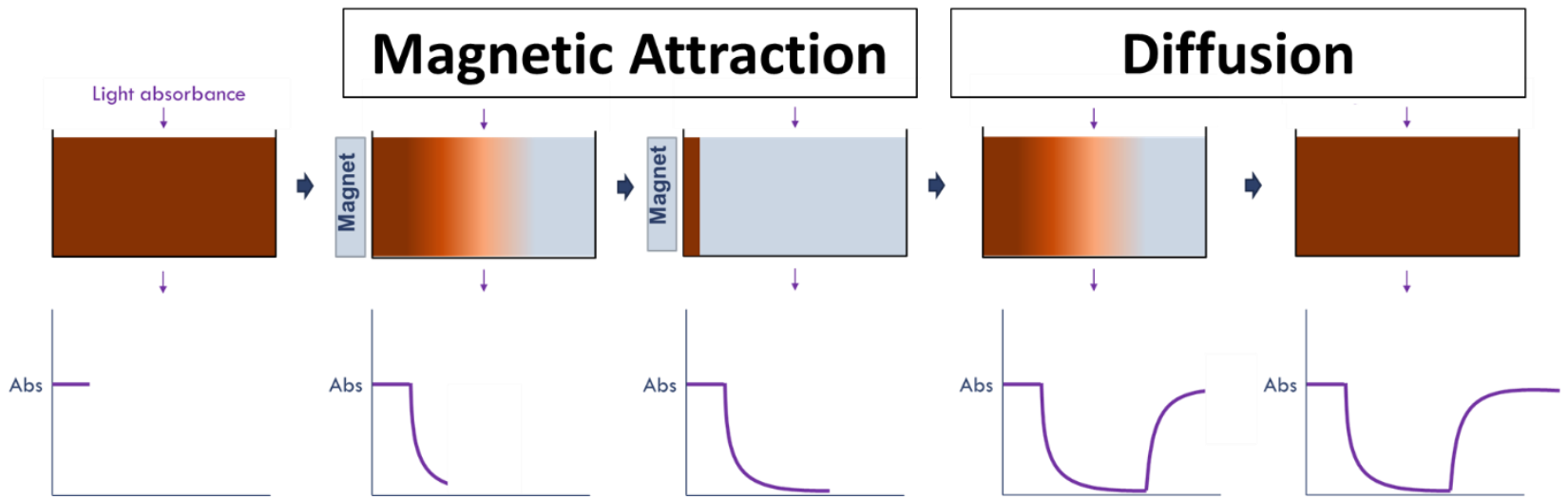




Figure 3.1. The experiment setup to measure the particle mobility of SPIONs during magnetic attraction and diffusion. The change of SPIONs concentration is observed by measuring the absorbance across a static fluid suspension. The concentration slowly reduced during magnetic attraction and slowly increase during diffusion.

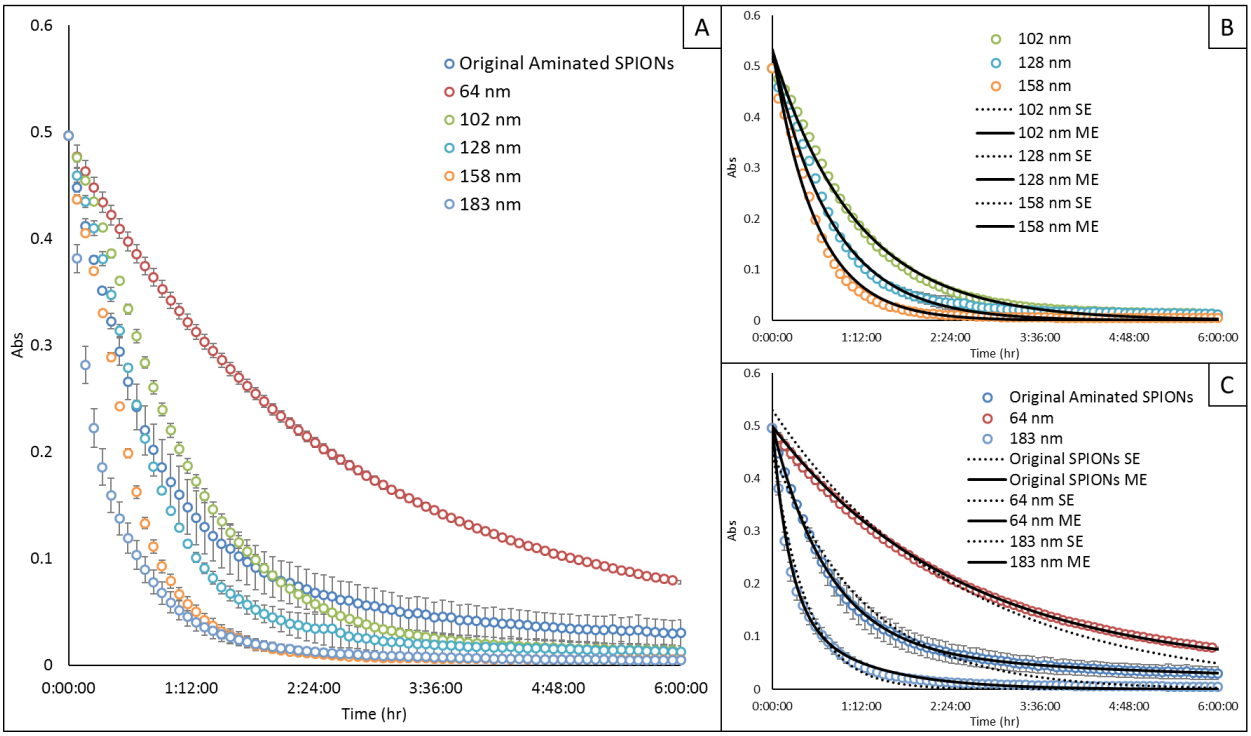


Figure 3.2. Absorbance measurements of the change in aminated SPION concentration with constant magnetic gradient. Original aminated SPIONs has an average size of 137 nm and a PI of 0.18. The original particle was split into multiple fractions with DMF. The fractionated particles have average sizes of 64, 102, 128, 158, and 183 nm and the PIs are 0.09, 0.06, 0.08, 0.08, 0.08, and 0.1. All experimental results were fitted by single exponential models (SE) and some were fitting by exponential models with multiple terms (ME).

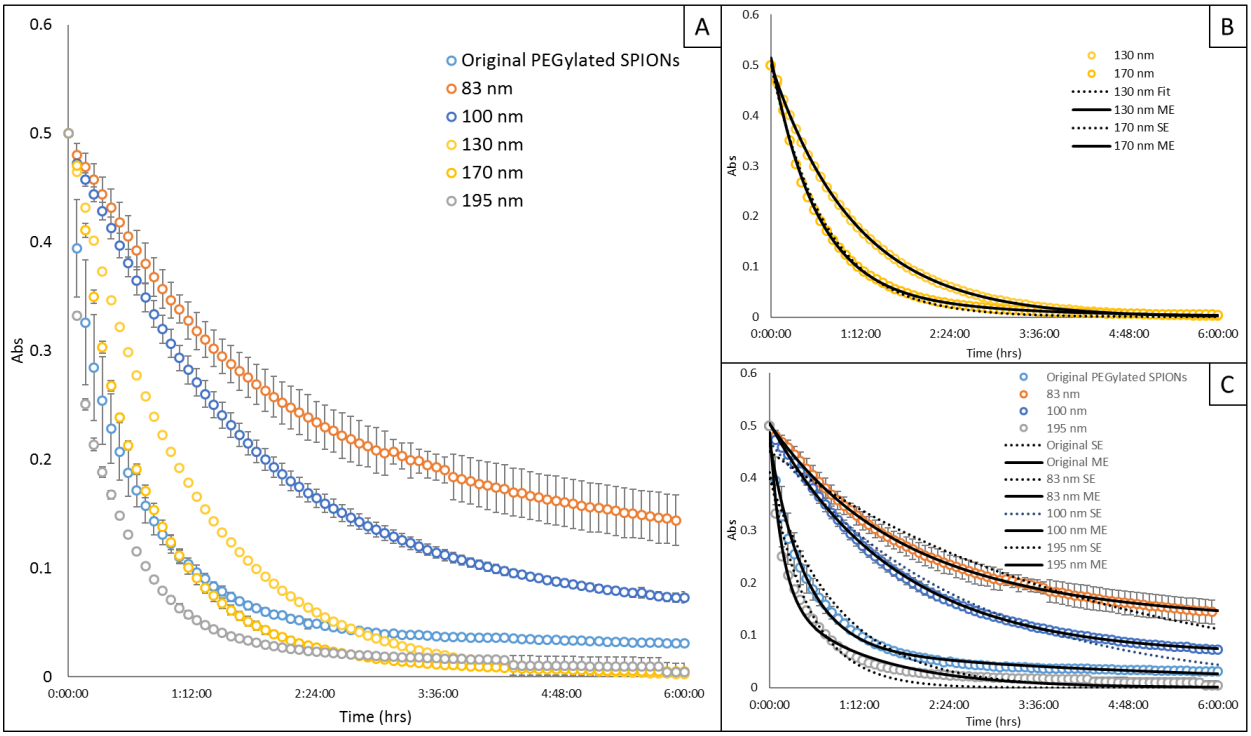


Figure 3.3. Absorbance measurements of the change in PEGYlated SPIONs concentration with constant magnetic gradient.

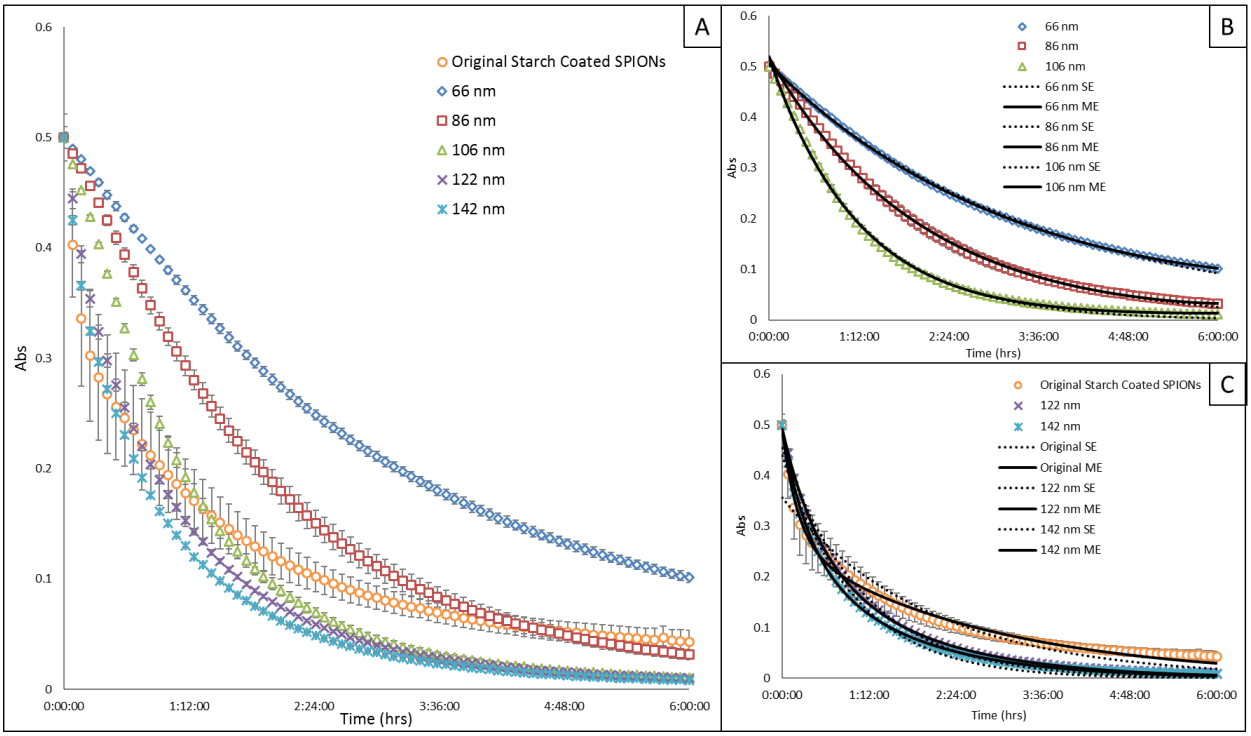


Figure 3.4. Absorbance measurements of the change in starch coated SPIONs concentration with constant magnetic gradient.

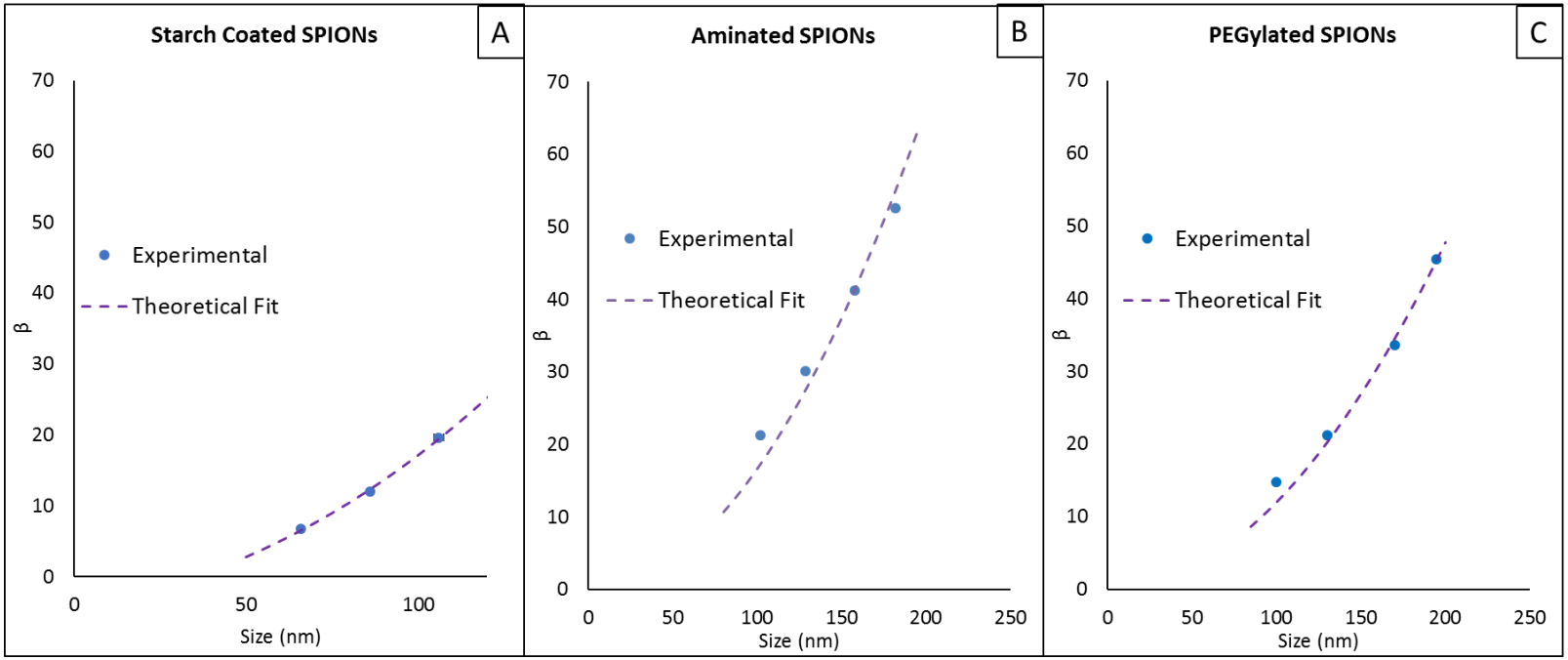


Figure 3.5. Comparison of the magnetic attraction rate constant β between experimental data and theoretical fit from equation (11). Data from magnetic attraction experiment with (A) aminated SPIONs, (B) PEGylated SPIONs, and (C) Starch Coated SPIONs.

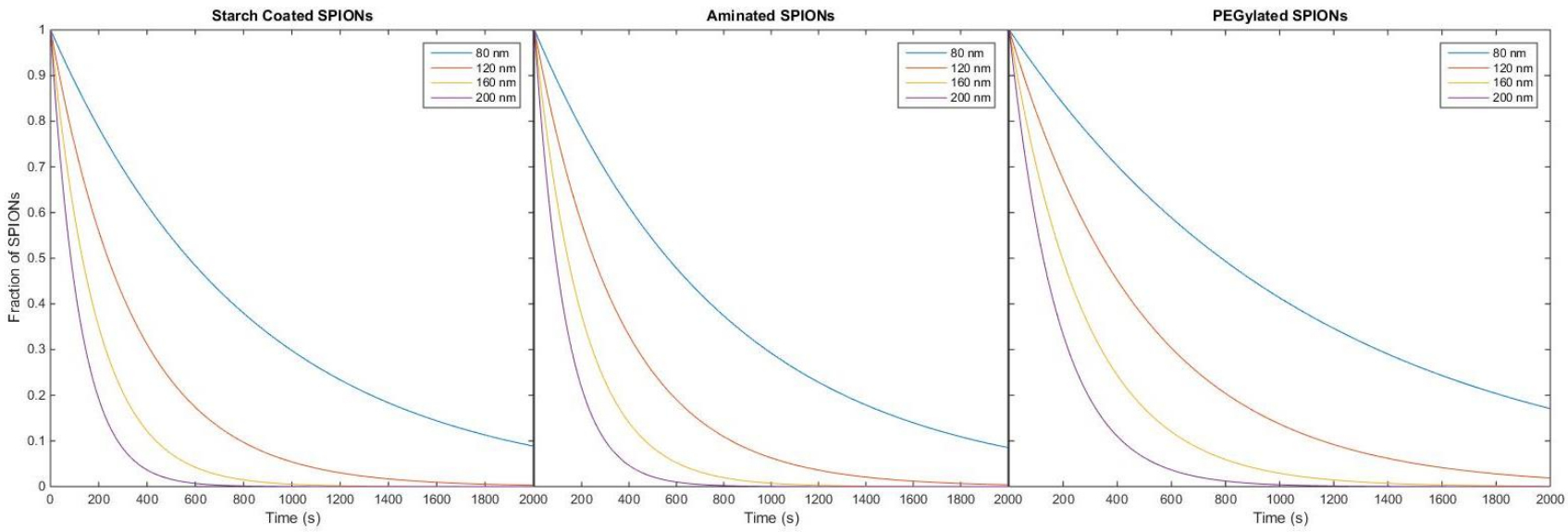


Figure 3.6. SE models for magnetic attraction of different sized SPIONs with different formulations.

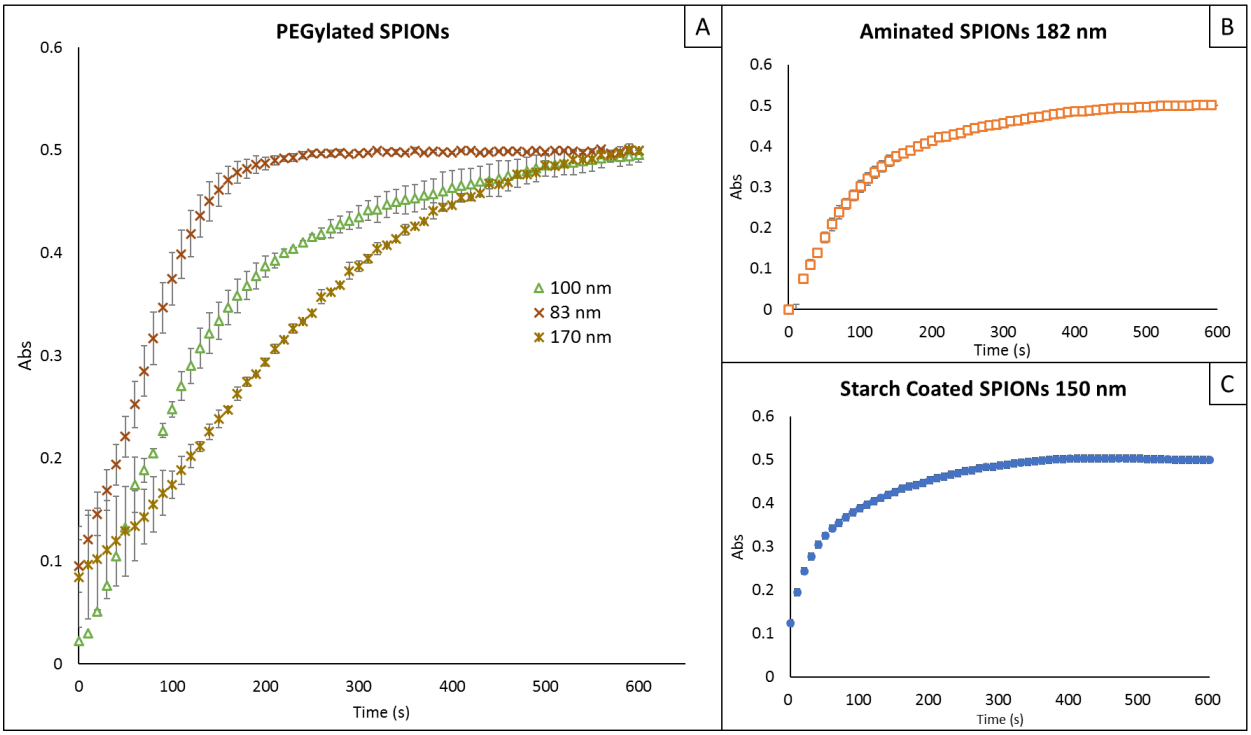


Figure 3.7. Diffusion of different sized PEGylated SPIONs with (A) PEGylated SPIONs, (B) aminated SPIONs, and starch coated SPIONs.

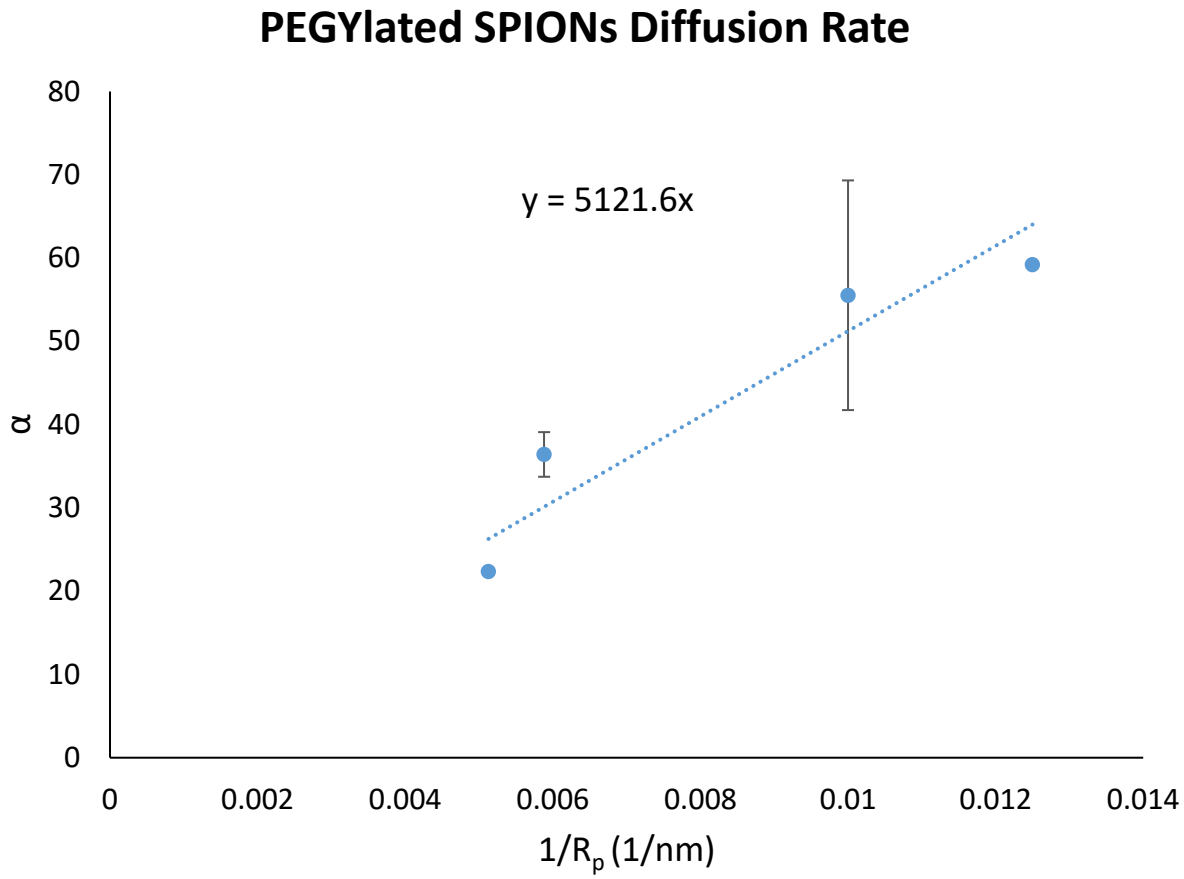


Figure 3.8. The size dependency of SPION diffusion rate α. It demonstrated a good agreement with Stokes' Einstein relationship.

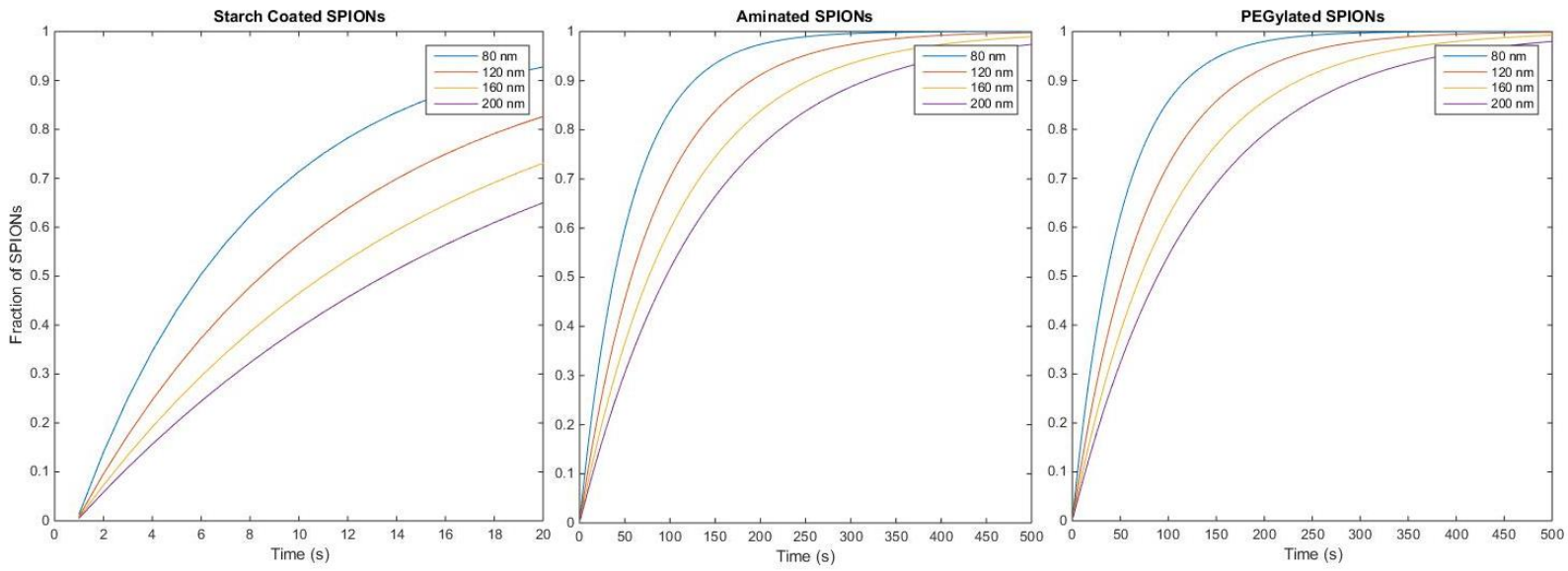


Figure 3.9. Computational modeled diffusion profile for different sized SPIONs.

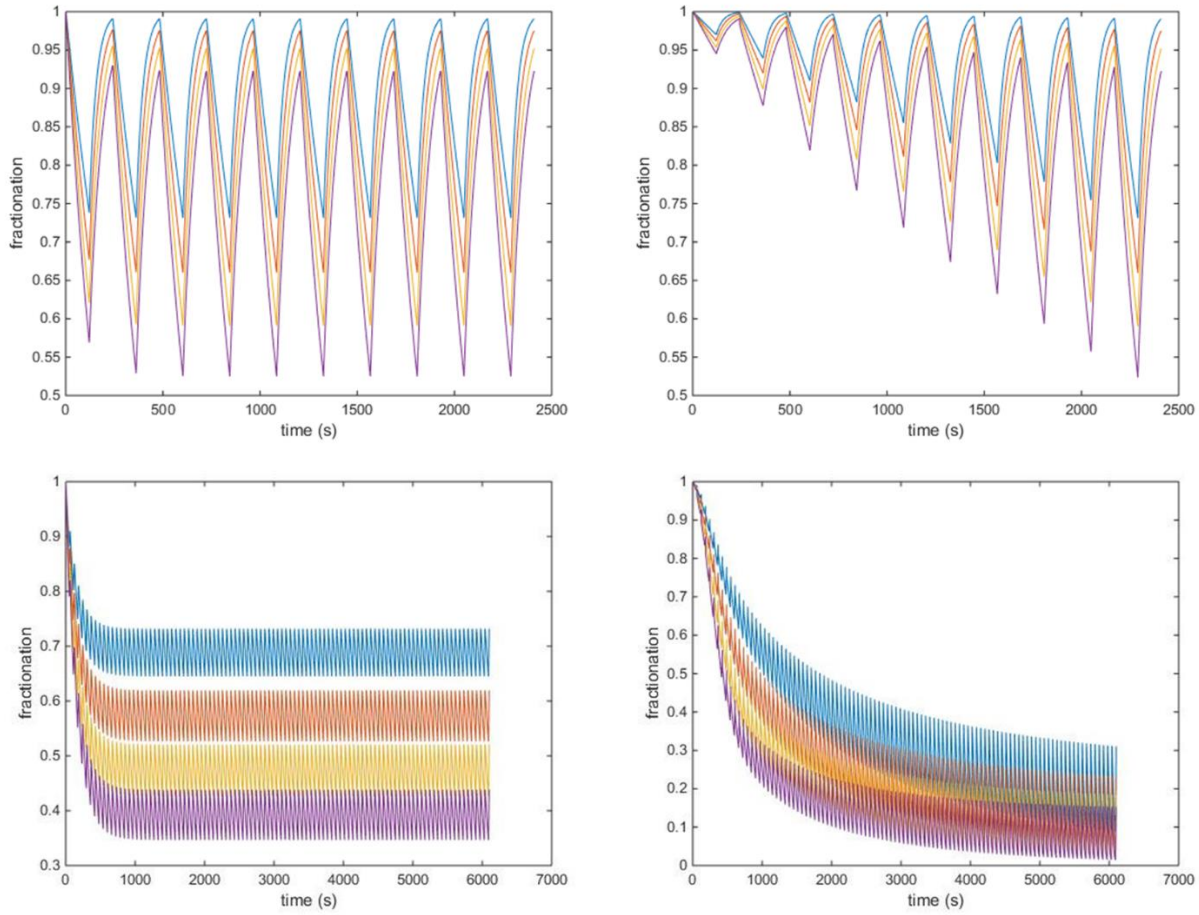


Figure 3.10. SPION concentration during PMF magnetic field. (A) The change in SPION concentration with a constant magnetic field with 10 cycles. (B) The change in SPION concentration with an increasing magnetic field strength with 10 cycles. (C) The change in SPION concentration with a constant magnetic field with 100 cycles. (D) The change in SPION concentration with an increasing magnetic field strength with 100 cycles.

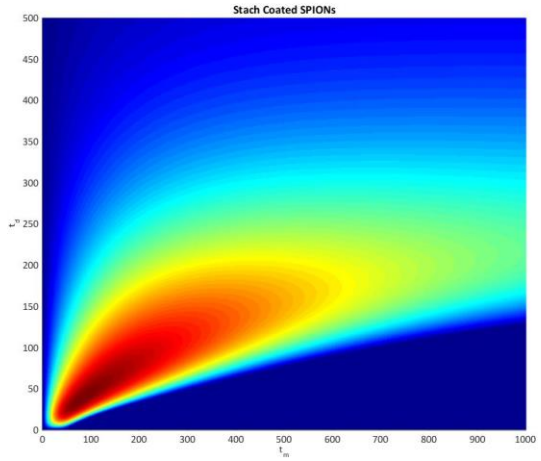
Stach Coated SPIONs
$t_d$
$t_m$

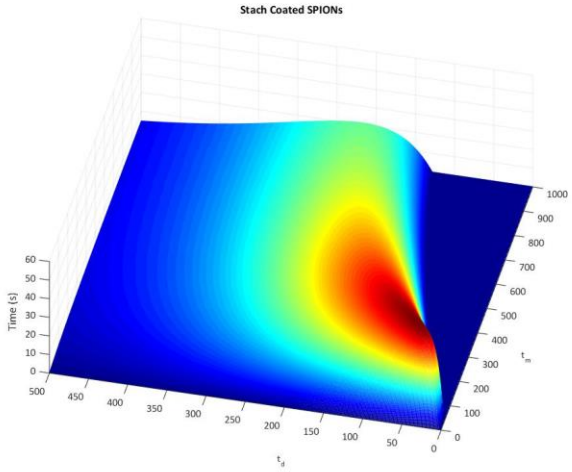
Stach Coated SPIONs
Time (s)
$t_d$
$t_m$

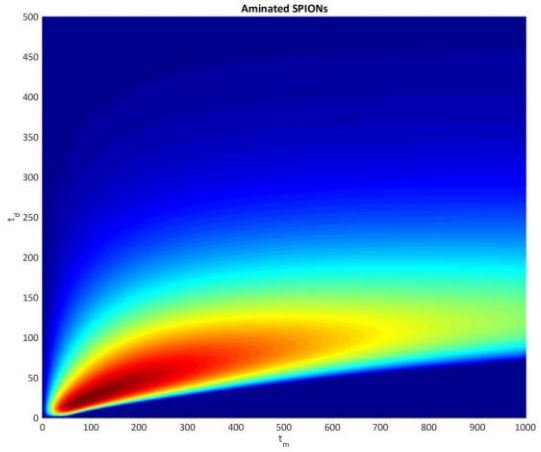
Aminated SPIONs
$t_d$
$t_m$

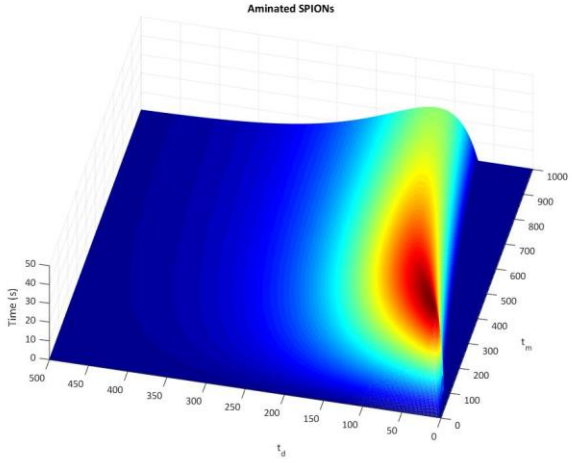
Aminated SPIONs
Time (s)
$t_d$
$t_m$

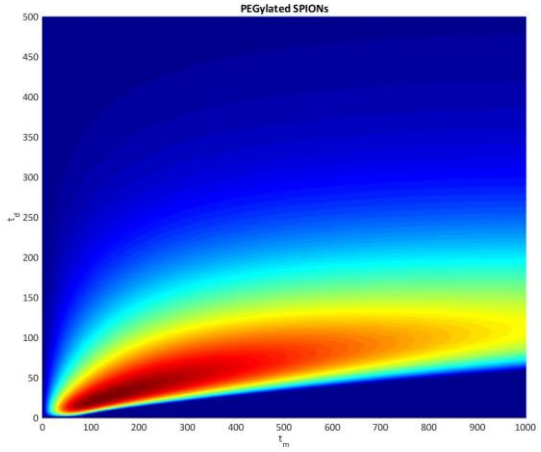
PEGylated SPIONs
$t_d$
$t_m$

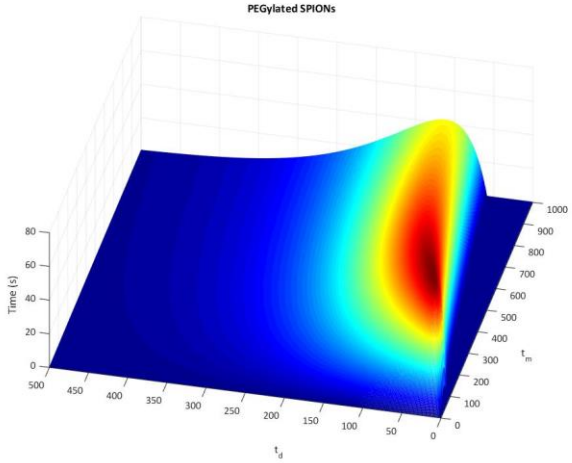
PEGylated SPIONs
Time (s)
$t_d$
$t_m$

Figure 3.11. $|\Delta T_r|$ is calculated with a constant strength PMF for SPIONs between particle size of 70 to 140 nanometers. The optimal pulse sequence for starch coated SPIONs has a $t_m$= 70 and $t_d$ = 35, as shown in part (A). The optimal pulse sequence for aminated SPIONs is $t_m$= 80 and $t_d$ = 20, as shown in part (B). The optimal pulse sequence for starch coated SPIONs is $t_m$= 110 and $t_d$ = 20, as shown in part (C).

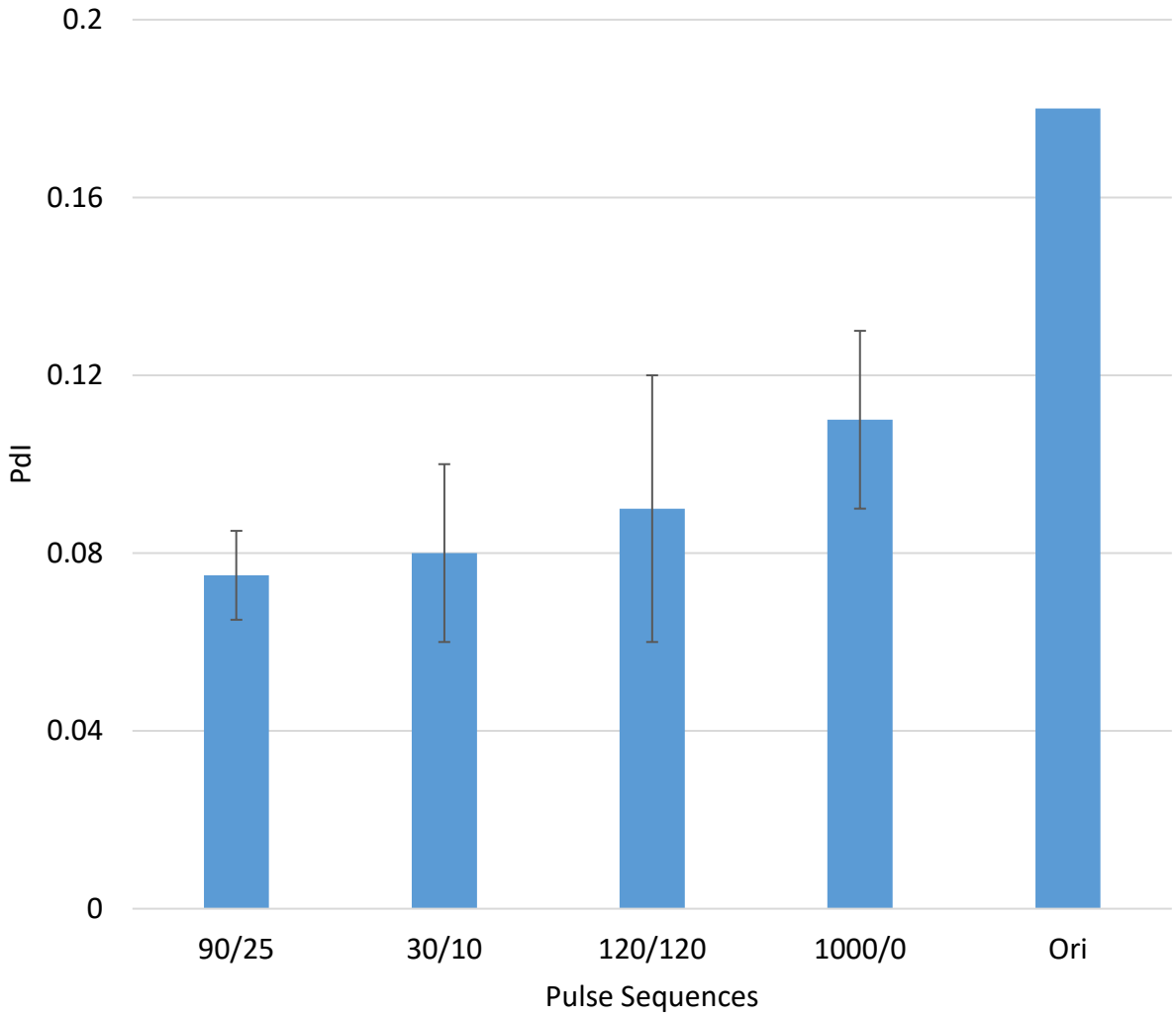


Figure 3.12. The optimal settings showed significant difference from other settings. There is significant difference between 30/10 and 1000/0 with P = 0.03 (n=63).

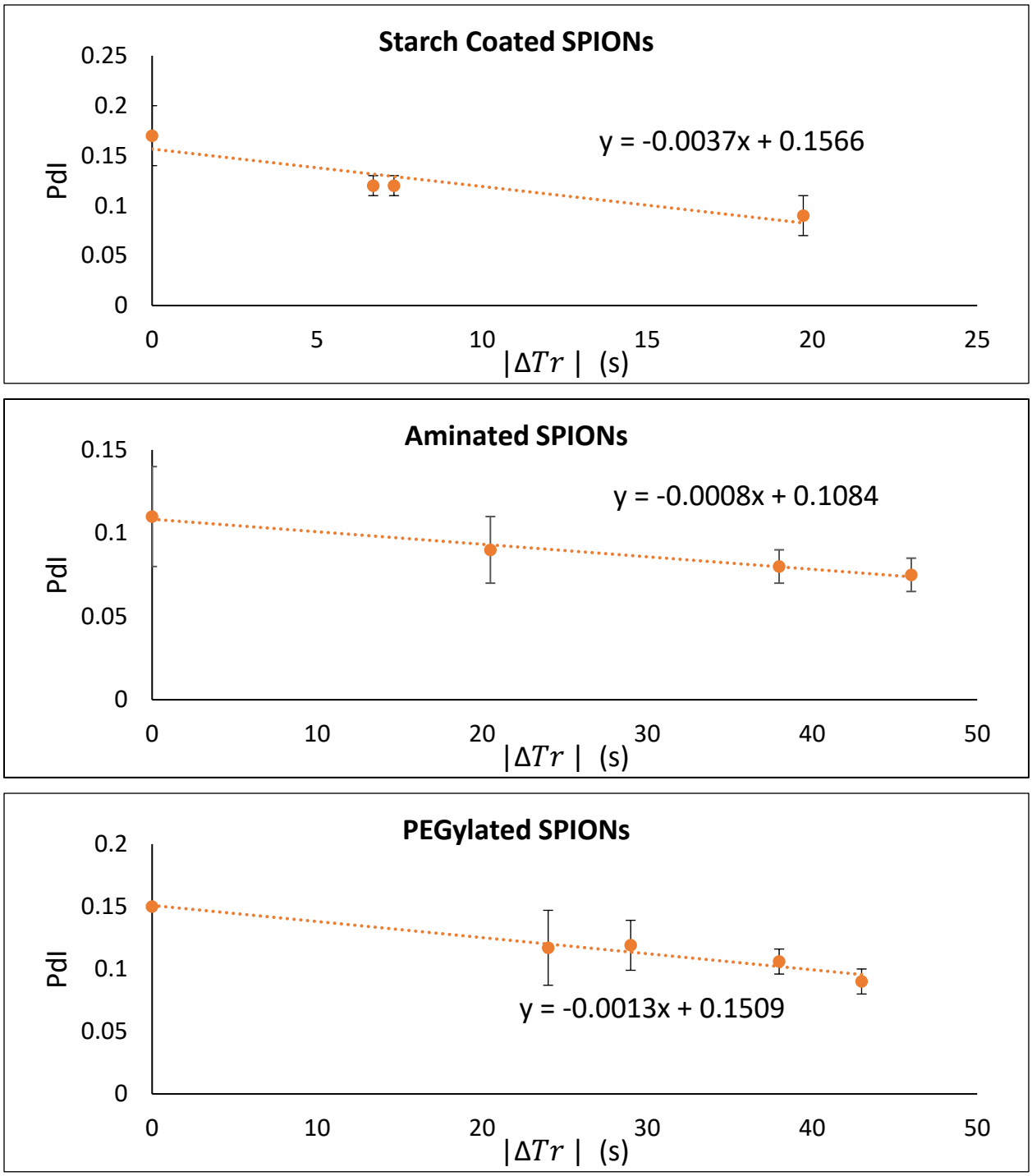


Figure 3.13. The DMF performance showed strong agreement with the models for all SPION formulations.

## Chapter 4 : Application for Monodisperse SPIONs: Enhanced Penetration of SPIONs through a Biological Barrier

### 4.1: Abstract

Most iron oxide based biomedical applications involve a delivery concept, including drug targeting, magnetic resonance imaging (MRI), and magnetic hyperthermia treatment. The efficacy of particle transport has a direct impact on drug dosage, imaging quality, and heat distribution. Therefore, controlling and improving the transportation of particles is extremely important for biomedical applications. The mass transportation of SPIONs is affected by multiple parameters, including different biological environments, particle sizes, and the conditions of the applied magnetic field. Therefore, a cell monolayer with controlled confluency, sized SPIONs, and a rotational magnetic field is used to study their effect on the mass transportation. The rotational magnetic showed significant improvement of the mass transport compared to static and no magnetic field. The mass transport rate is controllable with different frequency of the magnetic field. Furthermore, differently sized SPIONs showed twice the mass transport rate with only 50 nm difference in particle size.

### 4.2: Introduction

Super paramagnetic iron oxide nanoparticles (SPIONs) are unique for their low toxicity and magnetic characteristic. The magnetic property can be leveraged to control the particle transportation and overcome biological barriers through a magnetic field [87,104,105]. An improved SPION transportation mechanism can dramatically improve the performance of current SPION applications, including drug delivery [103,104], target specific MRI contrast enhancement [87], and magnetic hyperthermia [74], in terms of dosage [106,107], imaging quality [108], and heating distribution [74]. The key to improve SPION transportation is to maximize SPION mobility while minimize SPION aggregation [73]. The SPION transportation rate through a biological barrier is affected by

multiple parameters, such as pore size of the barrier, particle size [37–39], surface chemistry, particle concentration and applied magnetic field [73,109]. There are many studies trying to promote SPION transportation efficiency through different magnetic field settings, including pulsed, constant, and rotational magnetic field [73,109,110]. Constant magnetic field could promote SPION transportation only at low concentration situation due to less particle aggregations [73,109,110]. Pulsed magnetic field showed enhanced SPION penetration through a cell monolayer at high concentration because SPIONs can redisperse between pulses [73]. Rotational magnetic field also enhanced SPION mobility through a physical barrier because SPIONs are forced to spin and move with the field and slowing down the rate of aggregation [109].

Here, we study the effect of cell confluency, particle size, and different frequencies of a rotational magnetic field on the mass transport of SPION across a human intestinal epithelial cell (Caco-2) cell monolayer. The Cell confluency is determined by a combination of Transepithelial Electrical Resistance (TEER) and optical microscope image analysis. TEER showed good reliability when confluency is greater than 50%. On the other hand, optical microscope image analysis has a better performance when the cell confluency is below 50% compared to TEER. Different sized particles were obtained by diffusive magnetic fractionation technique and each fraction has a narrow size distribution. The particle size and distribution were measured by dynamic light scattering. A rotational magnetic field was generated by a rotating bar magnet with a constant gradient. Caco-2 cells were cultured at different confluency in Transwell inserts with 1μm porous bottom. SPION suspension was prepared in cell culture media and added into the upper compartment of the Transwell insert. The inserts were placed into a 24-well plate and placed on top of a rotating magnet, as shown in Figure 4.1. Finally, SPION transport kinetics was studied with constant, rotational, no magnetic field for their initial mass transport rate and overall transported mass in 2 hours.

4.2: Result and discuss:

**Enhanced SPION transportation with 200 rpm rotational, constant, and no magnetic field across a cellular monolayer with controlled confluency.** The 200 rpm rotational magnetic field showed significant improvement of particle transportation compared to constant and no magnetic field. The confluency of the Caco-2 cell monolayer was measured by a combination of TEER and optical microscope image analysis. Microscope image of the entire well was taken and calculated for their cell population.

When Caco-2 cells were cultured for more than 8 days, the cellular structure became very tight and SPIONs did not seem to have the mobility to move through the Caco-2 monolayer regardless of magnetic field conditions, as shown in Figure 4.2(A).

Small amount of SPIONs traveled through the Caco-2 monolayer with the rotational magnetic field when the culture aging was reduced to 6 days. On the other hand, both constant and no magnetic field scenarios showed no sign of SPION transportation across the cellular barrier, as shown in Figure 4.2(B).

When the cell culture aging was reduced to 5 days, SPION transportation was observed for all three field conditions. For both the initial and 2 hours mass transport results, the rotational magnetic field showed about twice the mass transport rate than static or no magnetic field scenarios, as shown in Figure 4.2(C) and Figure 3.

When the cell culture aging was reduced to 4 days, there was significant change in confluency observed by microscope images with 70% the calculated confluency. The rotational magnetic field transported 75% of the total SPIONs across the cellular barrier within 2 hours and had an initial mass transport rate of 0.72 ng/s. With the same condition, either constant or magnetic field showed significantly lower initial and overall mass transport rate, as shown in Figure 4.2(D) and Figure 4.3.

When the cell culture aging was reduced to 3 days, the confluency was 30%. The rotational magnetic field showed 90% overall mass transportation in 2 hours and an initial mass transport rate of 1.05 ng/s, which was significantly higher than either constant or no magnetic field scenarios. Static magnetic field transported significantly more SPIONs in 2 hours than no magnetic field; even they have the same initial mass transport rate, as shown in Figure 4.2(E) and Figure 4.3. Since their initial mass transport rates were the same for both constant and no magnetic field, it is reasonable to assume both conditions having the same mass transport driving force across the cellular barrier at the beginning of the process. The only driving force for no magnetic field is gravity and diffusion. Assuming gravity being neglectable in this particle size range, concentration difference is the major driving force for diffusion. For no magnetic field case, the SPION concentration at the lower compartment is slowly building up over time and weakening the driving force. For constant magnetic field, SPIONs moved across the cellular barrier the 1 μm membrane and aggregate at the bottom of the lower compartment due to the constant magnetic field gradient. This left the top of the fluid in the lower compartment in very low SPION concentration and kept the driving force remain strong.

SPION transport kinetics was studied without the Caco-2 cell monolayer but only a 1μm PET membrane. It showed that 90% of SPIONs moved across the membrane by the rotational magnetic field within 2 hours, which is still significantly better than the constant and no magnetic field. There was no statistical difference in both initial and overall mass transport rate between constant and no magnetic field, as shown in Figure 4.1.

The rotational magnetic field showed a significant improvement in both initial and overall mass transport rate of SPIONs compared to the constant and no magnetic field. Other the other hand, constant and no magnetic field showed identical initial mass transport rate for all measurements. It implies that the transportation is majorly driven by concentration gradient.

**Effect of SPION transportation across a Caco-2 monolayer with rotational magnetic field of different frequencies.** Constant magnetic field (0 rpm), 100 rpm, 200 rpm, 300 rpm, 400 rpm, 800 rpm and no magnetic field were used to study the mass transport of SPIONs. Caco-2 cells were cultured for 4 days with a TEER value of 250 $\Omega/cm^2$ and confluency of 70%, as shown in condition (D) in Figure 4.2. The total SPION transportation was high in transportation rate, no significant dependency of frequency in the range of 100~400 rpm and all 4 tested frequencies showed initial mass transport rates about 0.8 ng/s and 80% transportated in 2 hours, as shown in Figure 3. However, when the rotational frequency reached 800 rpm, the initial mass transport rate was significantly reduced from 0.8 ng/s to 0.5 ng/s and the mass transport is significant lower in the first 60 minutes, as shown in Figure 4.3 and Figure 4.4. Therefore, there is an optimal frequency to give the maximum SPION transport within the first 60 minutes. All 5 rotational magnetic field conditions showed indistinguishable 2 hour SPION transport results. For SPION in broad size distribution, about 20% of SPIONs simply cannot or travel too slow to across the Caco-2 monolayer even with 70% confluency. We also see this in the previous section that the mass transport only reaches 90% in 2 hours even without the Caco-2 cell monolayer as shown in Figure 4.2. Therefore, we prepared different sized SPIONs for further investigation.

**A comparison of different sized SPIONs moving across a Caco-2 monolayer with rotational and no magnetic field.** PEGylated SPIONs particles have a Z-average size of 135 nm and an average polydispersity index of 0.16. The particles were spitted into fractionations by diffusive magnetic fractionation with average sizes of 117 nm, 135nm, and 170 nm and an average polydispersity index is 0.09 for all three of them. The mass fractions of the original size distribution were also calculated to be 0.4, 0.4, and 0.2 respectively. The SPION transportation across a Caco-2 cell monolayer was observed by the influence of 200 rpm rotational and no magnetic field. Caco-2 cells were cultured for 5 days and reached a TEER of 500 Ω/cm2 and confluency of 100%, which

is the same as condition (C) in Figure 4.2. In 2 hours, the rotational magnetic field showed great improvement on original 117 nm while 135 nm and 170 nm showed very limited improvement, as shown in Figure 4.5. The initial mass transport rates are about 2 times of the rates of original SPIONs, 117nm, and 135 nm compared to 170 nm with the rotational field, as shown in Figure 4.6 and Figure 4.7. If we sum up all the 2-hour transported mass of the three sized fractions by their corresponding mass ratio toward the original particle, we get an overall mass transport of 28% in 2 hours. The result is very close to the measured overall mass transport of the original SPION of 29%. It implies that the mass transport of SPION is greatly influenced by particle sizes under the applied condition of rotational field and confluency. On the other hand, the results of 2 hours transported mass are almost identical regardless of particle sizes when no magnetic field was applied. It implies that the particle size effect is weak without applied magnetic field and confluency.

**SPION transportation switches from a constant magnetic field to a rotational magnetic field.** Since the mass transport of SPION is very sensitive to the condition of the applied magnetic field, the behavior of SPIONs was manipulated by the field condition. The condition of the Caco-2 monolayer is 400 $\Omega/cm^2$ with 80 confluency. SPIONs were exposed to a constant magnetic field for 60 minutes followed by 60 minutes of rotational magnetic field. The corresponding results are compared to those of SPION transportation under 120 minutes of constant magnetic field. Particles had undergone a behavior change when the magnetic field parameters were changed, as shown in Figure 4.8. Therefore, the mass transport of SPION can be controlled by switching between different applied magnetic field conditions, such as no magnetic field, constant, pulse and rotational magnetic field.

## 4.3: Conclusion:

The one-dimensional transport of SPIONs through a cellular layer is greatly influenced by the confluency, particle sizes, and field conditions. The study demonstrated the effect of each component toward the transport of SPION in terms of initial mass transport rate and total mass transport rate in 2 hours. The mass transport of SPION is a balance between the applied magnetics force and the induced particle aggregation. The magnetic force enhanced the SPION's mobility across the cellular barrier. However, the applied magnetic field introduces SPION aggregations. Therefore, we observed a rotational magnetic field can promote SPION transport with different confluency because it slows down the particle aggregation rate. We also observed low particle transport rate when the rotational frequency is too low (0 rpm) or too high (800 rpm). Particle size also showed a significant effect, smaller size SPIONs have a higher mass transport rate in compared to larger SPIONs. Ultimately, our result showed a possible path toward controlling of SPION transportation to overcome biological barriers with different parameters.

4.4: Figures

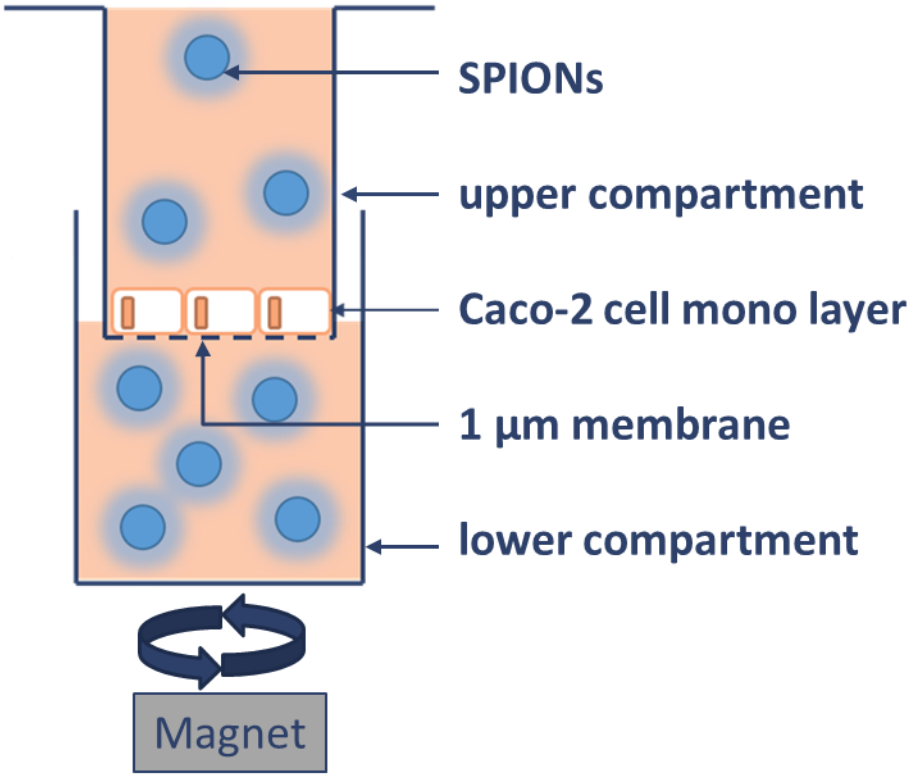


Figure 4.1. Transwell setup to study mass transport of SPION across a cellular barrier.

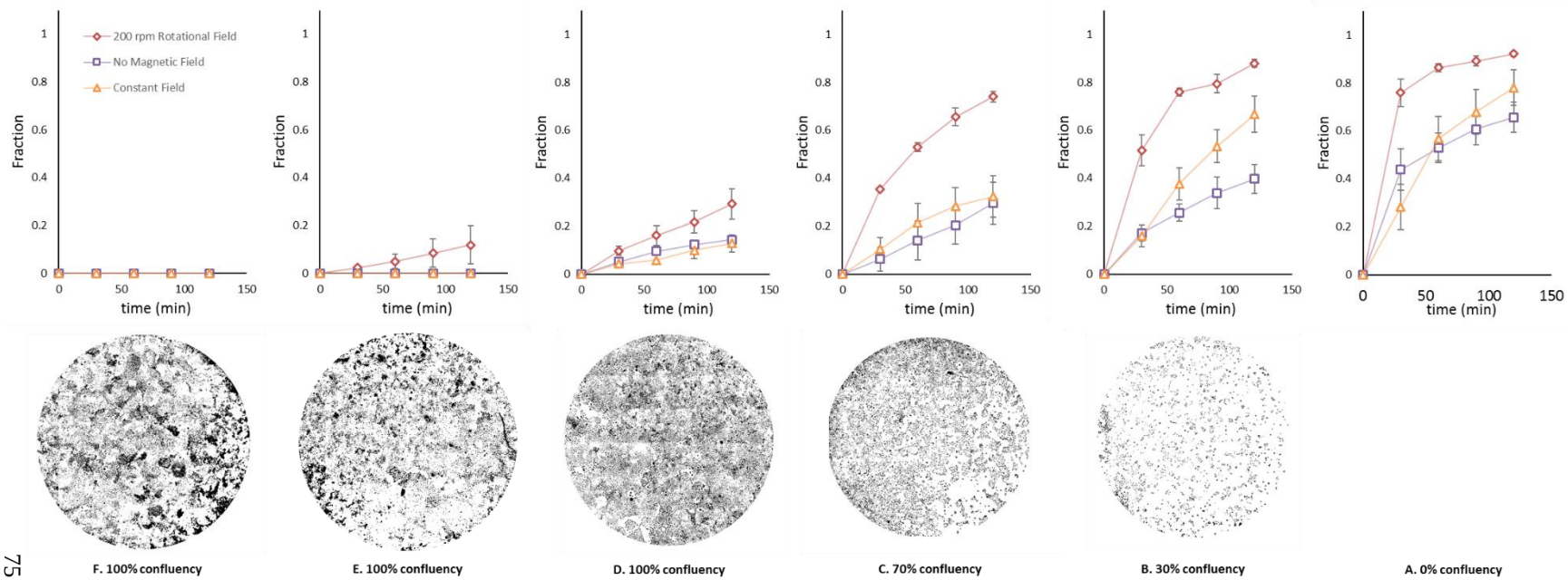


Figure 4.2. SPION transportation through Caco-2 cell monolayers with different confluency (N=3). (A) Caco-2 cells were cultured for 8 days. The TEER value is 1500 Ω/cm$^2$ and the estimated confluency is 100 %. All three methods show no sign of SPION transportation. (B) Caco-2 were cultured for 6 days and only 200 rpm rotational field showed SPION transportation in a small amount. The TEER value is 900 Ω/cm$^2$ and the estimated confluency is 100%. (C) Caco-2 cells were cultured for 5 days with a TEER value of 500 Ω/cm2 and an estimated confluency of 100%. The 200 rpm rotational field transported 30% of inputted SPIONs while constant and no magnetic field only transported 15%. (D) Caco-2 cells were cultured for 4 days with a TEER value of 250 Ω/cm2 and an estimated confluency of 70%. The 200 rpm field transported 75% of SPIONs in two hours while constant and no magnetic field can only achieve 30%. (E) Caco-2 cells were cultured for 4 days with a TEER value of 220 Ω/cm2 and an estimated confluency of 30%. The 200 rpm rotational field transported 90% of the SPIONs while constant magnetic field had 65% and no magnetic field had 40%. (F) The transportation of SPIONs was observe with only the 1µm PET membrane without the cell monolayer. The 200 rpm rotational field showed 90% particle penetration through the membrane while constant magnetic field had 80% and no magnetic field had 65%.

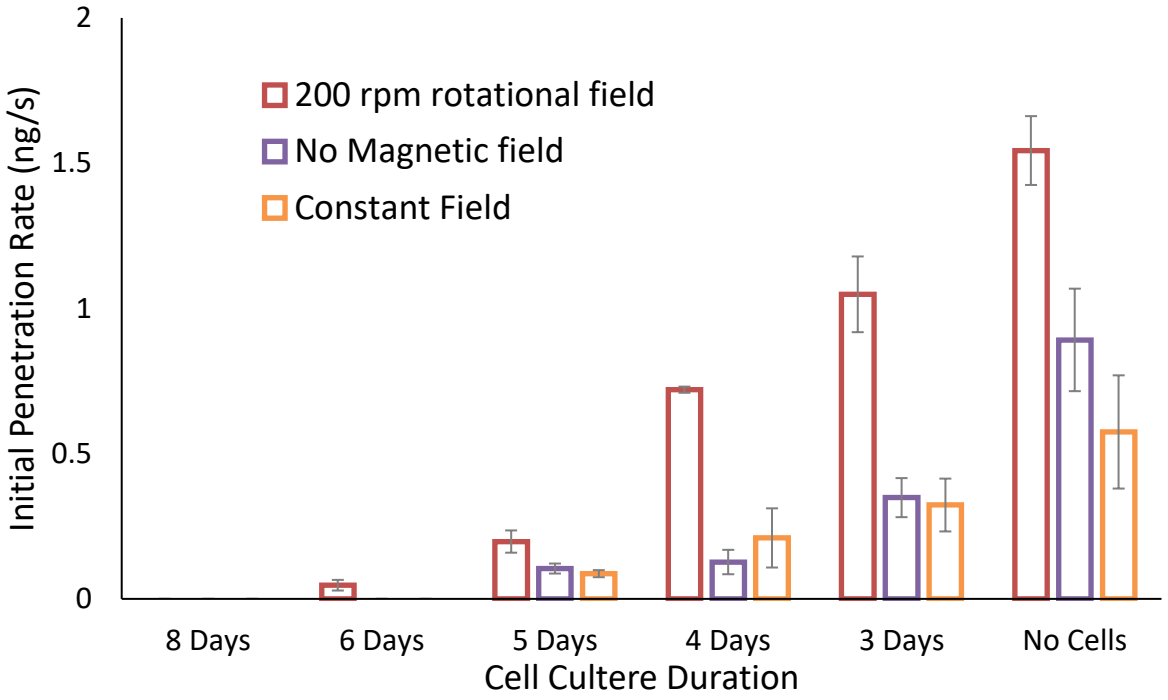


Figure 4.3. Initial mass transport rate of SPIONs across Caco-2 cell monolayers with different cell confluency (N=3). The initial mass transport rate is calculated by the mass of SPION penetrated through the cell monolayer in the first 30 minutes. The 200 rpm rotational magnetic field showed significant difference from constant and no magnetic field. The constant and no magnetic field showed no statistical difference except when there are no Caco-2 cells. One-way ANOVA test and Tukey's test were used ($\alpha$=0.05) to determine significant difference between the means. Constant and no magnetic field showed no statistical difference in initial mass transport rate.

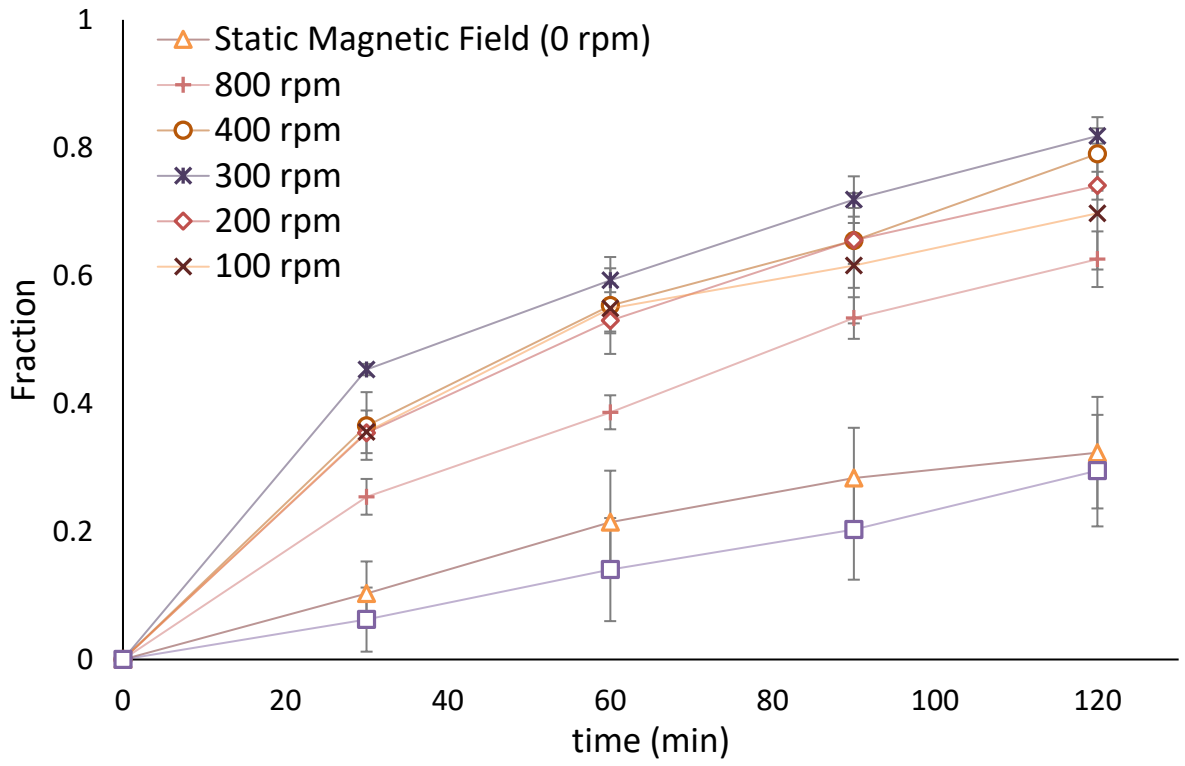


Figure 4.4. SPION overall transportation with rotational magnetic field of different frequency and with 4 days of cell culture (N=3).

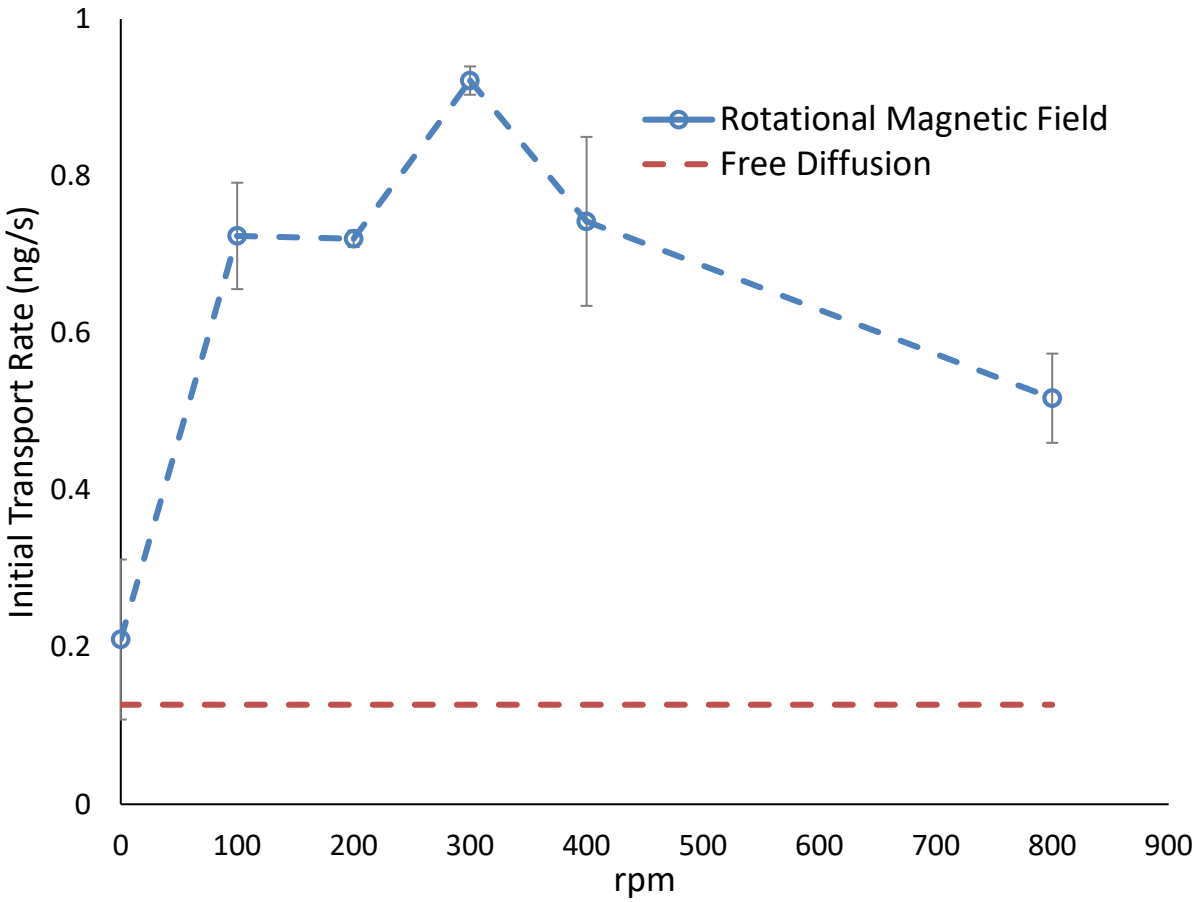


Figure 4.5. SPIONs initial mass transport rate with magnetic fields of different rotational speed (N=3). The initial mass transport rate was estimated by the mass transport in the first 30 minutes. One-way ANOVA test and Tukey's test were used ($\alpha$=0.05) to determine significant difference between the means. Constant and no magnetic field showed no statistical difference in initial mass transport rate.

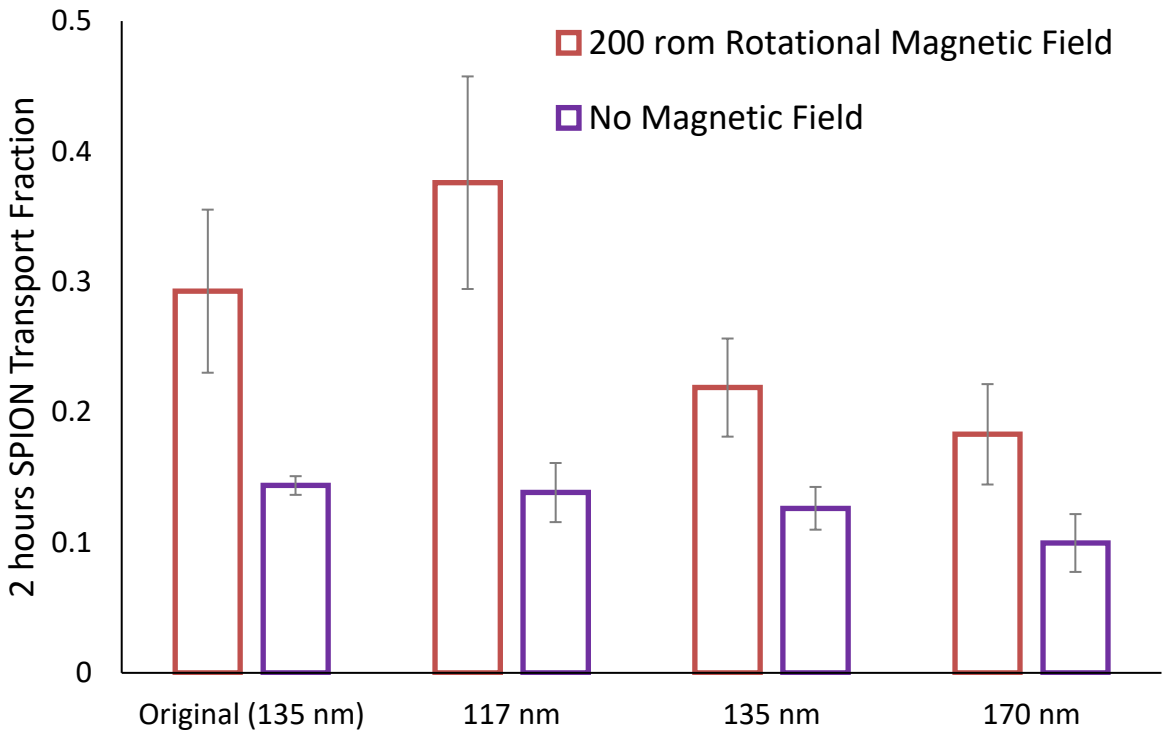


Figure 4.6. The 2 hours SPION mass transportation with sized selected particles (N=3). The original PEGylated SPIONs has a Z-average size of 135 nm and a polydispersity index of 0.16. The sized SPIONs were fractionated from the original PEGylated SPIONs with average polydispersity index of 0.09 and with Z-average sizes of 117 nm, 135 nm, 170 nm. Different sized SPIONs showed no significant difference with no magnetic field. However, Original and 117 nm showed significant improvement in SPION transport with 200 rpm rotational field ($P<0.05$) while 135 nm and 170 nm only showed small improvement from no magnetic field .

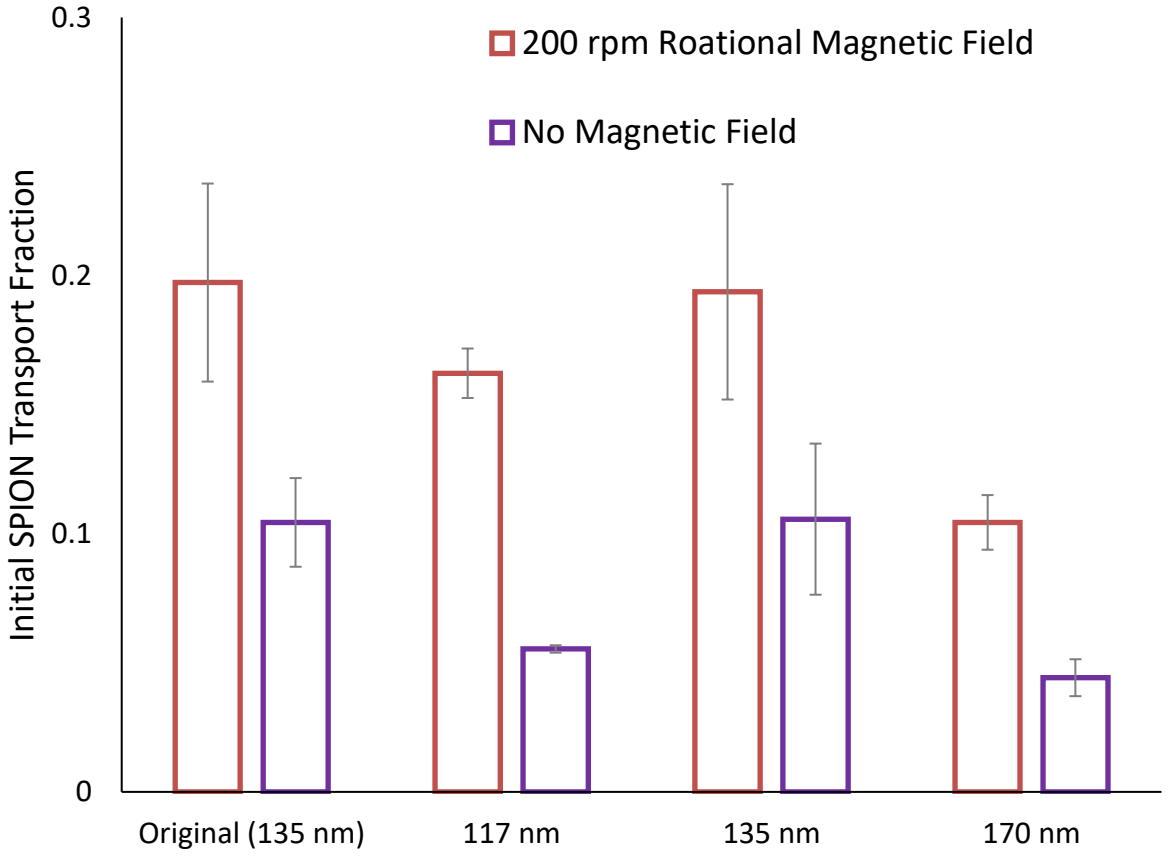


Figure 4.7. The initial SPION transport rate within 30 minutes (N=3). The original PEGylated SPIONs has a Z-average size of 135 nm and a polydispersity index of 0.16. The sized SPIONs were fractionated from the original PEGylated SPIONs with average polydispersity index of 0.09 and with Z-average sizes of 117 nm, 135 nm, 170 nm. There was no significant difference in SPION transport with no magnetic field, but significant improvement of mass transport with 200 rpm rotational magnetic field.

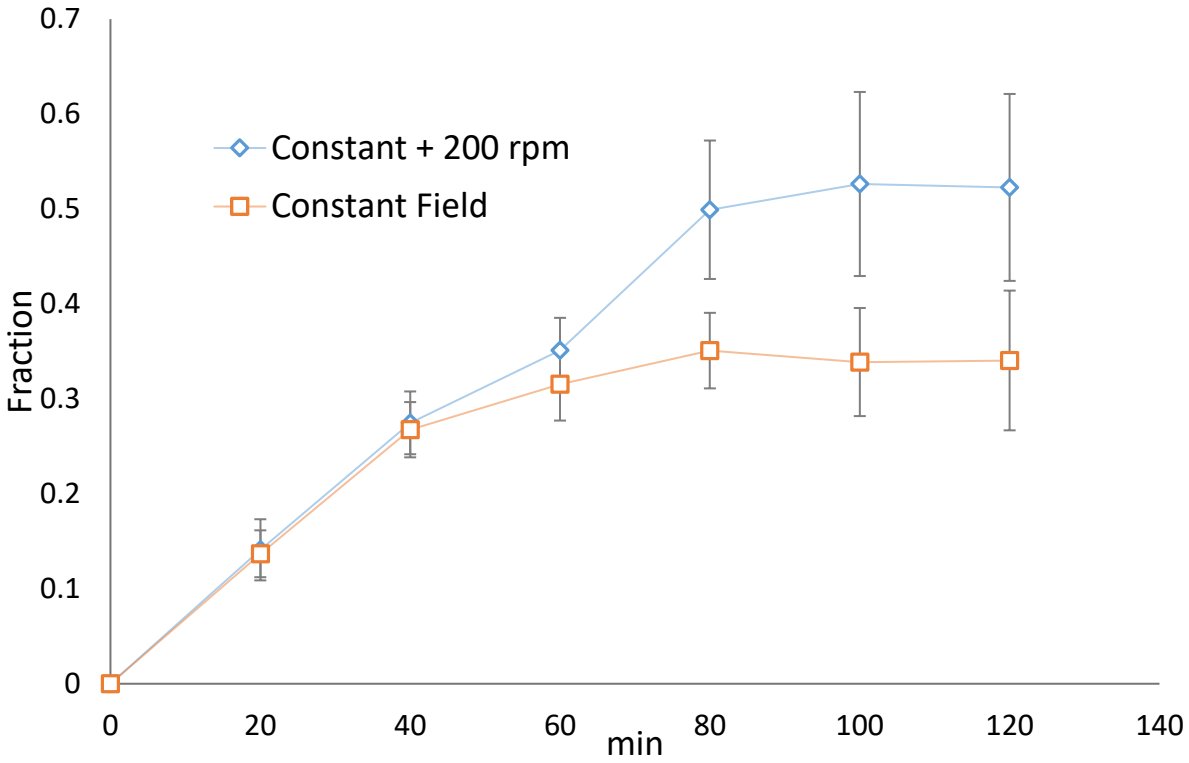


Figure 4.8. Plot shows a direct comparison between Constant and rotational magnetic field. SPION transport across Caco-2 cell monolayer with TEER of 400 Ω/cm2 and estimated confluency of 90%. Blue indicates SPION transport with 60 minutes of constant magnetic field in the beginning followed by 60 minutes of 200 rpm rotational magnetic field. Orange is the mass transport with a constant magnetic field for 60 minutes.

4.5: Materials and Methods

**PEGylated SPIONs Preparation.** The commercially purchased starch coated SPIONs were cross-linked, aminated, and PEGylated according to previously published method. The method starts with 2 mL of starch coated SPIONs solution (22 mg/ml) incubated with 2.6 mL 6M NaOH for 15 minutes. Then, 1.3 mL of epichlorohydrin was added and the resulting solution was incubated for 24 hrs at room temperature. The solution was then dialyzed against water with an 8-10 kDa MWCO Float-A-Lyzer® G2 dialysis device (Spectrum Laboratories, Inc., Rancho Dominguez, CA). The purified SPION solution was then incubated with 2 ml of 30% ammonia for 24 hrs at room temperature to provide aminated SPIONs. The PEGylated SPION was obtained from mPEG-NHS. Firstly, 15mg of 5 MW of mPEG-NHS was dissolved in a mixture of 300 µl DMSO, 300 µl water, and 300 µl phosphate buffer. Then, a 300 µl of aminated SPION solution was added to the mixture and was shaken for 24 hrs at room temperature. The resulting mixture solution was then magnetically separated from the solution and washed with DI-water for 4 times.

**Size selected SPIONs.** SPIONs with specific size range were produced from previously disclosed method diffusive magnetic fractionation (DMF) technique. Magnetic columns (LS Column; Miltenyi Biotec) were filled by PEGylated SPIONs. Then a pulsed magnetic field was applied by a 22W electric coil. The current of the coil is control by a DC power supply (6543A; Hewlett Packard). The pulsed magnetic field went on for 30 seconds and off for 10 seconds periodically with a total of 8 cycles. The current strength was increased on each cycle which the settings are 5, 10, 30, 50, 100, 200, 300, and 450 mA. The current is maintained at 450 for 10 minutes and a fluid flow was introduced into the system for another 5 minutes. Then, the current was decrease stepwise to collect different sized SPIONs.

**Particle Size Measurement.** ZetaSizer Nano ZS90 (Malvern, UK) was used to measure particle hydrodynamic diameters, and particle size distribution.

**Cell Culture.** CaCO-2 cells (obtained from American Type Culture Collection (ATCC) and were culture in 25 $cm^2$ flasks at 37 °C with 5% $CO_2$ humidified incubator. The cells were cultured with media consisting of 79% Eagle's minimum essential medium (MEM; Corning Co., NY), 20% fetal bovine serum (FBS; Seracare Life Science), and 1% penicillin-streptomycin (Gibco 10378). The CaCO-2 cells were detached from their container with trypsin (TripLE; Gibco) passaged with 1:6-1:8 ratio when reaching 70% confluency.

The cell monolayer is prepared by adding cells in suspension (500 µL, $1 \times 10^5$ cells/$cm^3$) into the upper compartment of cell culture inserts (Transwell; 353104, Corning Co., NY). The bottom of the inserts is made of PET membranes with 1µm pores. The inserts were placed inside a 24-well plate with 700 µL of MEM in the lower compartment. The plate is incubated at 37 °C with 5% $CO_2$ to 3-10 days.

**Transepithelial Electrical Resistance (TEER) Measurement of Confluency.** Epithelial Volt/Ohm (TEER) Meter ($EVOM^2$; WPI, FL) is used to measure cell confluency of CaCO-2 monolayer on the PET membrane. The measurements have a range of 90-1000 Ω/ $cm^2$.

**Optical Microscope Image Analysis of Confluency.** Optical microscope images (EVOS FL auto imaging system; Thermo Fisher Scientific Inc.) were used to estimate cell confluency of CaCO-2 monolayer on the PET membrane. Cell nucleuses are dyed with two drops of NucBlue™ (R37605, Life Technologies Co.) directly added onto the upper compartment of the inserts. The inbuilt scanning function of EVOS software (DAPI, 10X) is used to obtain images of the cell monolayer. Image J is used to calculate the number of cells from the obtained image.

**Experiment Setup.** The cell culture media on the upper compartment of the cell culture inserts were replaced by 300 µL of SPION suspension which is 0.012 µg/µL of PEGylated SPIONs in cell culture media suspension. The insert is placed into a new 24-well plated with 1000 µL of cell culture media on the lower compartment of the inserts. The plate was place on top of a

rotational/fixed magnetic field to observe SPION penetration through the cellular monolayer and membrane. The rotational magnetic field is generated by a 0.22T and 5 cm tall bar magnet rotating of top of a magnetic hotplate stirrer (97042-598; VWR). The bottom of the bar magnet was maintained 2 cm away from the center surface of the stirrer plate. The prepared 24-well plate was place on top of a foam platform that is 7 cm tall. Every 30 minutes, 200 µL of samples were collected from the lower compartment of the inserts and 200 µL of fresh cell culture media were added back into the well. During the sample collection, the inserts were completely removed from the magnetic field for 20-30 seconds. The collected samples were placed inside a 96-well plate and measure their absorbance (SpectraMax i3; Molecular Device, US) to determine their SPION concentration.

**Measurement of SPION concentration.** SPION concentration were determined by absorbance at 450 nm with 200 µL of volume. Standard curves were obtained by known SPION concentration measured by Ferrozine assay.

## Chapter 5 : Conclusion

SPIONs are one of the most powerful nanoparticle because it has both magnetic property and biocompatibility. In comparison with other nanomaterials, multiple SPION based particles were FDA approved for different usages, such as AMI-225, Feridex or Resovist. However, the undesired size effects and inconsistent performances limit the adoption of this technology. Broad size distribution of SPIONs is the root cause for major concerns. Therefore, many researchers turned away and looked for other nanomaterials with controllable size distribution, such as gold and silica nanoparticles. However, none of the material can provide the same advantages of SPIONs. That is why we focus on developing a solution, DMF method, to narrow down the size distribution of SPIONs. The DMF showed to be an efficient, controllable and scalable size separation method.

We studied the magnetic mobility and diffusivity of difference sized SPIONs. The results were used to optimize DMF to produce SPIONs with narrow distribution. We developed models based on SPION's mobility under an applied PMF and predicted the optimal pulse sequence to sized SPIONs into multiple layers. The model showed strong correlation with the performance of the DMF, which was indicated by the polydispersity index of the separated particles.

**References:**


1. Hori, M. *et al.* Detection of Hypervascular Hepatocellular Carcinoma : Comparison of SPIO-enhanced MRI With Dynamic Helical CT. **26,** 701–710 (2002).
2. Bluemke, D. A. *et al.* Hepatic MR Imaging with Ferumoxides: Multicenter Study of Safety and Effectiveness of Direct Injection Protocol. *Radiology* **228,** 457–464 (2003).
3. Duda, S. H. *et al.* Superparamagnetic iron oxide: detection of focal liver lesions at high-field-strength MR imaging. *J. Magn. Reson. Imaging* **4,** 309–14
4. Kang, J. *et al.* Size-regulated group separation of CoFe2O4 nanoparticles using centrifuge and their magnetic resonance contrast properties. *Nanoscale Res. Lett.* **8,** 376 (2013).
5. Briley-Saebo, K. C., Mani, V., Hyafil, F., Cornily, J. C. & Fayad, Z. A. Fractionated Feridex and positive contrast: In vivo MR imaging of atherosclerosis. *Magn. Reson. Med.* **59,** 721–730 (2008).
6. Arami, H., Khandhar, A., Liggitt, D. & Krishnan, K. M. In vivo delivery, pharmacokinetics, biodistribution and toxicity of iron oxide nanoparticles. *Chem. Soc. Rev.* **42,** 4906 (2015).
7. Weissleder, R. *et al.* Ultrasmall superparamagnetic iron oxide: characterization of a new class of contrast agents for MR imaging. *Radiology* **175,** 489–93 (1990).
8. Rheinlander, T., Kotitz, R., Weitschies, W. & Semmler, W. Magnetic fractionation of magnetic fluids. *J. Magn. Magn. Mater.* **219,** 219–228 (2000).
9. Rheinlander, T.; Kotitz, R.; Weitschies, W. . S. Different methods for the fractionation of magnetic fluids. *Colloid Polym. Sci.* **278,** 259–263 (2000).
10. Hasegawa, K. & Sato, T. Particle-size distribution of CoFe2O4 formed by the coprecipitation method. *J. Appl. Phys.* **38,** 4707–4713 (1967).
11. Sonavane, G., Tomoda, K. & Makino, K. Biodistribution of colloidal gold nanoparticles after intravenous administration: Effect of particle size. *Colloids Surfaces B Biointerfaces* **66,** 274–280 (2008).
12. Huang, J. *et al.* Effects of Nanoparticle Size on Cellular Uptake and Liver MRI with PVP-Coated Iron Oxide Nanoparticles. *ACS Nano* **4,** 7151–7160 (2010).
13. Gittleman, J. I., Abeles, B. & Bozowski, S. Superparamagnetism and relaxation effects in granular Ni-SiO2 and Ni-Al2O3 films. *Phys. Rev. B* **9,** 3891–3897 (1974).
14. Dunlop, D. J. Superparamagnetic and single-domain threshold sizes in magnetite. *J. Geophys. Res.* **79,** 5537 (1974).

15. Butler, R. F. Theoretical Single-Domain Grain Size Range in Magnetite and Titanomagnetite. *J. Geophys. Res.* **80,** (1975).
16. Si, S. *et al.* Size-Controlled Synthesis of Magnetite Nanoparticles in the Presence of Polyelectrolytes.pdf. 3489–3496 (2004).
17. Cole, A. J., Yang, V. C. & David, A. E. Cancer theranostics: the rise of targeted magnetic nanoparticles. *Trends Biotechnol.* **29,** 323–32 (2011).
18. Gupta, a & Gupta, M. Synthesis and surface engineering of iron oxide nanoparticles for biomedical applications. *Biomaterials* **26,** 3995–4021 (2005).
19. Park, J. *et al.* One-nanometer-scale size-controlled synthesis of monodisperse magnetic iron oxide nanoparticles. *Angew. Chemie - Int. Ed.* **44,** 2872–2877 (2005).
20. Liang, X. *et al.* Synthesis of nearly monodisperse iron oxide and oxyhydroxide nanocrystals. *Adv. Funct. Mater.* **16,** 1805–1813 (2006).
21. Yu, W. W., Falkner, J. C., Yavuz, C. T. & Colvin, V. L. Synthesis of monodisperse iron oxide nanocrystals by thermal decomposition of iron carboxylate salts. *Chem. Commun. (Camb).* 2306–2307 (2004). doi:10.1039/b409601k
22. Zhu, Y., Jiang, F. Y., Chen, K., Kang, F. & Tang, Z. K. Size-controlled synthesis of monodisperse superparamagnetic iron oxide nanoparticles. *J. Alloys Compd.* **509,** 8549–8553 (2011).
23. Cavelius, C., Moh, K. & Mathur, S. Chemically designed growth of monodisperse iron oxide nanocrystals. *Cryst. Growth Des.* **12,** 5948–5955 (2012).
24. Park, J. *et al.* Ultra-large-scale syntheses of monodisperse nanocrystals. *Nat. Mater.* **3,** 891–895 (2004).
25. Jarrett, B. R., Frendo, M., Vogan, J. & Louie, A. Y. Size-controlled synthesis of dextran sulfate coated iron oxide nanoparticles for magnetic resonance imaging. *Nanotechnology* **18,** 35603 (2007).
26. Gutiérrez, L. *et al.* Synthesis methods to prepare single- and multi-core iron oxide nanoparticles for biomedical applications. *Dalt. Trans.* 2943–2952 (2015). doi:10.1039/c4dt03013c
27. Lartigue, L. *et al.* Cooperative organization in iron oxide multi-core nanoparticles potentiates their efficiency as heating mediators and MRI contrast agents. *ACS Nano* **6,** 10935–49 (2012).
28. Dozier, D., Palchoudhury, S. & Bao, Y. Synthesis of iron oxide nanoparticles with biological coatings. *J. Sci. Heal. …* 16–18 (2010). at <http://scholar.google.com/scholar?hl=en&btnG=Search&q=intitle:Synthesis+of+Iron+Oxide+Nanoparticles+with+Biological+Coatings#0>
29. FDA. Approved Drug Products with Therapeutic Equivalence Evaluations. *Orange Book*

1 (2016). at <http://www.accessdata.fda.gov/scripts/cder/ob/docs/tempai.cfm>
30. Laurent, S. *et al.* Magnetic iron oxide nanoparticles: Synthesis, stabilization, vectorization, physicochemical characterizations and biological applications. *Chem. Rev.* **108,** 2064–2110 (2008).
31. Xie, J., Huang, J., Li, X., Sun, S. & Chen, X. Iron oxide nanoparticle platform for biomedical applications. *Curr. Med. Chem.* **16,** 1278–94 (2009).
32. Pradal, J. *et al.* Effect of particle size on the biodistribution of nano- and microparticles following intra-articular injection in mice. *Int. J. Pharm.* **498,** 119–129 (2016).
33. Absar Ahmad, *,†, Satyajyoti Senapati, ‡, M. Islam Khan, †, Rajiv Kumar, ‡ and & Murali Sastry*, §. Extracellular Biosynthesis of Monodisperse Gold Nanoparticles by a Novel Extremophilic Actinomycete, Thermomonospora sp. (2003).
34. Stöber, W., Fink, A. & Bohn, E. Controlled growth of monodisperse silica spheres in the micron size range. *J. Colloid Interface Sci.* **26,** 62–69 (1968).
35. Matsumura, Y. & Maeda, H. a New Concept for Macromolecular Therapeutics in Cancer-Chemotherapy - Mechanism of Tumoritropic Accumulation of Proteins and the Antitumor Agent Smancs. *Cancer Res.* **46,** 6387–6392 (1986).
36. Park, K. Facing the truth about nanotechnology in drug delivery. *ACS Nano* **7,** 7442–7447 (2013).
37. Owens, D. E. & Peppas, N. A. Opsonization, biodistribution, and pharmacokinetics of polymeric nanoparticles. *Int. J. Pharm.* **307,** 93–102 (2006).
38. Li, S. D. & Huang, L. Pharmacokinetics and biodistribution of nanoparticles. *Mol. Pharm.* **5,** 496–504 (2008).
39. Sonaje, K. *et al.* Biodistribution, pharmacodynamics and pharmacokinetics of insulin analogues in a rat model: Oral delivery using pH-Responsive nanoparticles vs. subcutaneous injection. *Biomaterials* **31,** 6849–6858 (2010).
40. Albanese, A., Tang, P. S. & Chan, W. C. W. The Effect of Nanoparticle Size, Shape, and Surface Chemistry on Biological Systems. *Annu. Rev. Biomed. Eng.* **14,** 1–16 (2012).
41. Zong, Y. *et al.* Effect of size and charge on pharmacokinetics and in vivo MRI contrast enhancement of biodegradable polydisulfide Gd(III) complexes. *J. Control. Release* **112,** 350–356 (2006).
42. Jinno, J. I. *et al.* Effect of particle size reduction on dissolution and oral absorption of a poorly water-soluble drug, cilostazol, in beagle dogs. *J. Control. Release* **111,** 56–64 (2006).
43. Yadav, K. S., Chuttani, K., Mishra, A. K. & Sawant, K. K. Effect of Size on the Biodistribution and Blood Clearance of Etoposide-Loaded PLGA Nanoparticles. *PDA J. Pharm. Sci. Technol.* **65,** 131–9 (2011).

44. Kulkarni, S. A. & Feng, S.-S. Effects of particle size and surface modification on cellular uptake and biodistribution of polymeric nanoparticles for drug delivery. *Pharm. Res.* **30,** 2512–22 (2013).
45. Duplessis, J., Ramachandran, C., Weiner, N. & Muller, D. The influence of particle size of liposomes on the deposition of drug into skin. *Int. J. Pharm.* **103,** 277–282 (1994).
46. Chono, S., Tanino, T., Seki, T. & Morimoto, K. Influence of particle size on drug delivery to rat alveolar macrophages following pulmonary administration of ciprofloxacin incorporated into liposomes. *J. Drug Target.* (2008). at <http://www.tandfonline.com/doi/abs/10.1080/10611860600834375?journalCode=idrt20>
47. Jung, C. W. & Jacobs, P. Physical and chemical properties of superparamagnetic iron oxide MR contrast agents: ferumoxides, ferumoxtran, ferumoxsil. *Magn. Reson. Imaging* **13,** 661–674 (1995).
48. Wang, Y.-X. J., Hussain, S. M. & Krestin, G. P. Superparamagnetic iron oxide contrast agents: physicochemical characteristics and applications in MR imaging. *Eur. Radiol.* **11,** 2319–2331 (2001).
49. Hunter Bradley Rogers. Size Optimization of Magnetic Nanoparticles for Biomedical Applications via a Novel Size-Selective Fractionation Process. *Auburn University* (2014).
50. Li, Y., Chen, T., Tan, W. & Talham, D. R. Size-dependent MRI relaxivity and dual imaging with Eu0.2Gd 0.8PO4H2O Nanoparticles. *Langmuir* **30,** 5873–5879 (2014).
51. Eric D. Smolensky, Hee-Yun E. Park, Yue Zhou, Gabriele A. Rolla, M. & Marjańska, Mauro Botta, and V. C. P. Scaling Laws at the Nano Size: The Effect of Particle Size and Shape on the Magnetism and Relaxivity of Iron Oxide Nanoparticle Contrast Agents. *J Mater Chem B Mater Biol Med* **1,** 2818–2828 (2013).
52. Shellock, F. G. & Kanal, E. Safety of magnetic resonance imaging contrast agents. *J. Magn. Reson. Imaging* **10,** 477–84 (1999).
53. Grobner, T. & Prischl, F. C. Gadolinium and nephrogenic systemic fibrosis. *Kidney Int.* **72,** 260–4 (2007).
54. Faucher, L., Tremblay, M., Lagueux, J., Gossuin, Y. & Fortin, M. A. Rapid synthesis of PEGylated ultrasmall gadolinium oxide nanoparticles for cell labeling and tracking with MRI. *ACS Appl. Mater. Interfaces* **4,** 4506–4515 (2012).
55. Jordan, A. *et al.* Inductive heating of ferrimagnetic particles and magnetic fluids: physical evaluation of their potential for hyperthermia. *Int. J. Hyperthermia* **9,** 51–68
56. Di Corato, R. *et al.* Magnetic hyperthermia efficiency in the cellular environment fordifferent nanoparticle designs. *Biomaterials* **35,** 6400–6411 (2014).
57. Stauffer, P. R., Cetas, T. C. & Jones, R. C. Magnetic Induction Heating of Ferromagnetic Implants for Inducing Localized Hyperthermia in Deep-Seated Tumors. *IEEE Trans.*

*Biomed. Eng.* **BME-31,** 235–251 (1984).

58. Gordon, R. T., Hines, J. R. & Gordon, D. Intracellular hyperthermia. A biophysical approach to cancer treatment via intracellular temperature and biophysical alterations. *Med. Hypotheses* **5,** 83–102 (1979).
59. Gaumet, M., Vargas, A., Gurny, R. & Delie, F. Nanoparticles for drug delivery: the need for precision in reporting particle size parameters. *Eur. J. Pharm. Biopharm.* **69,** 1–9 (2008).
60. Johannsen, M. *et al.* Thermotherapy of Prostate Cancer Using Magnetic Nanoparticles: Feasibility, Imaging, and Three-Dimensional Temperature Distribution. *Eur. Urol.* **52,** 1653–1662 (2007).
61. Maier-Hauff, K. *et al.* Efficacy and safety of intratumoral thermotherapy using magnetic iron-oxide nanoparticles combined with external beam radiotherapy on patients with recurrent glioblastoma multiforme. *J. Neurooncol.* **103,** 317–324 (2011).
62. Dudeck, O. *et al.* Local arterial infusion of superparamagnetic iron oxide particles in hepatocellular carcinoma: A feasibility and 3.0 T MRI study. *Invest Radiol* **41,** 527–535 (2006).
63. Kumar, C. S. S. R. & Mohammad, F. Magnetic nanomaterials for hyperthermia-based therapy and controlled drug delivery. *Adv. Drug Deliv. Rev.* **63,** 789–808 (2011).
64. Hilger, I. *et al.* Thermal ablation of tumors using magnetic nanoparticles: an in vivo feasibility study. *Invest. Radiol.* **37,** 580–6 (2002).
65. Tanaka, K. *et al.* Heat immunotherapy using magnetic nanoparticles and dendritic cells for T-lymphoma. *J. Biosci. Bioeng.* **100,** 112–5 (2005).
66. Thiesen, B. & Jordan, A. Clinical applications of magnetic nanoparticles for hyperthermia. *Int.J Hyperth.* **24,** 467–474 (2008).
67. Hergt, R., Dutz, S., Michael, R. & Röder, M. Effects of size distribution on hysteresis losses of magnetic nanoparticles for hyperthermia. *J. Phys. Condens. Matter* **20,** 385214 (2008).
68. Hergt, R., Dutz, S., Müller, R. & Zeisberger, M. Magnetic particle hyperthermia: nanoparticle magnetism and materials development for cancer therapy. *J. Phys. Condens. Matter* **18,** S2919–S2934 (2006).
69. Sheng, Peng; Shouheng, S. No TitleChemical Synthesis of Monodisperse Magnetic Nanoparticles. *Mater. Matters* **4,** 14 (2009).
70. Jordan, A. *et al.* Endocytosis of dextran and silan-coated magnetite nanoparticles and the effect of intracellular hyperthermia on human mammary carcinoma cells in vitro. *J. Magn. Magn. Mater.* **194,** 185–196 (1999).
71. Jordan, A., Scholz, R., Wust, P., Fähling, H. & Roland Felix. Magnetic fluid hyperthermia

(MFH): Cancer treatment with AC magnetic field induced excitation of biocompatible superparamagnetic nanoparticles. *J. Magn. Magn. Mater.* **201,** 413–419 (1999).

72. Soheilian, R. *et al.* Toward Accumulation of Magnetic Nanoparticles into Tissues of Small Porosity. *Langmuir* **31,** 8267–8274 (2015).
73. Min, K. A. *et al.* Pulsed magnetic field improves the transport of iron oxide nanoparticles through cell barriers. *ACS Nano* **7,** 2161–2171 (2013).
74. Wust, P. D. P. *et al.* Magnetic nanoparticles for interstitial thermotherapy – feasibility, tolerance and achieved temperatures. *Int J Hyperth.* (2009).
75. Hyeon, T. Chemical synthesis of magnetic nanoparticles. *Chem. Commun.* **8,** 927–934 (2003).
76. Liu, C. *et al.* Polyol Process Synthesis of Monodispersed FePt Nanoparticles. *J. Phys. Chem. B* **108,** 6121–3 (2004).
77. Xie, J. *et al.* One-pot synthesis of monodisperse iron oxide nanoparticles for potential biomedical applications. *Pure Appl. Chem.* **78,** 1003–1014 (2006).
78. Zhao, F., Yuan, M., Zhang, W. & Gao, S. Monodisperse lanthanide oxysulfide nanocrystals. *J. Am. Chem. Soc.* **128,** 11758–11759 (2006).
79. Constantinides, C. D. *et al.* Superparamagnetic iron oxide MION as a contrast agent for sodium MRI in myocardial infarction. *Magn. Reson. Med.* **46,** 1164–1168 (2001).
80. Allkemper, T., Bremer, C., Matuszewski, L., Ebert, W. & Reimer, P. Contrast-enhanced blood-pool MR angiography with optimized iron oxides: effect of size and dose on vascular contrast enhancement in rabbits. *Radiology* **223,** 432–438 (2002).
81. Chastellain, M., Petri, A. & Hofmann, H. Particle size investigations of a multistep synthesis of PVA coated superparamagnetic nanoparticles. *J. Colloid Interface Sci.* **278,** 353–360 (2004).
82. Chambon, C., Clement, O., Le Blanche, A., Schouman-Claeys, E. & Frija, G. Superparamagnetic iron oxides as positive MR contrast agents: in vitro and in vivo evidence. *Magn. Reson. Imaging* **11,** 509–519 (1992).
83. Yoshida, T., Othman, N. B. & Enpuku, K. Characterization of magnetically fractionated magnetic nanoparticles for magnetic particle imaging. *J. Appl. Phys.* **114,** 173908 (2013).
84. Glöckl, G. *et al.* Development of a liquid phase immunoassay by time-dependent measurements of the transient magneto-optical birefringence using functionalized magnetic nanoparticles. *J. Magn. Magn. Mater.* **289,** 480–483 (2005).
85. Shiozawa, M., Kobayashi, S., Sato, Y. & Maeshima, H. Magnetic resonance lymphography of sentinel lymph nodes in patients with breast cancer using superparamagnetic iron oxide : a feasibility study. 394–401 (2014). doi:10.1007/s12282-012-0401-y

86. Johnson, L., Pinder, S. E. & Douek, M. Deposition of superparamagnetic iron-oxide nanoparticles in axillary sentinel lymph nodes following subcutaneous injection. 481–486 (2013). doi:10.1111/his.12019
87. Chertok, B. *et al.* Iron Oxide Nanoparticles as a Drug Delivery Vehicle for MRI Monitored Magnetic Targeting of Brain Tumors. *Biomaterials* **29,** 487–496 (2009).
88. Anani, T., Panizzi, P. & David, A. E. Nanoparticle-based probes to enable noninvasive imaging of proteolytic activity for cancer diagnosis. *Nanomedicine* **11,** 2007–2022 (2016).
89. Moghimi, S. M., Hunter, A. C. & Murray, J. C. Long-circulating and target-specific nanoparticles: theory to practice. *Pharmacol. Rev.* **53,** 283–318 (2001).
90. Grzybowski, B. A., Bishop, K. J. M., Wilmer, C. E., Soh, S. & Grzybowski, B. A. Nanoscale Forces and Their Uses in Self-Assembly. 1600–1630 (2009). doi:10.1002/smll.200900358
91. Corot, C. & Warlin, D. Superparamagnetic iron oxide nanoparticles for MRI : contrast media pharmaceutical company R & D perspective. **5,** 411–422 (2013).
92. Li, L. *et al.* T h e r a n o s t i c s Superparamagnetic Iron Oxide Nanoparticles as MRI contrast agents for Non-invasive Stem Cell Labeling and Tracking. **3,** (2013).
93. Matsumura, Y. & Maeda, H. A New Concept for Macromolecular Therapeutics in Cancer Chemotherapy: Mechanism of Tumoritropic Accumulation of Proteins and the Antitumor Agent Smancs. *Cancer Res.* **46,** 6387–6392 (1986).
94. Blanco-Andujar, C., Ortega, D., Southern, P., Pankhurst, Q. a & Thanh, N. T. K. High performance multi-core iron oxide nanoparticles for magnetic hyperthermia: microwave synthesis, and the role of core-to-core interactions. *Nanoscale* **7,** 1768–75 (2015).
95. Ditsch, A., Lindenmann, S., Laibinis, P. E., Wang, D. I. C. & Hatton, T. A. High-gradient magnetic separation of magnetic nanoclusters. *Ind. Eng. Chem. Res.* **44,** 6824–6836 (2005).
96. Giddings, J., Yang, F. & Myers, M. Flow-field-flow fractionation: a versatile new separation method. *Science (80-. ).* **193,** (1976).
97. Latham, A. H. & Williams, M. E. Capillary magnetic field flow fractionation and analysis of magnetic nanoparticles. *Abstr. Pap. 230th ACS Natl. Meet. Washington, DC, United States, Aug. 28-Sept. 1, 2005* **77,** ANYL--207 (2005).
98. Rogers, H. B., Anani, T., Choi, Y. S., Beyers, R. J. & David, A. E. Exploiting Size-Dependent Drag and Magnetic Forces for Size-Specific Separation of Magnetic Nanoparticles. *Int. J. Mol. Sci.* **16,** 20001–19 (2015).
99. Löwa, N. *et al.* Journal of Magnetism and Magnetic Materials Hydrodynamic and magnetic fractionation of superparamagnetic nanoparticles for magnetic particle imaging. *J. Magn. Magn. Mater.* **380,** 266–270 (2015).

100. Cole, A. J. *et al.* NIH Public Access. **32,** 2183–2193 (2012).
101. Weissleder, R. *et al.* Ultrasmall superparamagnetic iron oxide: characterization of a new class of contrast agents for MR imaging. *Radiology* **175,** 489–493 (1990).
102. Gerber, R., Takayasu, M. & Friedlaender, F. Generalization of HGMS theory: The capture of ultra-fine particles. *Magn. IEEE Trans.* **19,** 2115–2117 (1983).
103. Adam J. Cole, Allan E. David, Jianxin Wang, Craig J. Galbán, and V. C. Y. Magnetic brain tumor targeting and biodistribution of long- circulating PEG-modified, cross-linked starch coated iron oxide nanoparticles. *Biomaterials* **32,** 6291–6301 (2012).
104. Cheng, J. *et al.* Magnetically Responsive Polymeric Microparticles for Oral Delivery of Protein Drugs. **23,** (2006).
105. Jaillard, D. & Hoebeke, J. Folate-Conjugated Iron Oxide Nanoparticles for Solid Tumor Targeting as Potential Specific Magnetic Hyperthermia Mediators ... Folate-Conjugated Iron Oxide Nanoparticles for Solid Tumor Targeting as Potential Specific Magnetic Hyperthermia Mediators : Synthesis , Physicochemical Characterization , and in Vitro. (2017). doi:10.1021/bc050050z
106. Icp-ms, M., Elias, A., Crayton, S. H., Warden-rothman, R. & Tsourkas, A. Quantitative Comparison of Tumor Delivery for Multiple Targeted Nanoparticles Simultaneously by. 1–9 (2014). doi:10.1038/srep05840
107. Kirpotin, D. B. *et al.* Antibody Targeting of Long-Circulating Lipidic Nanoparticles Does Not Increase Tumor Localization but Does Increase Internalization in Animal Models. 6732–6741 (2006). doi:10.1158/0008-5472.CAN-05-4199
108. Rad, A. M., Arbab, A. S., Jiang, Q. & Soltanian-zadeh, H. Quantification of Superparamagnetic Iron Oxide (SPIO)-labeled Cells Using MRI. *J Magn Reson Imaging* **26,** 366–374 (2015).
109. Soheilian, R. *et al.* Toward Accumulation of Magnetic Nanoparticles into Tissues of Small Porosity. (2015). doi:10.1021/acs.langmuir.5b01458
110. Nanoparticles, O. & Under, H. Transcellular Transport of Heparin-coated Magnetic Iron Oxide Nanoparticles (Hep-MION) Under the Influence of an Applied Magnetic Field. 119–135 (2010). doi:10.3390/pharmaceutics2020119